

18 NSWC/WOL TR 77-137

12
50

AD A 052689

6
EXPERIMENTAL INVESTIGATION OF THE
KINETICS OF THE SHOCK-INDUCED
ALPHA TO EPSILON PHASE TRANS-
FORMATION IN ARMCO IRON,

10
Jerry W. FORBES

RESEARCH AND TECHNOLOGY DEPARTMENT

AD NO.
DDC FILE COPY

11
15 DEC 1977

16
ZR 011 01

17
ZR 011 01 01

12
149 p.

Approved for public release, distribution unlimited.

15
F44620-67-C-0087,
✓ AFOR-66-1088

DDC
RECEIVED
APR 14 1978
B 16



NAVAL SURFACE WEAPONS CENTER

Dahlgren, Virginia 22448 • Silver Spring, Maryland 20910

269 850 - [handwritten notes]

UNCLASSIFIED

SECURITY CLASSIFICATION OF THIS PAGE (When Data Entered)

20. (continued)

tion, f , transformed, and the difference in the Gibbs energies, $G_2 - G_1$:

$$1 - f = \exp \left[\theta(G_2 - G_1 - A) \right]$$

where θ is constant, and A is the value of $G_2 - G_1$ at the onset of transformation. This relation shows that an increase in $G_2 - G_1$ results in more transformation. To provide a basis for understanding this behavior, a relation between the number of "frozen-in" nucleation sites and driving force, $G_2 - G_1$, is established. The "frozen-in" nuclei occur because equilibrium embryos of the second phase, which result from statistical fluctuations, may be forced into the stability field of the second phase by sudden application of sufficient pressure. The relation so established has at best a remote numerical similarity to the experimental relation, but it shows promise of further development.

UNCLASSIFIED

SECURITY CLASSIFICATION OF THIS PAGE (When Data Entered)

SUMMARY

This work contributes new understanding of the dominant processes for phase transformations which may occur under conditions of shock wave loading of materials. It should be of interest to material scientists and design engineers who deal with shockwaves or impulsive loads. The work was supported principally by the Naval Surface Weapons Center Independent Research Program, Task 177, with additional support from the Air Force Office of Scientific Research under Grant No. AF-AFSOR-1088-66 and (ARPA) Contract F-44620-67-C-0087.

Julius W. Enig
JULIUS W. ENIG
By direction

ACCESSION for	
NTIS	White Section <input checked="" type="checkbox"/>
DDC	Buff Section <input type="checkbox"/>
UNANNOUNCED	<input type="checkbox"/>
JUSTIFICATION	
BY	
DISTRIBUTION/AVAILABILITY CODES	
Dist.	AVAIL. and/or SPECIAL
A	

PREFACE

The number of friends and colleagues giving me moral support and advice are too numerous to mention, but first I thank my thesis committee: Dr. George E. Duvall, Chairman; Dr. Richard M. Fowles; and Dr. M. Howard Miles, of Washington State University, for their help. Professor Duvall increased my understanding of a number of technical points, edited the final draft of this dissertation, and provided guidance in a supportive manner.

Second, Mr. John O. Erkman, Mr. Nathaniel L. Coleburn, and Dr. D. J. Pastine of the Naval Surface Weapons Center played major roles in supporting my efforts. John and Nat offered technical advice and edited some preliminary drafts of some sections of the dissertation. Nat also helped secure funds for the research. I credit their influence for my continuing this work when it sometimes appeared an impossible task. Dr. Pastine was my local adviser. To all the people mentioned above, and to many others whom I have thanked privately, I am grateful.

TABLE OF CONTENTS

	Page
SUMMARY	i
PREFACE	ii
LIST OF TABLES	vi
LIST OF ILLUSTRATIONS	vii
Chapter	
1. INTRODUCTION	1
1.1. General Background of Polymorphism	1
1.2. Alpha to Epsilon Transformation in Iron.	3
1.2.1. Background	4
1.2.2. Shock Profile Data Related to Transformation Kinetics	4
1.2.3. Evidence for Non-equilibrium Behavior of Mixed Phases	7
1.3. Outline of This Work	9
1.4. Summary	10
2. EXPERIMENTAL CONCEPTS	12
2.1. Basic Relations	12
2.2. Wave Propagation	14
2.3. Free Surface Velocity Measurements	17
3. EXPERIMENTAL PROCEDURES	23
3.1. General Facilities	23
3.2. Armco Iron Properties	24
3.2.1. Metallurgical Properties	24
3.2.2. Sample Preparations	25

TABLE OF CONTENTS (Cont.)

	Page
3.3. Types of Experiments	26
3.4. Elastic Precursor Experiments	26
3.5. Plate Slap Experiments	28
3.5.1. Flier Plate System for Plate Slap Experiments	28
3.5.2. Target Preparation for Plate Slap Experiments	31
3.5.3. Laboratory Methods	34
3.6. Explosively Driven Experiments	37
4. EXPERIMENTAL RESULTS	39
4.1. Elastic Precursor Data	39
4.2. Transmission Data for a 25.4-mm Thick Sample	42
4.3. Transmission Data for Thin Samples	42
4.3.1. Plastic I Data	42
4.3.2. Plastic II Data	48
4.3.3. Stress-Volume State Behind the Plastic II Shock	53
4.4. Summary	55
5. THEORY OF THE ALPHA TO EPSILON TRANSFORMATION	56
5.1. Review of Experimental Information	56
5.1.1. Shock Experiments	56
5.1.2. Static Experiments	59
5.1.3. Discussion	61
5.2. Characteristics of Martensitic Transformation	61
5.2.1. Crystallography	63
5.2.2. Uniaxial Strain	68
5.2.3. Fraction Transformed	69
5.2.4. Fraction Transformed in Athermal Transformation	71
5.3. Nucleation of a New Phase	72
5.3.1. Nucleation Sites	73
5.3.2. Nucleation Due to Rapid Application of Stress	74

TABLE OF CONTENTS (Cont.)

	Page
5.4. The Quasistatic Hugoniot	83
6. KINETICS OF TRANSFORMATION	91
6.1. Relaxation Times	94
6.1.1. Decay of Stress Associated with the Plastic I Shock	94
6.1.2. Rise Time of Plastic II Shocks	96
6.1.3. Metallurgical Data	97
6.2. Slow Decay of the Stress Behind the Plastic I Shock	101
6.3. Discussion	103
7. SUMMARY AND CONCLUSIONS	104
REFERENCES	108
APPENDIX	
A. THERMODYNAMICALLY CONSISTENT EQUATION OF STATE . .	112
A.1. Equilibrium Surfaces	113
A.2. Approximations of Potential Functions . .	118
B. STREAK CAMERA CALIBRATION	121
B.1. Writing Speed	121
B.2. Dynamic Spatial Resolution	124
C. ERROR ANALYSIS	125
C.1. General Treatment of Errors	125
C.2. Error in Free Surface Velocity Measurements	127
C.2.1. Sources of Various Errors	128
C.2.2. Errors in Determining the Trace Angle and the Wave Tilt Angle	130
D. PERMANENT REGIME WAVE SOLUTION	134
D.1. General Solution	134
D.2. Rate Equation	136

LIST OF TABLES

Table	Page
3.1. Types of experiments	27
4.1. Elastic precursor amplitudes in Armco iron	40
4.2. Plastic I data	43
4.3. Plastic II data	49
5.1. Iron transformation stress	57
5.2. Values of dN^*/dG_{21}	84
A.1. Initial values	117
B.1. Calibration experimental results	123
C.1. Various contributions to the error in u_{fs}	129

LIST OF ILLUSTRATIONS

Figure	Page
1.1. Two shock wave stress-distance profiles in iron for times t_2 and t_3 where $t_2 < t_3$	5
2.1. Lagrangian distance-time diagram of shock wave propagation in iron	15
2.2. Reflected light plate slap experiment (a) and corresponding streak camera record (b)	18
2.3. Streak camera record	20
3.1. Flier plate system for plate slap experiments	29
3.2. Diagram showing relation of experimental target, light source, and camera for transmission experiments	35
4.1. Elastic precursor stress as a function of sample thickness	41
4.2. Free surface velocity of iron after plastic I shock arrival	44
4.3. Stress behind the plastic I shock in iron as a function of sample thickness	45
4.4. Stress jump across the plastic I shock as a function of sample thickness	46
4.5. Shock wave arrival times at free surfaces	50
4.6. Corrected Lagrangian h-t diagram for beginning of the plastic II front	52
4.7. Iron Hugoniot states	54
5.1. Transformation stress for iron under compression at various temperatures	60
5.2. Body centered lattice	65

LIST OF ILLUSTRATIONS (Cont.)

Figure	Page
5.3. Shear mechanism for body-centered-cubic to hexagonal-close-packed transformation	67
5.4. Subdivision of a single grain by martensitic plates. A and B are first and second generation plates, respectively	70
5.5. Shear mechanism in body-centered-cubic iron to obtain hexagonal symmetry along a twin plane . .	75
5.6. Spherical embryos in stable phase 1. Curve A is for the stable phase 1 field with $G_2 - G_1 = G_{21} > 0$. Curve B is for low pressure sufficient to make the phase 2 field stable with $G_{21}(n_1^*) < 0$. Curve C is for higher pressure, P_2 , for which $G_{21}(n_2^*) < G_{21}(n_1^*) < 0$	76
5.7. Amount of epsilon phase as a function of stress in excess of 130 kbar	86
6.1. Isotherm used to define $f^{eq} = (V_A - V_1^T) / (V_1^T - V_2^T)$ for state A where $0 \leq f^{eq} \leq 1$ and $f^{eq} = 1$ for state B where $V_B \leq V_2^T$	93
6.2. Temperature-independent steady plastic II shock fronts using Eq. (6.4.) and $U_2 - u_1 = 3.36$ mm/ μ sec.	98
6.3. Reflected plastic I wave reduces the stress in and behind the plastic II shock front to a value below the transformation stress. This process leaves a zone, $h_5 - h_3$, in iron of varying hardness	100
6.4. Stress-particle velocity states at the impact boundary when an iron sample is impacted by an aluminum plate	102

LIST OF ILLUSTRATIONS (Cont.)

Figure		Page
A.1.	Difference between Gibbs energies of alpha and epsilon iron along the mixed phase Hugoniot . .	119
B.1.	Schematic of calibration technique for the streak camera	122
C.1.	Envelope of parallel lines between A and B make up the streak camera trace	132

CHAPTER 1
INTRODUCTION

Under the influence of shock waves certain materials undergo polymorphic transformations. The time available in a shock experiment for such a transformation to occur does not exceed a few microseconds, yet the same transformation may require minutes or hours for completion in a static experiment. This large transformation rate is an important distinctive feature of transformations in shock waves. Little is known about atomic mechanisms which cause these ultrafast transformations. This void in knowledge is partly due to lack of experimental data. The need for data and understanding of the transformation process is the reason for this work.

1.1. General Background
of Polymorphism

The ability of a compound to crystallize in different structures is well-established. Bridgman¹ showed that many materials undergo a transformation to a new structure under the influence of pressure. In more recent times it has been shown that many transformations observed statically are also observed dynamically; i.e., under shock compression. Examples of this are found in materials such as iron,^{2,3} carbon,^{4,5} bismuth,^{6,7} silicon,^{8,9} boron nitride,^{10,11} and many others.

To understand the varied aspects of polymorphism it is necessary to relate static results to dynamic measurements. Caution must be exercised in making this relation because of the distinct differences in compression methods. A plane shock wave results in uniaxial compression at very large strain rates accompanied with large shear forces. These properties can result in defect formation, plastic flow, and other irreversible effects.

Some progress in relating static and dynamic results has been made by identifying shear deformation as a likely mechanism that accelerates transformations. The addition of shear to a sample under static compression has been shown to accelerate the transformation process.¹² The accelerating effect of adding shear to static experiments has led Leiserowitz, *et al.*,¹³ to draw a controversial analogy between experiments on shock wave compression and experiments of hydrostatic pressure with shear stresses added. The role shear deformation plays in accelerating transformation rates in dynamic experiments is difficult to ascertain since an elevation of hydrostatic pressure above that normally required to produce the transformation can greatly increase the transformation rate.¹⁴ To date no explanation for differences between static and dynamic rates is satisfactory.

In dynamic experiments the transformation rate affects the shape and amplitude of shock waves which evolve towards the steady state. Studying evolution of a wave in time provides some understanding of dynamic polymorphism. Experimental shock studies of the kinetics of solid-solid phase transformations have been limited primarily to four materials: iron,^{2,15}

potassium chloride,^{16,17} antimony,¹⁸ and Arkansas novaculite.¹⁹

A framework for interpreting experiments in dynamic polymorphism was provided by Horie and Duvall,²⁰ who combined continuum mechanics and thermodynamics to treat the evolution of shock waves in materials with time-dependent phase transformations.

1.2. Alpha to Epsilon Transformation in Iron

Discovery of and serious attempts to understand the iron transformation appear to have followed the publication by Walsh²¹ of high pressure iron Hugoniot data which disagreed markedly with existing work on its compressibility at lower pressures. In particular, the results implied compression of iron significantly greater than would be expected from extrapolation of static compressibility data of Bridgman.¹ This stimulated studies using shock waves at lower stresses. The discrepancy in compressibility was resolved by the discovery by Minshall and his co-workers^{2,22} of multiple shock stress waves from which they inferred the existence of a polymorphic transformation near 130 kbar.

Many questions still remain unresolved about the pressure-induced iron phase transformation. The mechanism of transformation and effects of shear, temperature, pressure gradients, and strain rate on the transformation process are not fully understood. In addition, Hugoniot data and equilibrium thermodynamic predictions differ for the mixed-phase region. The work in this dissertation is directed toward understanding the non-equilibrium behavior of the mixed-phase region for the iron transformation.

1.2.1. Background

Iron is an elastic-plastic material which undergoes a phase transformation when stressed above 130 kbar. These properties will result in three forward-facing shocks (elastic, plastic I, and plastic II, respectively) traveling away from the impact surface. Under equilibrium conditions the stress behind the plastic I shock is a measure of transformation pressure for the polymorphic transformation. Time-dependence of the transformation requires that stress in the plastic I shock and the plastic II shock overshoot their equilibrium values for short times after impact. The evolution of the shocks is illustrated in Fig. 1.1 where shock wave pressure-distance profiles are drawn for two different times following impact on the left. Measurement of shock amplitudes as a function of thickness can be used in conjunction with appropriate models to obtain information about kinetics of the transformation process.

1.2.2. Shock Profile Data Related to Transformation Kinetics

Transformation rate affects the shapes and amplitudes of shocks in iron. There are four types of existing experimental data on shock profiles in iron which relate to transition kinetics. The four types of data are: (1) amplitude of stress behind the plastic I shock as a function of sample thickness, (2) amplitude of stress behind the plastic I shock as a function of final driving stress for constant sample thickness, (3) rise time in the plastic II shock front, and (4) thickness of the plastic II shock front inferred from residual metallurgical effects.

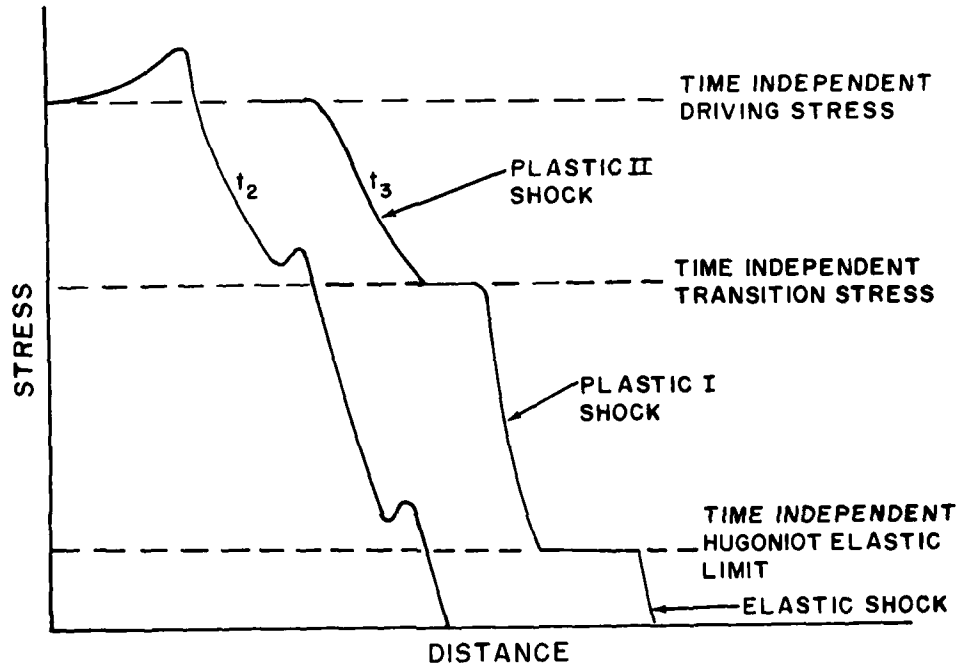


FIGURE 1.1 TWO SHOCK WAVE STRESS-DISTANCE PROFILES IN IRON FOR TIMES t_2 AND t_3 WHERE $t_2 < t_3$.

The plastic I wave stress exceeds its eventual time-independent value near the impact boundary, and time required for the stress to decay to its time-independent value is related to kinetics of the transformation. Minshall and his co-workers,^{2,22} measured a slow decay in the plastic I wave stress as a function of thickness for a decaying driving stress. The plastic I stress was about 140 kbar in a sample 6-mm thick; it decayed to 130 kbar in a sample 40-mm thick. In the present experimental work I measured a similar slow decay in plastic I stress as a function of thickness for constant final driving stress. The plastic I stress was about 139 kbar for a 1-mm-thick sample and decayed to 131 kbar in a 25-mm-thick sample. Final driving stress was near 200 kbar. Barker and Hollenbach¹⁵ measured a small increase in the plastic I stress with increase of final driving stress for constant sample thickness; amplitude of stress behind the plastic I shock increased by 6 kbar when final driving stress changed from 130 kbar to 300 kbar for 6.35-mm-thick samples.¹⁵

The transformation process occurs principally in the plastic II shock front; therefore, the rate of transformation may contribute significantly to rise time of this wave. I and a number of experimenters^{15,23} have measured rise times of 0.2 to 0.3 μ sec for the plastic II shock front in iron by monitoring surface motion of shocked samples. A less accurate method of obtaining rise time information is from residual metallurgical effects,^{24,25} which imply shock front thickness; for an approximately steady wave, rise time is obtained by dividing shock front

thickness by wave velocity. Smith²⁴ has suggested that the plastic II shock front width in iron is less than 0.02 mm, based on metallurgical data. This shock width implies a rise time of about 0.005 μ sec.

To interpret some of the above experimental results, Horie and Duvall²⁰ developed a model of mixed phases which contained a constant relaxation time parameter. This relaxation time has to be evaluated from experimental data. In considering available data, they found a relaxation time of 1/3 μ sec based on rise time measurements of Novikov, et al,²³ for the plastic II shock front of 0.01 μ sec based on the plastic II shock front width of less than 0.02 mm reported by Smith²⁴, and of 20 μ sec based on the slow decay of the plastic I stress observed by Minshall.²² A relaxation time less than 0.05 μ sec is required to explain my data on decay of the plastic I stress, while Barker and Hollenbach¹⁵ found that a relaxation time of 0.16 to 0.18 μ sec was required to explain their data on plastic I stress decay. The disagreement among values of relaxation time impugns the validity of the Horie and Duvall²⁰ assumption of constant relaxation time.

1.2.3. Evidence for Non-equilibrium Behavior of Mixed Phases

Experimental and theoretical evidence exists which suggests that in the pressure range of 130 to 300 kbar iron is not in equilibrium and/or the transformation does not go to completion. The more pertinent results are summarized in this section.

At least two theoretical attempts have been made to understand the iron Hugoniot data between 130 and 300 kbar. Duvall and Horie²⁶ demonstrated that the calculated slopes of the equilibrium phase line in pressure-temperature space differs significantly from the measured slope. More recently, Andrews^{27,28,29} calculated the equilibrium Hugoniot for iron and found it to differ from Hugoniot data between 130 and 300 kbar. The conclusion from both treatments is that dynamic transformation data do not agree with equilibrium thermodynamics.

Single crystals of silicon iron have been subjected to x-ray diffraction and metallographic analysis after exposure to shock waves and relief waves which caused the formation and disintegration of the epsilon phase.³⁰ As a result of this cycle of transformation, one would expect single crystals to be transformed into polycrystalline aggregates. The diffraction analysis shows that the material had retained in large measure its original orientation, though it was polycrystalline. There are two possible explanations for this. The first is that the alpha to epsilon transformation and its reversal are crystallographically reversible to some extent.³¹ The second, suggested by German, et al.,³⁰ is that the transformation does not go to completion. This suggestion appears to be in better agreement with various experimental results.

Much of the experimental evidence implying non-equilibrium behavior comes from the results of static isothermal compression experiments. Such experiments show that the iron transformation

begins near 130 kbar and goes to completion for stresses greater than 150 kbar.^{32,33,34,35} This behavior disagrees with equilibrium thermodynamics, which requires complete transformation to occur at constant stress when temperature is held constant. This requirement appears never to be realized experimentally. A very thorough investigation of the Bismuth I-Bismuth II transformation by Zeto and Vanfleet⁶ shows that the onset of transformation in their apparatus always occurs at greater pressure than does the reverse transformation. They and others take equilibrium pressure of the transformation equal to the mean of direct and reverse transformation pressures.

An anomaly exists in static isothermal compression data which has not been carefully discussed in the literature: In some experiments iron appears to transform completely at the transformation pressure, while in other experiments with the same equipment the lower phase persists to higher pressures. No attempt is made to explain this anomaly because it involves analysis of static compression equipment and techniques which is beyond the ability of the author and the intended scope of this dissertation.

1.3. Outline of This Work

The basic problem studied in this work is the body-centered-cubic (alpha) to hexagonal-close - packed (epsilon) transformation in iron under shock compression. Iron samples were all initially at room temperature prior to shock loading.

Measurements were made of the evolution of shock waves with different sample thicknesses for approximately constant final driving stress. Experimental data were interpreted with the aid of a mixed phase continuum model with constant relaxation time to obtain some information about kinetics of the process. Hugoniot measurements in the mixed phase region are shown to correlate well with a simple relation between difference of Gibbs energies and fraction of material transformed. Some factors relating to deviations from equilibrium in the mixed phase region are explored.

1.4. Summary

The reasons for choosing to study iron were: (1) there exists a wealth of thermodynamic data on iron, (2) effects of the time-dependent phase transformation on shock profiles have been theoretically calculated by Horie and Duvall²⁰ and later by Andrews,^{27,29} and (3) the elastic precursor stress amplitude does not depend on final driving stress for sample thicknesses of 3 mm or greater.³⁶

The experimental intent of this study was to measure the evolution of the plastic I shock in polycrystalline Armco iron when final driving stress was 201 kbar. Basic findings were: (1) stress behind the plastic I shock increases from 131 to 140 kbar when sample thickness decreases from 25 to 1 mm, (2) transformation stress measured in a 25.4-mm-thick sample is 131.4 ± 3.3 kbar, (3) little or no variation of plastic I wave amplitude for propagation distances between 0.9 and

6.35 mm, (4) relative volume behind the plastic II wave is $V_3/V_0 = 0.871 \pm 0.008$ for a stress of 201 ± 8.4 kbar, (5) rise time for the plastic II shock is 0.18 ± 0.02 μ sec.

In terms of the Horie-Duvall model, decay of the plastic I wave implies an initial transformation rate greater than 2×10^7 /sec for final driving stress of 201 kbar.

CHAPTER 2
EXPERIMENTAL CONCEPTS

In this chapter a number of relations are given for converting experimental data into more useful forms. Sections deal with basic relations, wave propagation, and free surface velocity measurements.

2.1. Basic Relations

The equations for plane one-dimensional flow, independent of material properties, are:

$$\frac{\partial \rho}{\partial t} + \frac{\partial \rho u}{\partial x} = 0 , \quad (2.1)$$

$$\rho \frac{du}{dt} \equiv \rho \frac{\partial u}{\partial t} + \rho u \frac{\partial u}{\partial x} = - \frac{\partial P}{\partial x} , \quad (2.2)$$

$$\frac{dE}{dt} = -P \frac{dV}{dt} \quad \text{and} \quad V = \frac{1}{\rho} , \quad (2.3)$$

where t is time, x is Eulerian space coordinate, V is specific volume, u is mass velocity, E is specific internal energy, and P is stress in the x direction, positive in compression. Thermal conductivity is assumed to be negligible.

For steady waves the flow equations lead to the following jump conditions for a shock discontinuity:

$$\rho_2(U_2 - u_2) = \rho_1(U_2 - u_1) , \quad (2.4)$$

$$P_2 - P_1 = \rho_1(U_2 - u_1)(u_2 - u_1) , \quad (2.5)$$

$$E_2 - E_1 = \frac{1}{2} (P_2 + P_1)(V_1 - V_2) , \quad (2.6)$$

where U_2 is shock velocity. Subscript 2 is for the state behind the shock front while subscript 1 is for the state ahead of the shock. Density at room temperature and atmospheric pressure is given by ρ_0 . The measurement of any two parameters of the set (P, V, E, U_2, u) for known conditions ahead of the shock is sufficient to determine the other three. The two measured parameters for this work are shock velocity and change in free surface velocity, which is assumed to be twice the change in particle velocity; i.e.,

$$\Delta u_{fs} = 2\Delta u . \quad (2.7)$$

Walsh, et al.³⁷ have shown that particle velocity obtained from Eq. (2.7) is accurate to 1 percent for a single shock in iron with final stress of 400 kbar.

Free surface velocity produced by reflection of a shock from an unconfined surface is the sum of particle velocities produced by the shock, u , and by the reflected rarefaction, u_r , respectively; i.e.,

$$u_{fs} = u + u_r . \quad (2.8)$$

An elastic-plastic material which is also polymorphic, such as iron, has a complicated release path in the pressure-particle plane. Rigidity of the material and kinetics of the reverse transformation help determine the value of u_r . Treatment of the release of stress for shocked elastic-plastic solids has been fairly successful. Measurements of the reverse transformation reported by Barker and Hollenbach¹⁵ show that even in this case Eq. (2.7) is a good approximation. Equation (2.7) has been used throughout the present work to convert free surface velocities to particle velocities.

2.2. Wave Propagation

Plane shock waves are generated in the iron sample by impact of a flier plate or a plane detonation wave. After traveling a short distance, the initial shock develops into elastic, plastic I, and plastic II waves described in the introduction. These proceed through the sample and each interacts in turn with its plane free surface. A map of the process in space time is shown in Fig. 2.1. The space coordinate is Lagrangian, being the undisturbed x coordinate denoted h . The Lagrangian wave propagation velocity is denoted by a prime: U_1' for elastic wave, U_2' for plastic I, and U_3' for plastic II. Final stress behind the plastic II shock front is greater than transformation stress. Initial time-dependent effects involved in the formation of the three waves are not shown in the diagram. Reflected wave velocities are denoted R' and wave paths in Fig. 2.1 are labeled according to their slopes; e.g., $dt/dh = 1/U_1'$ for the

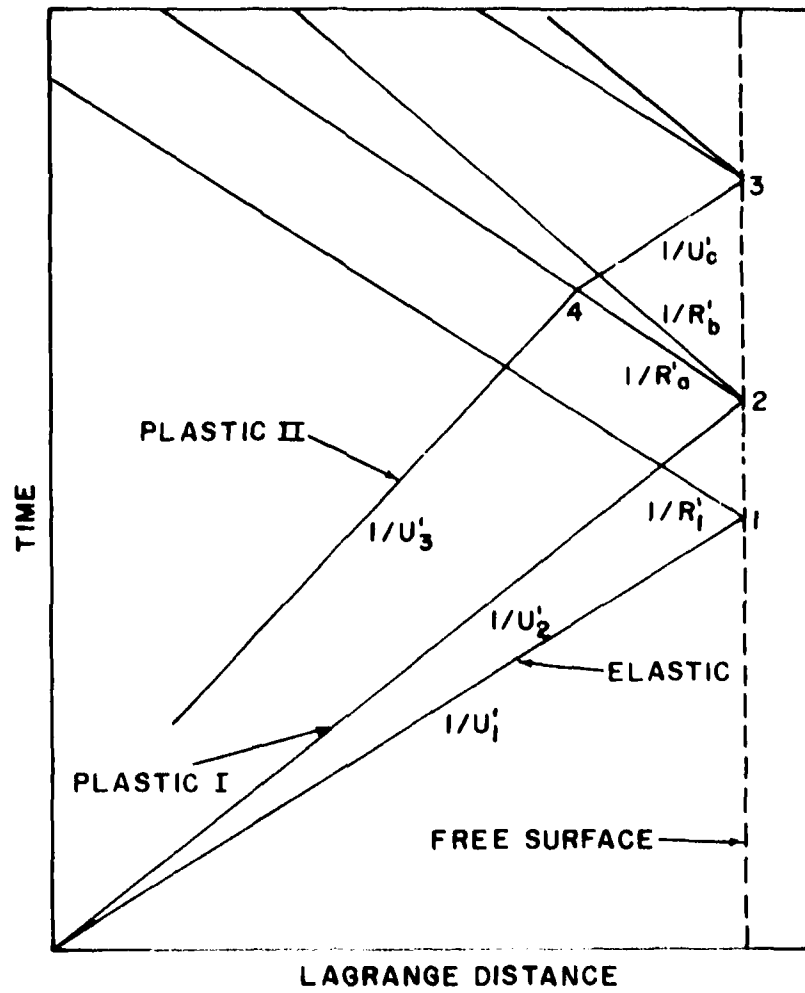


FIGURE 2.1 LAGRANGIAN DISTANCE-TIME DIAGRAM OF SHOCK WAVE PROPAGATION IN IRON.

elastic shock. Elastic reverberations between forward-facing shock fronts and free surface are ignored. Times labeled 1, 2, and 3 correspond to arrivals at the free surface of elastic, plastic I, and plastic II shocks, respectively.

Point 4 is the intersection of the forward-facing plastic II shock with the backward-facing relief wave originating at point 2. Point 4 lies on the locus of h-t points which nearly represents the path the original forward-facing plastic II shock would have taken without interference from the elastic relief wave. Coordinates of point 4 can be calculated from the results of a series of experiments with the same impact stress but different sample thicknesses, h_0 . The coordinates of point 4 are given by

$$t_4 = t_2 + \frac{(t_3 - t_2) \cdot U_c'}{U_c' + R_a'} \quad (2.9)$$

$$h_4 = h_0 - \frac{(t_3 - t_2) \cdot U_c' \cdot R_a'}{U_c' + R_a'} \quad (2.10)$$

where h_0 is the coordinate of the free surface. Arrival times t_2 and t_3 are measured; U_c' is assumed equal to elastic wave speed U_1 .

Eulerian velocities for plastic I and plastic II waves are obtained from Lagrangian velocities through use of the relations³⁸

$$U_2' = \frac{\rho_1}{\rho_0} (U_2 - u_1) \quad (2.11)$$

$$U_3' = \frac{\rho_2}{\rho_0} (U_3 - u_2) , \quad (2.12)$$

where ρ and u are density and particle velocity, respectively, behind the wave defined by the subscript.

Elastic wave velocity, $U_1 \equiv U_1'$, was taken to be 6.18 mm/ μ sec.³⁶ Plastic I velocity (Eulerian) for individual experiments was calculated by assuming the wave to be centered at $h=0$, $t=0$, which gives

$$U_2 = \frac{h_0 + u_1(t_2 - t_1)}{t_2} . \quad (2.13)$$

Experimental data on arrival times at the free surface for different h_0 support the assumption that the plastic I wave is centered at $h=0$, $t=0$.

2.3. Free Surface Velocity Measurements

Free surface and shock velocities were measured using the arrangement shown in Fig. 2.2. The mirrors shown were silvered on their lower surfaces and collimated light was allowed to fall on the assembly at near-normal incidence. Reflections were recorded on film in a rotating mirror camera. Part (b) of the figure represents the film record. Portions below the broken and near-horizontal lines are exposed; upper portions are unexposed.

Shock impact against a mirror surface causes the amount of light being reflected to decrease. The change in reflected light is recorded by the camera as a function of time. Time events labeled on the record are for flier arrival at the impact

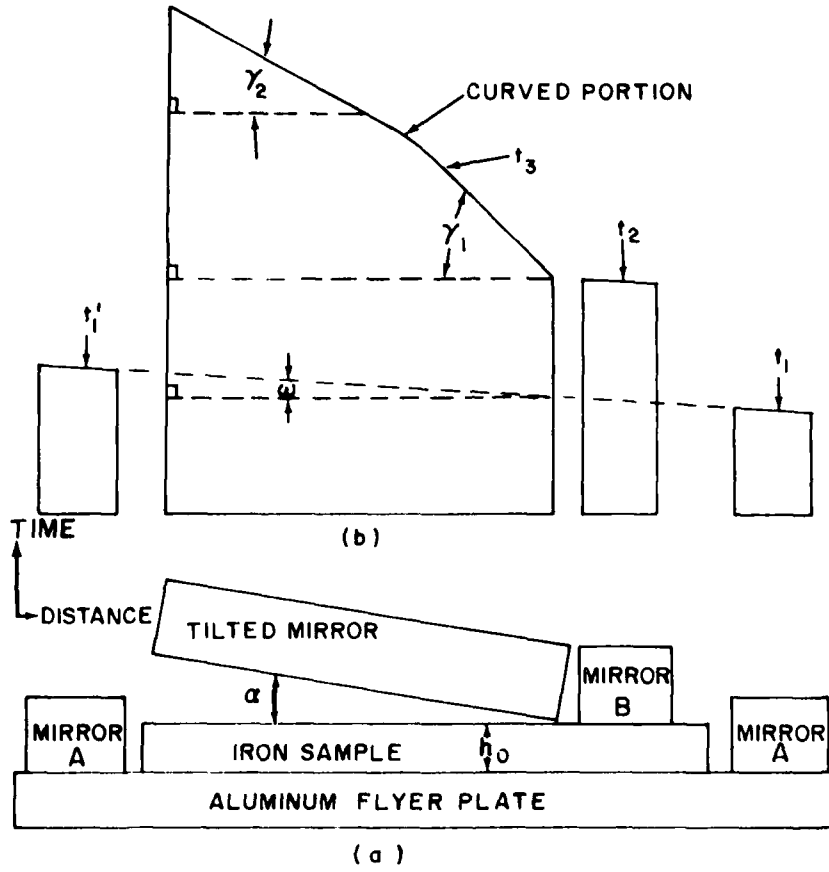


FIGURE 2.2 REFLECTED LIGHT PLATE SLAP EXPERIMENT (a) AND CORRESPONDING STREAK CAMERA RECORD (b).

surface, t_1 ; plastic I arrival at the free surface of the iron sample, t_2 ; and plastic II shock arrival at the free surface, t_3 . Elastic shock arrivals at the free surface were not recorded because of their small amplitudes. The continuous trace due to the free surface impacting the tilted mirror has two linear parts connected by a curved part. The first linear part represents free surface motion produced by the plastic I shock and makes an angle γ_1 with the distance axis on the film. The curved part is due to the finite rise time of the plastic II shock front. The second linear part represents free surface motion produced by the plastic II shock. It makes an angle γ_2 with the distance axis on the film. Tilt of the flier plate is indicated by non-simultaneous arrivals at the outside mirrors, A, labeled t_1 and t_1' on the record, and by non-simultaneous arrival over mirror B on the sample. Times t_1 and t_1' define a line which makes an angle ω with the distance axis.

Average shock wave velocities and free surface velocities are determined from measured distances and slopes, respectively, on the film record and from the known writing speed of the camera. A record is shown in Fig. 2.3 with the same labels as in Fig. 2.2.

Film records of the free surface motion were read with a Vanguard analyzer or a traveling microscope. Distances on the film as small as 0.006 and 0.001 mm can be resolved with the Vanguard analyzer and microscope, respectively. To accurately determine slopes of linear parts of the trace, many points were read and fitted by least squares to a straight line. Each trace was read at least three times and the resulting slopes were

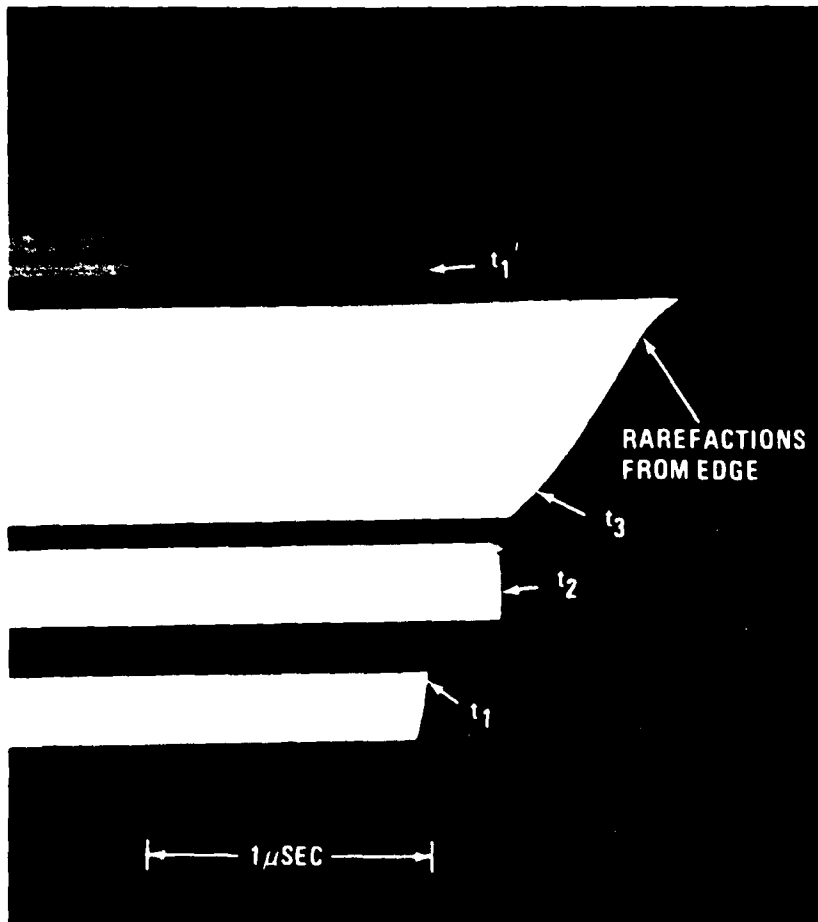


FIGURE 2.3 STREAK CAMERA RECORD.

averaged. In order to preclude points of the curved portion from the linear fits, the entire trace was graphed and limits of the linear portion were determined by inspection. This judgment was reviewed and proper adjustments were made after least-squares fitting of the straight line sections was completed. The time span of the curved portion was determined from the record and interpreted as a measure of rise time in the plastic II shock front. The equation relating free surface velocity, u_{f2} , produced by the plastic I shock, to measured parameters is³⁹

$$u_{f2} = \frac{u_c \tan \alpha}{M_f (\tan \gamma_1 - \tan \omega)} \quad (2.14)$$

where u_c is camera writing speed, M_f is camera magnification (image/object), α is angle between tilted mirror and the sample surface, γ_1 is the angle made by the first linear trace on the film, and ω is tilt of the shock wave measured on the film. These are indicated in Fig. 2.2. The small correction due to slight rotation of the surface by the elastic shock has been ignored in Eq. (2.14).

The equation relating free surface velocity, u_{f3} , produced by the plastic II shock to measured parameters is³⁹

$$u_{f3} = \frac{u_c \tan \alpha_1}{M_f \tan \gamma_2} \left[\frac{1 - \frac{\tan \omega}{\tan \gamma_1} \left(\frac{U_2 - u_{f2}}{U_3 - u_{f3}} \right)}{1 - \frac{\tan \omega}{\tan \gamma_2} \left(\frac{U_2 - u_{f2}}{U_3 - u_{f2}} \right)} \right] \quad (2.15)$$

where

$$\tan \alpha_1 = \frac{\tan \alpha + \tan \gamma_1}{\tan \gamma_1 - \tan \omega} \quad (2.16)$$

and where γ_2 is defined in Fig. 2.2.

CHAPTER 3
EXPERIMENTAL PROCEDURES

3.1. General Facilities

Most experiments were done at the Naval Surface Weapons Center (NSWC). The facility used is a test chamber with 61-cm-thick, steel-reinforced concrete walls to contain the explosion and accompanying noise. It was equipped with a streak camera and a number of oscilloscopes. The Cordin 132 streak camera is capable of writing on the film at speeds up to 20 mm/ μ sec. Ancillary equipment for calibration and for synchronizing the recording equipment was also available. An explosive preparation facility was available to cast, machine, and press explosive charges to specifications. A computer facility consisting of a CDC 6400 computer and accessory equipment was available for use in data reduction.

The preparation of target components and their assembly was all done by the author. Preparation included the machining and lapping of most components. Assembly, preparation, and handling of explosive components were done by a technician, as required by operating procedures of the laboratory. This technician also assisted the author in optically aligning test assemblies for streak camera experiments. All other aspects of the

experiments were done by the author, except where otherwise indicated in the text.

Two quartz gage experiments were done at the Shock Dynamics Laboratory at Washington State University, whose facilities are described elsewhere.⁴⁰

3.2. Armco Iron Properties

A 10.2-cm-diameter, 61.0-cm-long bar of Armco Magnetic Ingot iron was obtained for this program. This large specimen was obtained to insure that similar test samples would be used throughout the course of the study. All samples for this program came from a 10-cm length of this bar and were used as received except for cutting, surface grinding, and lapping of sample faces. Metallurgical properties of iron and procedures for sample preparations are given below.

3.2.1. Metallurgical Properties

Impurities present in a single unshocked sample of Armco iron were obtained by the NSWC using wet chemical and spectrochemical analyses. The sample tested was 99.84 percent pure iron, and accuracy of the over-all analysis was better than 0.05 percent. Unmeasurable traces of silicon, nickel, chromium, and molybdenum were detected. Measurable amounts of carbon (0.14 percent), phosphorous (0.002 percent), sulfur (0.014 percent), manganese (0.025 percent), and copper (0.11 percent) were found. It was assumed that all samples maintained these purity limits even though no other measurements were made.

I used the water displacement method to measure an initial iron density of $7.868 \pm 0.012 \text{ gm/cm}^3$. Hardness values ranged from 69 to 71 on the Rockwell F scale for two different iron samples with faces surface-ground. No difference in hardness beyond experimental scatter was detected along diameter paths on the faces of the samples.

An unshocked iron sample from the center of the bar was polished and etched with a 2 percent Nital solution (2 cc of concentrated HNO_3 and 100 cc of amyl alcohol). Grains were irregular in shape and had an average diameter of approximately 0.1 mm. Signs of foreign material were evident in the photomicrograph.

3.2.2. Sample Preparations

Samples were cut with faces perpendicular to the bar axis. Each disc was turned to the desired diameter and its faces were surface-ground to the desired thickness, which ranged from 1 to 25.4 mm. Faces were then lapped to a flatness of less than 2 fringes measured with sodium light and an optical flat. An exception was the 25.4-mm-thick plate used to obtain the equilibrium transformation stress. This iron plate would not fit the available lapping wheel and was therefore hand lapped on 600 grit paper placed on a flat layout table. Its final flatness measured less than 20 fringes using sodium light and an optical flat. The two faces were parallel to better than 12μ for all samples as measured by a dial indicator.

3.3. Types of Experiments

The three types of experiments performed in this work are summarized in Table 3.1. In elastic precursor experiments, the iron samples were impacted by an aluminum projectile. Stress histories were obtained by recording with oscilloscopes the current output of a quartz gage affixed to the rear face of the sample. In plate slap experiments the iron samples were impacted by an aluminum flier plate. In the explosively driven experiment, the 25.4-mm-thick iron sample was impacted by a detonation wave. In plate slap and explosively driven experiments, shock wave transmission times and free surface velocities were determined by recording with a streak camera changes in the amount of light being reflected from the surfaces of mirrors.

All experiments were designed to be one-dimensional. Lateral relief from the sides of samples during the recording time was avoided by maintaining a sample ratio of diameter to thickness greater than three. The only two-dimensional hydrodynamic effects present were those induced by tilted or unavoidably curved shock fronts.

3.4. Elastic Precursor Experiments

Two elastic precursor experiments were performed using the gas gun facility at Washington State University. Experimental details for these were essentially the same as reported elsewhere.⁴¹

TABLE 3.1.--Types of experiments

Name of Experiment	Accelerating System	Intermediate Materials	Impact System
Elastic precursor	WSU gas gun	Aluminum projectile/ vacuum	Projectile impacting iron
Plate slap	2,4,6-Trinitrotoluene (TNT) ^a	Naval brass/ aluminum/vacuum	Aluminum impacting iron
Explosively driven	Ammonium perchlorate (AP) ^a	Detonation shock impacting iron

^aInitiated by Pentolite plane wave boosters.

3.5. Plate Slap Experiments

Shock wave transmission experiments were performed on thin samples of Armco iron in which final driving stress was near 200 kbar. Specific details of plate slap experiments are given in the following subsections. Included are discussions of flier system, target construction, and laboratory methods.

3.5.1. Flier Plate System for Plate Slap Experiments

The shock wave system is illustrated in Fig. 3.1. The system consists of a plane wave explosive booster (a), a cast 2,4,6-Trinitrotoluene (TNT) pad (b), a brass plate (c), an aluminum flier plate (d), a vacuum chamber (f, g, and k), and a target (g) which holds the iron sample. Reproducibility of the system was about 18 percent, as indicated by the range of free surface velocities (1.01-1.19 mm/ μ sec) obtained for the plastic II shock in iron.

The difference in impedance between the 2.54-cm-thick brass plate and the 0.32-cm-thick aluminum plate causes the brass-aluminum interface to go to zero pressure when backward-facing relief waves from the free surface of the aluminum plate reach the interface. The aluminum flier plate separates from the brass plate and flies free. It travels 12.7 mm through vacuum at an average velocity of 1.6 mm/ μ sec before impacting the iron samples. The time required for a flier plate to travel the 12.7 mm was approximately 8 μ sec, which is sufficient time for eight wave reverberations to occur in the plate before impacting the iron sample.

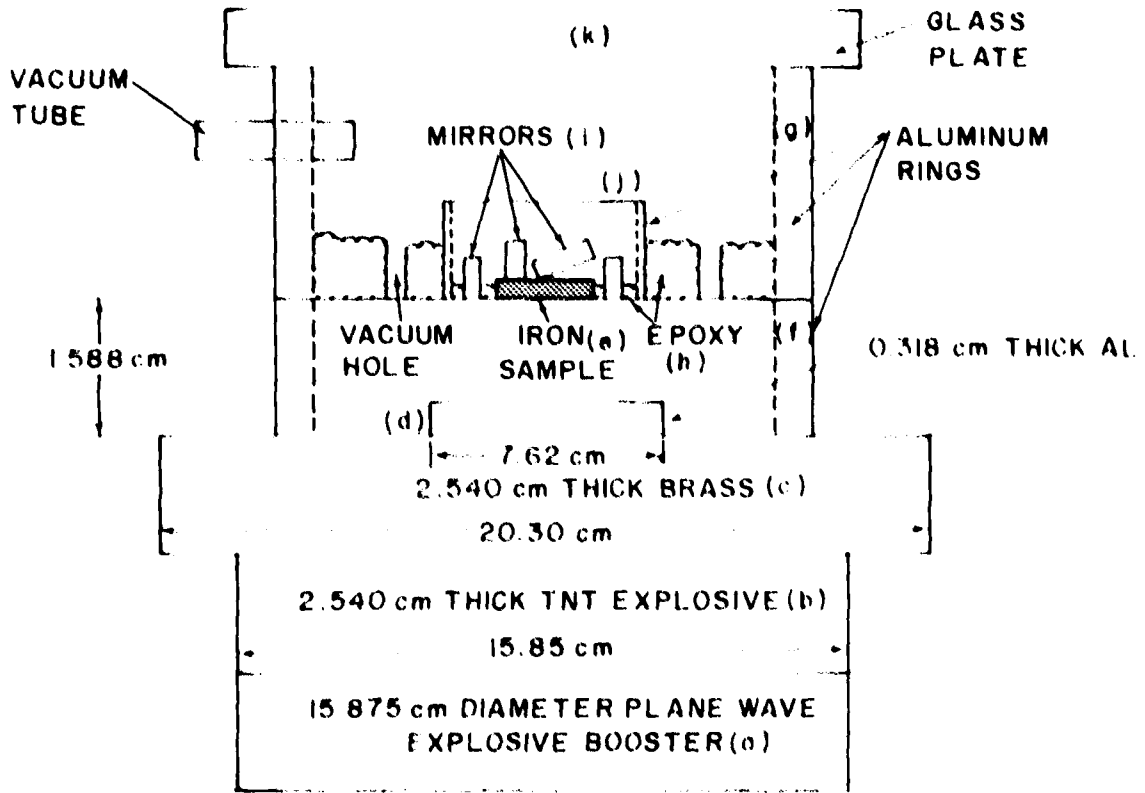


FIGURE 3.1 FLIER PLATE SYSTEM FOR PLATE SLAP EXPERIMENTS.

Spalling of the flier plate was believed not to occur though this was never proved. A graphical solution⁴², ignoring Taylor relief waves from the explosive gas products, indicates a maximum tension of about 35 kbar is first produced near the rear boundary of the flier plate. Therefore, if the plate spalled near the rear surface, it would not affect the present results because the thicker front of the plate drives the shock for a time ample for all measurements.

A graphical solution treating the elastic-plastic behavior of aluminum was carried out for times $t < d/c$, where d is flier plate thickness, c is longitudinal wave velocity in aluminum, and $t=0$ is the instant of separation of aluminum flier from the brass driver. The magnitude of the tension waves was reduced by at least 6 kbar in this time. The attenuation occurs because elastic waves overtake the slower plastic relief waves. The physics of this attenuating process has been treated elsewhere.⁴³ At the time of impact with the iron sample the aluminum flier plate is assumed to be stress free.

All flier plates were tilted less than 4×10^{-3} rad relative to the target face. In a special experiment wherein a transparent glass plate was used in place of the iron sample, flier plate impact on the glass plate was simultaneous to 0.012 μ sec over a central area with diameter of 30 mm. Flier plate edges arrived at the glass plate slightly ahead of the center portion, but not enough for their impact to perturb the iron samples and interfere with free surface measurements.

3.5.2. Target Preparation for Plate Slap Experiments

As shown in Fig. 3.1, the target consisted of a 15.24-cm-diameter aluminum ring (g), a 5.08-cm-diameter aluminum ring (j), the iron sample (e), mirrors (i), and epoxy (h). The 15.24-cm-diameter aluminum ring (target ring g) served to house the rest of the components and as part of the vacuum chamber. A 0.64-cm-thick piece of plate glass which served as the top of the vacuum chamber allowed mirrors to be viewed by the streak camera. The target ring was machined so that there was a small angle between the top glass and the iron surface to insure that light reflections from glass surfaces would not reach the camera. The target ring also had inserted through its wall a copper tube with 1.27-cm inner diameter to allow pumping of a vacuum. Pressures of less than 0.03 bar were obtained.

To insure reproducibility of the shock system, all dimensions of the component parts were maintained from shot to shot within 0.005 cm. Brass plate, aluminum flier plate, and spacing ring surfaces were parallel to within 0.0038 cm. The brass plate and aluminum flier plate faces were flatter than 2 light fringes as measured with sodium light using an optical flat. Mirrors were cut from a large, optical quality, front-silvered mirror, flat to 1 light fringe as measured using sodium light and an optical flat.

Tilted mirrors were placed on the iron samples with one edge of the silvered side in contact with the iron surface. A contact where no transmitted light was visible was considered

satisfactory. The contact edge of the mirror was placed far enough away from the edge of the iron sample to avoid interference from edge effects. The opposite end of the mirror was propped up by a jeweler's drill to obtain the desired angle (typically 2 deg) with the iron surface. The jeweler's drill was removed after the mirror was fixed securely in place with epoxy. Mirrors with small angles of inclination were used to insure that the gap between iron and mirror surfaces closed before wave interactions in the mirrors could affect the measurements.

The angle between tilted mirror and iron surface was measured with a shadowgraph instrument which is accurate to 1 min of arc. The iron impact surface opposite the surface with mirrors was used as a reference plane for the angle measurement. Since iron surfaces were parallel to better than 12 μ , any errors in the measured angle due to this lack of perfect parallelism were smaller than could be measured. Some tilted mirror angles were also measured, using a spectrometer table, by observing with a telescope the superimposition of a cross-hair and its image reflected alternately from the tilted mirror and the flat mirror against the iron surface. Angles could be measured in this way to within 0.5 min of arc. The remeasured angles agreed within 1.5 min of arc with shadowgraph measurements.

The target assembly of Fig. 3.1 was similar to that for precursor experiments discussed elsewhere.⁴¹ A target blank was built by wringing the target ring (g) down against a flat plate.

The flat plate was hand lapped on 600 grit paper to a flatness better than 2 sodium light fringes as measured with an optical flat. The small ring (j) was also wrung down against the flat plate near the center of the larger ring. The small ring eventually housed the iron sample (e). Vacuum grease between surfaces and on the entire face of the flat plate insured easy removal of the ring from the plate after the epoxy had been poured and cured. Epoxy (Shell Epon 815 mixed 4/1 by weight with a T-1 hardener) was poured inside the large ring to a thickness of 1.27 cm. The smaller ring was left blank at this stage of target preparation. The epoxy was poured in increments of 50 gm and each increment was allowed to cure before the next was poured. The target blank was then removed from the flat plate and vacuum holes were drilled in the epoxy to allow air to flow to the vacuum line from the chamber where the flier plate was located.

The target blank was hand lapped on 600 grit paper on a layout table to obtain a flat surface; it was then wrung down on the flat plate with vacuum grease. Two 0.64-cm-wide and 1.27-cm-long mirrors were wrung down against the flat steel plate next to the iron sample to measure the flier arrival and flier tilt. The iron sample and flat mirrors in the impact plane were then epoxied in place. The first three or four experiments used the Shell epoxy to fix the sample and mirrors in place. It was discovered that for thin samples (1.5 mm or less) a stronger, more viscous epoxy (Epoxi-Patch Kit 1C) was better suited to this purpose. The completed target was then removed

from the flat plate. Further lapping could not be done at this point because the silver would be removed from the mirror surfaces located at the impact plane.

This lack of a final lapping contributed slightly to the tilt, since sample and mirrors could not be put down perfectly flat. Indeed, tilts observed from this flier system were 1 order of magnitude greater than that obtained in the precursor experiments. Not all of this can be ascribed to lack of the final lapping; there are many factors other than this contributing to tilt. I concluded that imperfections in design and construction of the explosive plane wave booster were the main source of the observed tilt. These were beyond the control of the author, and it was therefore concluded that tolerances and methods of target preparation used were adequate. A better plane wave booster would be required to justify closer tolerances in target preparation.

3.5.3. Laboratory Methods

The target and explosive charge were mounted inside the test chamber on a leveled table. The table was placed so that the target assembly could be viewed through the slit of a rotating mirror streak camera aligned along the centers of the tilted mirrors. A diagram of the setup is shown in Fig. 3.2. Light from an exploding wire light source was reflected from mirror surfaces located in the target and intercepted by the camera. Incident light on the mirrors was at a slight angle from the normal to the target to allow convenient placement of the light

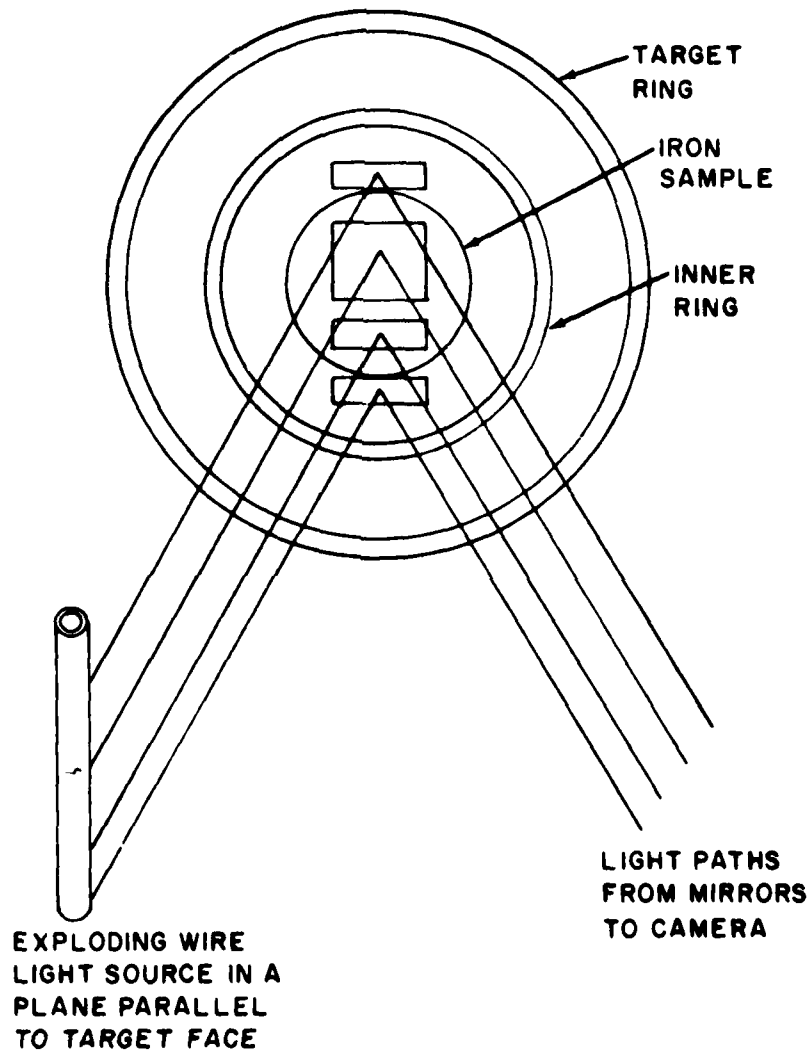


FIGURE 3.2 DIAGRAM SHOWING RELATION OF EXPERIMENTAL TARGET, LIGHT SOURCE, AND CAMERA FOR TRANSMISSION EXPERIMENTS.

source. Alignment of the experiment with the camera was accomplished by projecting light through the camera lens and slit out into the test chamber, where it was incident on the reflecting surfaces of the mirrors. These surfaces then reflected the light, at a small angle from the normal to the target surface, onto the glass capillary tube surface of the light source. This insured that light source and mirrors were properly aligned with the camera.

The Cordin 132 streak camera was outside the explosive chamber and protected from blast by a 2.54-cm-thick glass viewing window. The camera was focused on a precision grid placed on the surface of the target. A still picture was taken and developed before every experiment to verify focus. The camera was also run at the same writing speed used in the experiment and an aligned light wire source was exploded to check the amount of light available for the experiment.

The exploding wire light source was a 0.005-cm-diameter tungsten wire with resistance of 3.4 ohm, inside a 10.15-cm-long glass capillary tube having an outer diameter of 0.74 cm and an inner diameter of 0.15 cm. Experience has shown this to be a good light source. Air inside the capillary was shocked to luminescence by discharging a 3 μ F capacitor, which has been charged to 8000 V, through the tungsten wire. The capacitor power supply was connected to the wire by a 3.7-m-long, 10,000-V test prod wire (18 AWG).

Kodak TRI-X 70-mm-wide film was used in the streak camera. It was developed in Kodak D-11 developer and fixed in Kodak

Rapid fixer. The film's dynamic spatial resolution for this experimental setup of >300 lines/cm was measured in a special experiment by successfully recording the image of a Ronchi ruling as a function of time for a camera writing rate of 15 mm/ μ sec. Time resolution of the camera is a function of camera speed, rotor mirror distortion, spatial resolution, slit width, film characteristics, and ability to read the film record. A good estimate of time resolution is obtained by dividing slit width by camera speed. This estimate gives a time resolution of 0.0033 μ sec for a camera writing speed of 15 mm/ μ sec and a slit width of 0.05 mm. Possible errors in data due to time resolution, spatial resolution, and other such reasons are discussed in Appendix C.

3.6. Explosively Driven Experiments

An explosive shock system in contact with a 25.4 -mm-thick iron sample was used to obtain free surface data for driving stress near 250 kbar. The explosive shock system consisted of a plane wave booster in contact with a 2.54 -cm-thick pressed ammonium perchlorate (AP) explosive pad. The AP particle diameters were less than 10 μ before pressing to a density of 1.3 gm/cm³. Faces of the charge were machined to parallelism better than 0.0038 cm over a 12.7 -cm diameter. Faces of the charges were gently hand lapped on a layout table with 600 grit paper to insure a flat surface.

An AP pad was chosen principally because of the 250 kbar stress it induces in iron and the observed improvements in

planarity of the shock front, compared to the shock from the plane wave booster along. For example, arrival of a shock wave at the free surface of a 1.27-cm-thick aluminum plate driven by this explosive system was simultaneous to better than 0.04 μ sec over an area with a 5.93-cm diameter. Typical shock wave tilts resulting from this explosive system were 5×10^{-3} rad.

Laboratory methods and target preparations for these experiments were similar to those for plate slap experiments.

CHAPTER 4
EXPERIMENTAL RESULTS

Experimental results for two precursor experiments, one transmission experiment on a thick sample, and eight transmission experiments on thin samples are reported in this chapter. Stresses behind shock fronts were inferred from measured free surface velocity and average shock velocity. Elastic data required for calculation of stress behind the plastic I shocks were taken from Taylor and Rice's paper on Armco iron.³⁶

Errors have been reported in the shorthand form " $A \pm \epsilon$ " where ϵ is the average deviation of A. Appendix C treats the error analysis in some detail.

4.1. Elastic Precursor Data

Two precursor experiments were performed for different driving stresses. Sample thicknesses were 3.1 and 6.3 mm; results are summarized in Table 4.1 and in Fig. 4.1. The final stresses in iron were determined by the intersection of the equilibrium P-u curve of iron and the reflected P-u curve of aluminum, the aluminum curve being centered at $P=0$ and $u =$ projectile velocity.

The solid line in Fig. 4.1 was inferred from Taylor and Rice's³⁶ free surface velocities. Precursor stresses reported here are slightly lower than the solid line in Fig. 4.1.

TABLE 4.1.--Elastic precursor amplitudes in Armco iron

Sample Thickness (mm)	Stress in Quartz (kbar)	Precursor Stress in Iron (kbar)	Flier Plate Velocity (mm/ μ sec)	Driving Stress in Iron (kbar)
3.15	5.99	12.60 \pm 0.54	0.346 ^a	41.1
6.38	4.89	10.28 \pm 0.52	0.486 ^a	54.5

^aFlier plate material was 6061 T-6 aluminum.

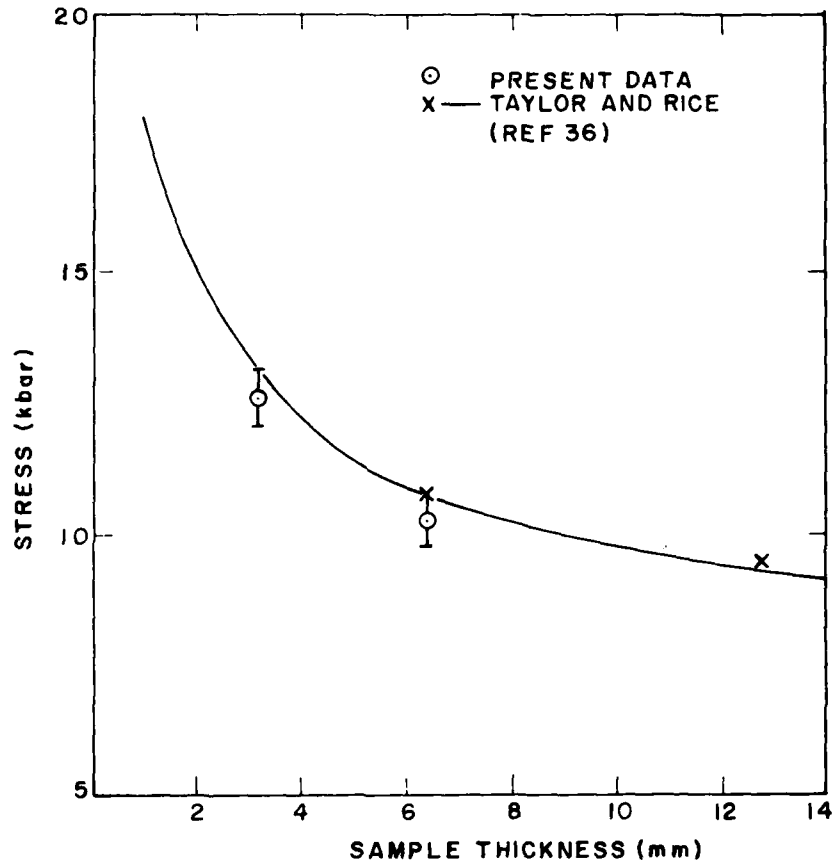


FIGURE 4.1 ELASTIC PRECURSOR STRESS AS A FUNCTION OF SAMPLE THICKNESS.

Deviations of these two data points from the line are within experimental error; discussion will be deferred to Section 6.2.

4.2. Transmission Data for a 25.4-mm-Thick Sample

A single experiment was performed to obtain stress behind the plastic I shock on a thick sample. Results are used as a reference for thin sample results. A stress of 131.4 ± 3.3 kbar was inferred from measured free surface velocity of 0.653 ± 0.0117 mm/ μ sec and an average measured shock velocity of 5.082 ± 0.090 mm/ μ sec. A Hugoniot elastic limit (HEL) of 8.3 kbar was used for the plastic I stress calculation.³⁶ This result agrees well with Bancroft, Peterson, and Minshall's² value of 131.0 kbar for a 24.7-mm-thick Armco iron sample.

4.3. Transmission Data for Thin Samples

Eight transmission experiments were performed at approximately 201-kbar driving stress. Sample thicknesses ranged from 0.94 to 6.31 mm. Free surface motion and average shock velocities for the iron samples were measured.

4.3.1. Plastic I Data

Table 4.2 summarizes results for the plastic I shock. The table includes sample thicknesses, free surface velocities, average shock velocities, and shock wave transit times. Dependence of free surface velocity, stress, and stress jump, $P_3 - P_2$, on sample thickness is shown in Figs. 4.2 to 4.4. These plots show small dependence of free surface velocity and stress on

TABLE 4.2.--Plastic I data

Sample Thickness (mm)	Elastic Wave Stress ^a (kbar)	Plastic I Wave Velocity (mm/ μ sec)	Plastic I Free Surface Velocity (mm/ μ sec)	Plastic I Stress (kbar)	Transmission Time (μ sec)
0.941	18.0	5.224 \pm 0.117	0.679 \pm 0.029	142.6 \pm 6.7	0.180 \pm 0.004
0.998	17.7	5.081 \pm 0.243	0.673 \pm 0.024	137.3 \pm 8.7	0.209 \pm 0.013
1.556	16.1	5.275 \pm 0.139	0.652 \pm 0.020	137.6 \pm 5.4	0.296 \pm 0.007
2.022	15.0	5.267 \pm 0.093	0.676 \pm 0.020	142.2 \pm 4.9	0.384 \pm 0.007
2.609	13.9	5.106 \pm 0.085	0.660 \pm 0.022	134.8 \pm 4.9	0.510 \pm 0.008
3.132	13.1	5.030 \pm 0.106	0.668 \pm 0.058	134.5 \pm 11.8	0.624 \pm 0.013
4.690	11.6	5.085 \pm 0.054	0.666 \pm 0.015	135.0 \pm 3.4	0.926 \pm 0.009
6.350	10.7	5.157 \pm 0.083	0.663 \pm 0.013	136.2 \pm 3.5	1.231 \pm 0.017

^aThese data are from Taylor and Rice. 36

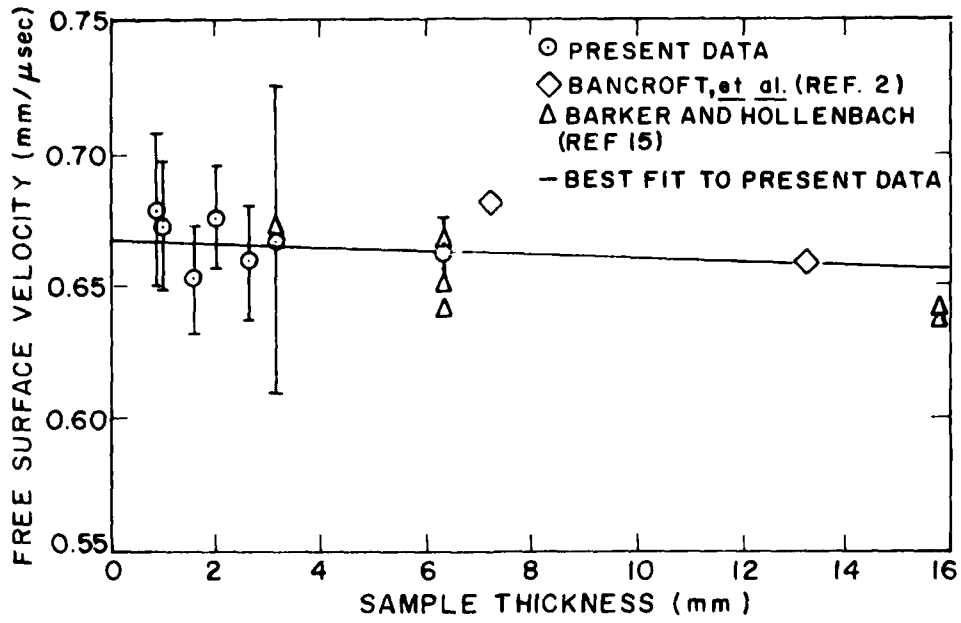


FIGURE 4.2 FREE SURFACE VELOCITY OF IRON AFTER PLASTIC SHOCK ARRIVAL.

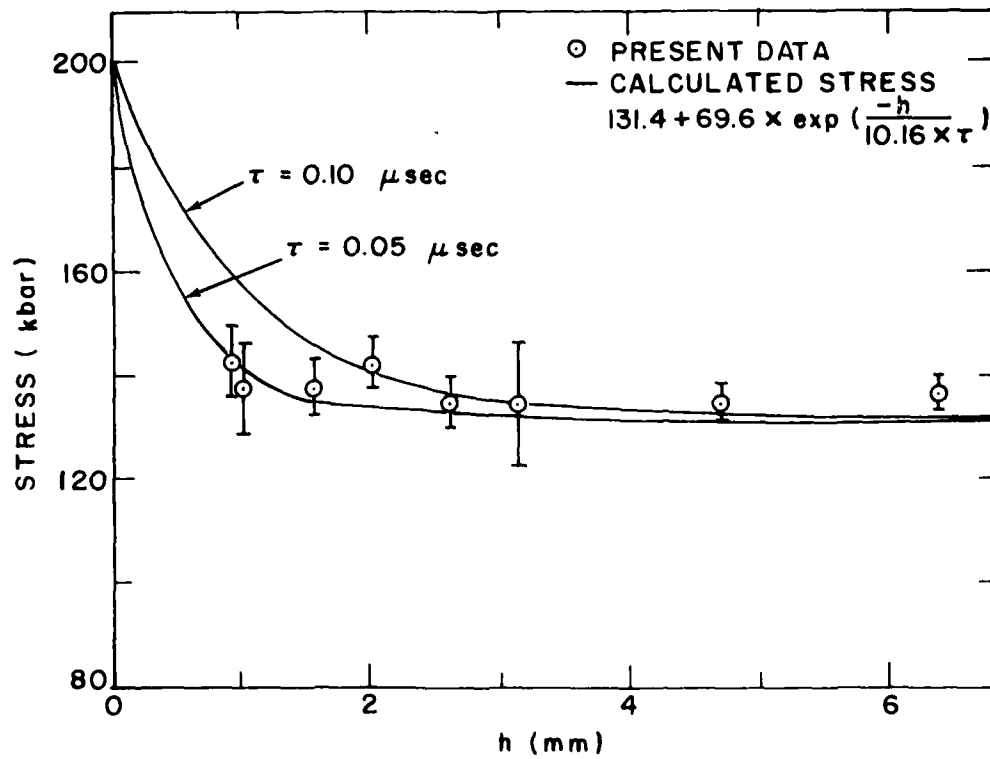


FIGURE 4.3 STRESS BEHIND THE PLASTIC I SHOCK IN IRON AS A FUNCTION OF SAMPLE THICKNESS.

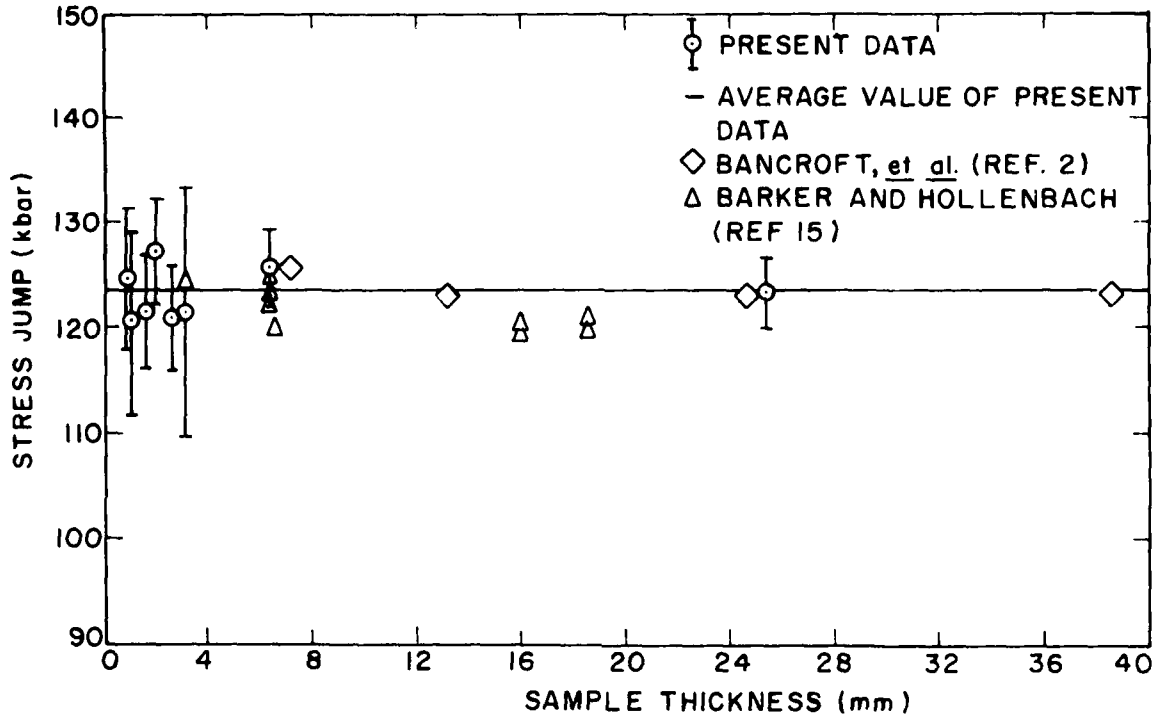


FIGURE 4.4 STRESS JUMP ACROSS THE PLASTIC I SHOCK AS A FUNCTION OF SAMPLE THICKNESS.

sample thickness. The plot of stress jump versus thickness implies that the increase in stress behind the plastic I front for small sample thicknesses may be accounted for by the known increase in stress of the precursor as sample thickness is decreased.

Figure 4.2 shows free surface velocity versus sample thickness; data from two additional sources are shown for comparison. These other data points result from experiments using different experimental techniques and different final driving stresses. The solid line is a least-squares fit of present data to a straight line. It corresponds to an increase in free surface velocity of about 0.1 percent for every 1-mm decrease in sample thickness. Its slope is not significantly different from zero.

Stresses behind the plastic I shock in iron versus sample thickness are shown in Fig. 4.3. In addition, two solid curves are present which are calculated from the phenomenological model of Duvall and Horie²⁰ for two different relaxation times. Comparison between calculated curves and experimental data shows that relaxation time, τ , is obviously less than 0.1 μ sec. The significance of this will be discussed in Section 6.1.

The data in Fig. 4.3 show a slight increase in stress for decreasing sample thickness. Stress is about 140 kbar for a sample thickness of 1 mm and about 136 kbar at 6.35 mm. The 140-kbar value is 9 kbar greater than the stress measured for the 25.4-mm-thick sample reported in Section 4.2.

This increase in stress for decreasing sample thickness is not very significant.

Stress jumps across the plastic I shock versus sample thickness are shown in Fig. 4.4. Precursor amplitudes were taken from Fig. 4.1. The solid line represents the weighted average of the stress jump for the present results. The stress jump appears constant. Deviations from this constant value of 123.6 ± 1.6 kbar for all the data are within experimental error. Constancy of the stress jump implies that the increase in plastic I stress for decreasing sample thickness shown in Fig. 4.3 may be due to the increase in precursor stress.

4.3.2. Plastic II Data

Table 4.3 summarizes results for the plastic II shock in iron. These results are from the same experiments as those that produced the plastic I data of Table 4.2. The table includes sample thicknesses, free surface velocities, shock wave transmission times, and rise times of the plastic II shock front. "Beginning" of the plastic II wave front refers to the time at which free surface velocity begins to exceed the plastic I value. "Top of the wave" refers to the time when free surface velocity again becomes constant or nearly so. Plastic II results are used here primarily to determine a best value for Lagrangian velocity of the wave front and to obtain the best possible pressure-volume (P-V) point from the data set.

Plastic I and plastic II shock wave arrival times at the free surface for various sample thicknesses are shown in Fig. 4.5.

TABLE 4.3.--Plastic II data

Sample Thickness (mm)	Plastic II Free Surface Velocity (mm/ μ sec)	Transmission Time for Beginning of Wave (mm/ μ sec)	Transmission Time for Top of Wave (μ sec)	Rise Time of Wave Front (μ sec)
0.941	1.054 \pm 0.040	0.255 \pm 0.010	0.446 \pm 0.020	0.191 \pm 0.022
0.998	1.186 \pm 0.021	0.306 \pm 0.018	0.503 \pm 0.026	0.197 \pm 0.032
1.556	1.141 \pm 0.023	0.448 \pm 0.026	0.652 \pm 0.026	0.204 \pm 0.037
2.022	1.153 \pm 0.031	0.547 \pm 0.021	0.684 \pm 0.034	0.137 \pm 0.040
2.609	1.079 \pm 0.032	0.677 \pm 0.027	0.842 \pm 0.048	0.165 \pm 0.055
3.132	1.012 \pm 0.040	0.832 \pm 0.031	1.008 \pm 0.029	0.176 \pm 0.043

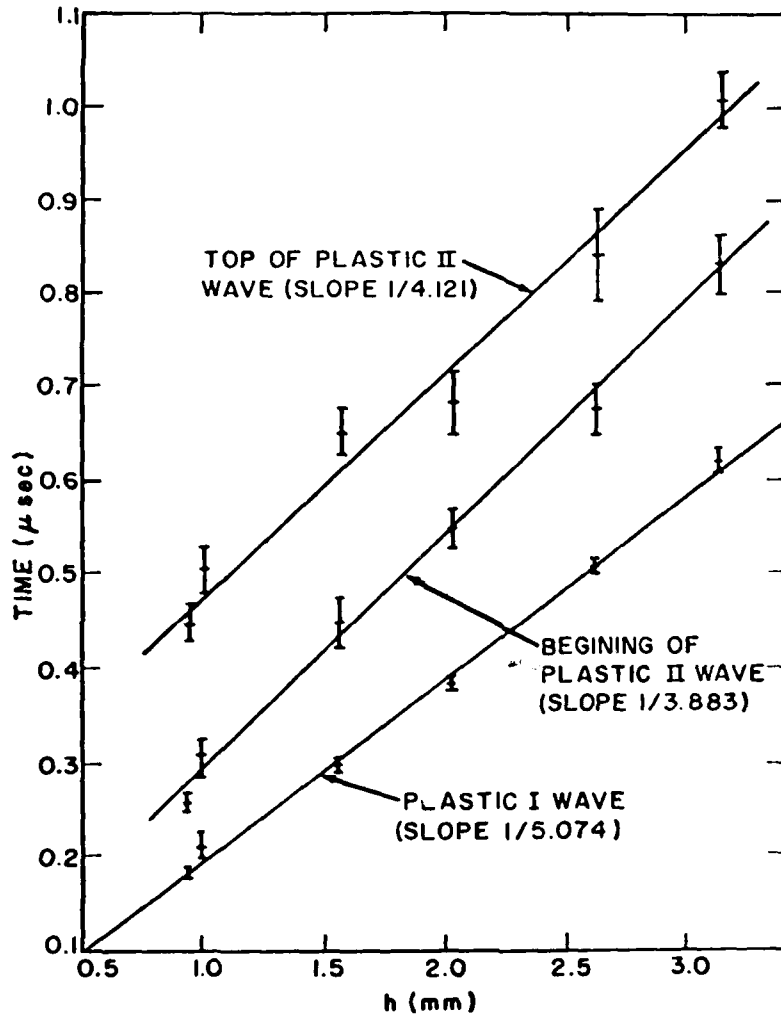


FIGURE 4.5 SHOCK WAVE ARRIVAL TIMES AT FREE SURFACES.

The arrival times were fit by least squares to straight lines, with arrival time taken as the independent variable and sample thickness as the dependent variable. Each arrival time was assigned a weighting factor proportional to the inverse square of its error. Differences in final stress reached in the iron samples were ignored when determining Lagrangian velocity of the plastic II shock wave.

Lagrangian velocities obtained by this procedure are:

$$\text{plastic I wave, } U_2' = 5.074 \pm 0.045 \text{ mm}/\mu\text{sec}$$

$$\text{beginning of plastic II wave, } U_{3B}' = 3.883 \pm 0.138 \text{ mm}/\mu\text{sec};$$

$$\text{top of plastic II wave, } U_{3T}' = 4.121 \pm 0.235 \text{ mm}/\mu\text{sec}$$

The beginning plastic II wave path intersects the $h=0$ plane at $t = 0.23 \pm 0.017 \mu\text{sec}$. The top of the wave front appears to propagate slightly faster than the bottom, but errors in the velocities do not allow any significance to be assigned to this observation. In fact, the error bars are of such large magnitude that no conclusion about steadiness of the wave front can be drawn from the data of Fig. 4.5.

The $h-t$ plots of shock transmission times in Fig. 4.5 do not represent the true paths of the initial forward-facing plastic shocks because of interactions with backward-facing waves from the free surfaces, described in Section 2.2. Corrections to the plastic I path are negligible because of the small amplitude of the precursor reflection. Values of (h,t) points for the beginning of the plastic II wave, corrected according to Eqs. (2.9) and (2.10), are shown in Fig. 4.6. The rectangles represent estimated errors for each point. The fitted line

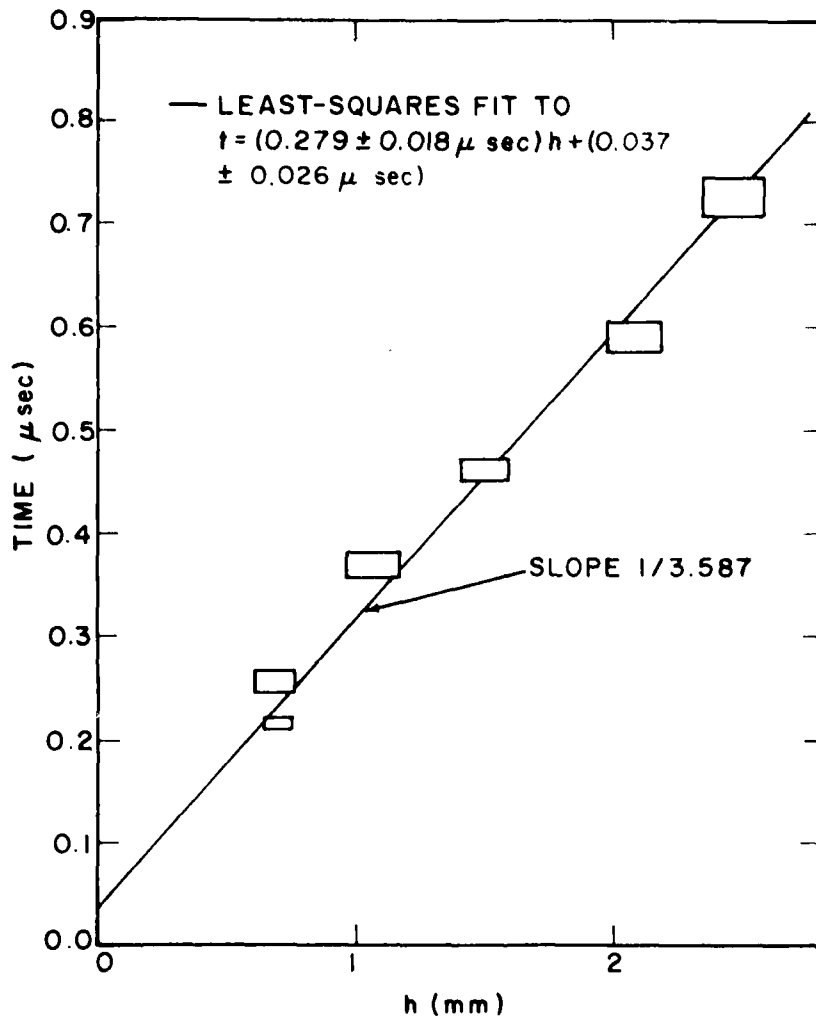


FIGURE 4.6 CORRECTED LAGRAGIAN h-t DIAGRAM FOR BEGINNING OF THE PLASTIC II FRONT.

corresponds to a velocity of 3.587 ± 0.227 mm/ μ sec, which is slightly less than that obtained for the uncorrected data of Fig. 4.5.

4.3.3. Stress-Volume State Behind the Plastic II Shock

The stress-volume state behind the plastic II shock was calculated using the equilibrium jump equations, Eqs. (2.4) and (2.5); weighted averages of plastic I and plastic II particle velocities; and Lagrangian shock velocities from the preceding section:

$$u_1 = 0.032 \pm 0.005 \text{ mm}/\mu\text{sec},$$

$$u_2 = 0.333 \pm 0.004 \text{ mm}/\mu\text{sec},$$

$$u_3 = 0.565 \pm 0.018 \text{ mm}/\mu\text{sec},$$

$$U_1' = 6.18 \pm 0.21 \text{ mm}/\mu\text{sec},$$

$$U_2' = 5.074 \pm 0.045 \text{ mm}/\mu\text{sec},$$

$$U_3' = 3.587 \pm 0.227 \text{ mm}/\mu\text{sec},$$

$$P_3 = 201 \pm 8.4 \text{ kbar},$$

$$V_3/V_0 = 0.871 \pm 0.008,$$

$$V_0 = 7.098 \pm 0.011 \text{ cc/mol.}$$

This stress-volume point is given in Fig. 4.7 along with data from Bancroft, *et al.*,² data from Barker and Hollenbach,¹⁵ and Andrews' equilibrium curve.²⁷ It is reasonably consistent with the Bancroft data and the Barker data.

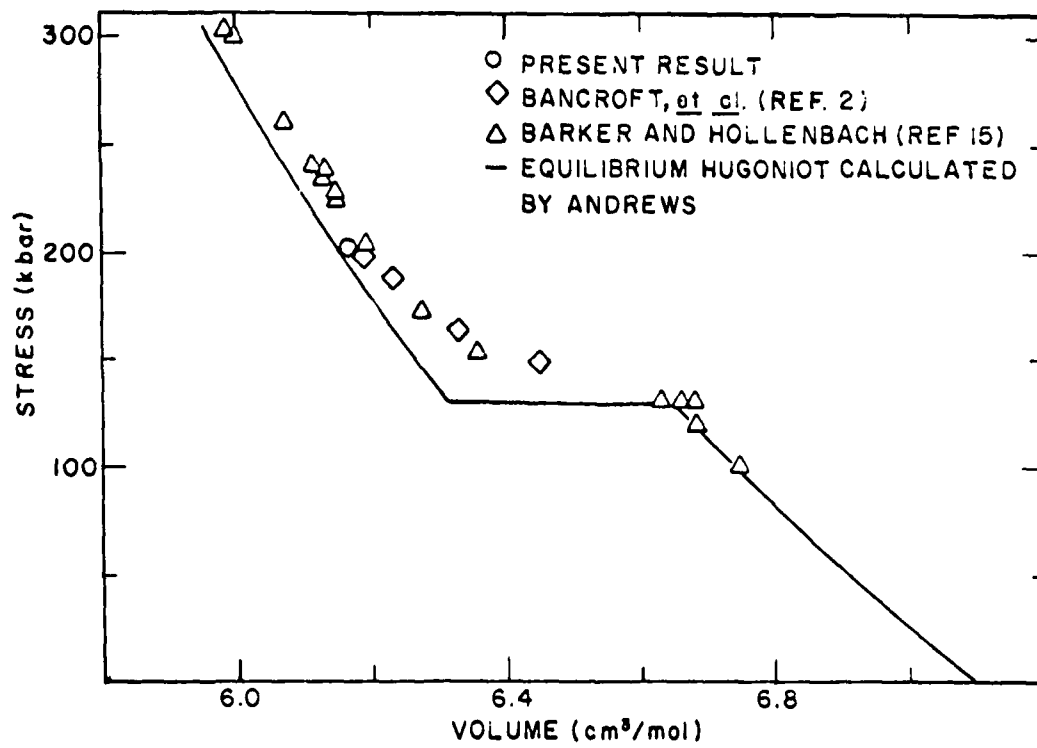


FIGURE 4.7 IRON HUGONIOT STATES.

4.4. Summary

The most significant experimental result of this study is shown in Fig. 4.3 and 4.4: There is little or no variation of plastic I wave amplitude for propagation distances between 0.9 and 6.35 mm. This implies, according to Fig. 4.3, a relaxation time of about 0.05 μ sec for onset of the $\alpha \rightarrow \epsilon$ transition. When the single measurement of 25.4-mm distance is included with close-in data, one infers a slow variation of transition stress with distance, superimposed on the rapid decay below 1 mm. Inference of the initial decay depends on the assumption that initial compression at the impact surface was entirely in the α phase.

Further results, which are essentially corroborative, are that:

1. Elastic precursor amplitude increases as sample thickness is decreased.
2. Transition stress measured in a 25.4-mm-thick sample is 131.4 ± 3.3 kbar.
3. Relative volume behind the plastic II wave is $V_3/V_0 = 0.871 \pm 0.008$ for a stress of 201 ± 8.4 kbar.
4. Rise time in the plastic II shock front is $0.18 \pm 0.02 \mu$ sec.

These results are in essential agreement with those of earlier experiments reported in references 36, 2, 2, and 23, respectively

CHAPTER 5

THEORY OF THE ALPHA TO EPSILON TRANSFORMATION

In this chapter shock wave measurements on iron and metallurgical data on martensitic transformations are brought together in an attempt to produce a plausible description of the iron transformation.

5.1. Review of Experimental Information

The alpha to epsilon transformation in iron has been studied by several different investigators using different experimental techniques and varying different parameters. Salient results of these studies are summarized here.

5.1.1. Shock Experiments

Stress in the plastic I shock is a measure of the transformation stress, P^{TL} , for the compression or loading process. Some measurements of P^{TL} for 19- to 25-mm-thick iron samples are given in Table 5.1. Iron samples used have had different metallurgical histories and probably contained different trace amounts of impurities. Agreement among values of P^{TL} in Table 5.1 implies that trace amounts of impurities and different metallurgical histories do not affect P^{TL} significantly. Minshall²² has shown that work hardening and heat treating Armco iron slightly increases P^{TL} , but the transition volume remained

TABLE 5.1.--Iron transformation stress

Source	p^{TL} (kbar)
Bancroft, <u>et al.</u> (REF. 2)	131
Minshall (REF. 22)	132
Loree, <u>et al.</u> (REF. 44)	129 \pm 1
Barker and Hollenbach (REF. 15)	130 \pm 1
Present study	131 \pm 3

constant. Although trace amounts of impurities have little effect on P^{TL} , 1.5 percent of carbon increases P^{TL} by 5 kbar.⁴⁴

Barker and Hollenbach¹⁵ measured shock release states in iron and showed that the reverse transformation of epsilon to alpha iron is initiated at a stress, P^{TU} , of 98 kbar. The stress for equilibrium transformation lies between P^{TL} and P^{TU} . Their mean value is $P^T = 116$ kbar, for which $T = 332^\circ\text{K}$ on the Hugoniot.

The 6 percent decay in P^{TL} for wave propagation from 6 to 25 mm described in Chapter 4 is similar to other reported values.^{2,15} Measurements on specimens down to a thickness of 1 mm reported in Chapter 4 show that initial decay of the plastic I shock stress is very rapid. This observation is supported by Barker and Hollenbach in measurements on specimens of thicknesses of 3 mm and greater.¹⁵

Shock compression data on iron show that, for a given volume, measured stress in the mixed phase region exceeds that expected for the equilibrium Hugoniot.^{27,28} (See Fig. 4.7.) Transformation begins at 130 kbar and appears to be complete near 200 kbar. The slope, ≈ -5 Mbar gm/cm^3 (1 Mbar = 10^3 kbar), of the Hugoniot just above P^{TL} disagrees significantly with the slope for the equilibrium curve, which is about -0.1 Mbar gm/cm^3 . The equilibrium value is calculated for conditions of uniform hydrostatic pressure throughout the material. For various reasons, including anisotropy of stress, measured values of stress, P , differ from hydrostatic values,

\bar{P} , by unknown amounts, which may account for some of the differences in slopes. It is not certain that measured Hugoniot states in the mixed phase region are in equilibrium. They persist for the experimental time span and will be denoted "quasistatic" states.

Values of P^{TL} for various temperatures are given in Fig. 5.1. The Clausius-Clapeyron equilibrium relation and the equation of state given in Appendix A yield a value of -60.8×10^{-6} Mbar/ $^{\circ}$ K for $\frac{dP}{dT}$. This calculated slope is within experimental error of the observations of Johnson, et al.⁴⁵

5.1.2. Static Experiments

A number of static isothermal compression experiments on iron have shown that the transformation is initiated near 130 kbar and goes to completion for stresses greater than 145 kbar.^{32,33,34,35} Giles, et al.³² found values of 133 kbar for P^{TL} and 81 kbar for P^{TU} along a 300 $^{\circ}$ K isotherm. They also found that the alpha phase persisted for stresses above 163 kbar while Mao, et al.³³ report no signs of alpha iron above 145 kbar. Giles, et al.³² found that the epsilon phase persisted down to 45 kbar in the unloading process. The mean value for transformation stress, \bar{P}^{Teq} , reported by Giles, et al. was 107 ± 8 kbar, which is 9 kbar less than the mean value, P^{Teq} , reported by Barker and Hollenbach.¹⁵ Some of this difference may be due to different amounts of shear stress in static and dynamic experiments.

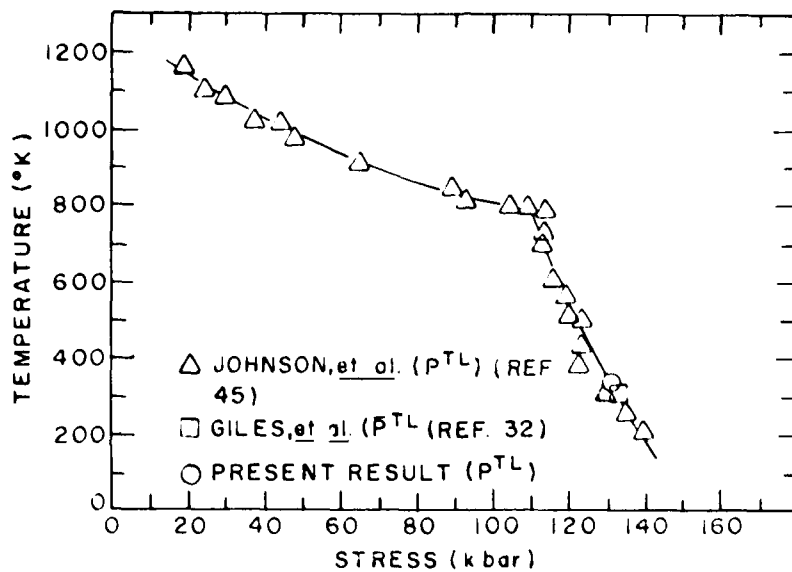


FIGURE 5.1 TRANSFORMATION STRESS FOR IRON UNDER COMPRESSION AT VARIOUS TEMPERATURES.

5.1.3. Discussion

Differences between the measured Hugoniot and calculated equilibrium Hugoniot may result from several causes including: (1) partial transformation, (2) transformation to a metastable state, (3) surface energy requirements for the new phase to nucleate, (4) strain energy requirements for accommodation of the new phase in the parent lattice, (5) effects of shear on the transformation, and (6) pre-existing new phase nuclei of various sizes.

The difference between P^{Teq} and \bar{P}^{Teq} is presumably due to shear. However, there exists no clear evidence that shear in iron is important to the phase transformation, except for effects of work hardening and heat treating prior to shock loading.²²

Several investigators have suggested that the alpha to epsilon transformation is martensitic. Giles, et al.³² make the strongest case based on: (1) the large difference between \bar{P}^{TL} and \bar{P}^{TU} , (2) existence of two phases over a large pressure range, and (3) simultaneous transformation of independent areas. These properties are all characteristic of martensitic transformations.

5.2. Characteristics of Martensitic Transformation

Martensitic transformations are defined in terms of process, not in terms of structure or properties. They require no diffusion of atoms; they are displacive or shearlike, in that the atoms move cooperatively to produce substantial shape changes

in the transforming region, even though each atom shifts only slightly relative to its neighbors. These diffusionless and displacive characteristics distinguish martensitic transformations from all other types.

Martensitic transformations produce lenticular plates with semicoherent interfaces between plates and parent lattice. Plates grow with a velocity near the speed of sound but stop growing when (1) a grain boundary, (2) another martensitic plate, or (3) other lattice disturbances which serve as barriers are encountered. The distribution of plate sizes within a grain is not well understood. Fisher⁴⁶ suggests that plates form randomly throughout each grain, constantly subdividing grains, so later generations of plates form in smaller and smaller parent volumes. Magee⁴⁷ has proposed a somewhat different order of growth in which nucleation is not random throughout each grain, so at any time some grains will contain martensitic plates and some will not. These plates tend to occur in clusters, with various-sized plates in each cluster. It has been observed that the first detectable amount of transformation is due to the presence of single clusters of plates⁴⁷ in several grains, in contrast with Fisher's model. Further transformation largely involves spreading of clusters to untransformed regions. To a first approximation, volume of newly-formed plates in a cluster is constant. This picture leads naturally to the conclusion that increments in volume of the new phase are proportional to increments in the number of nucleation centers activated.

5.2.1 Crystallography

Martensitic growth causes bulk shape changes, from such causes as tilting of the martensitic plates, which are visible at flat surfaces. The plates are surrounded by untransformed matrix and are usually lenticular, although in some steels "needles" or "laths" have been reported. These plates may in turn contain a fine structure of slip bands or twins as a direct consequence of the transformation process.⁴⁸

The martensitic plate has mirror symmetry about a plane, and this plane has a particular and reproducible orientation with respect to the parent phase for any lattice. The plane in the parent lattice which lies parallel to the symmetry plane of the martensitic plate is called the habit plane. It is the plane along which the principal shear displacement occurs in the martensitic reaction.

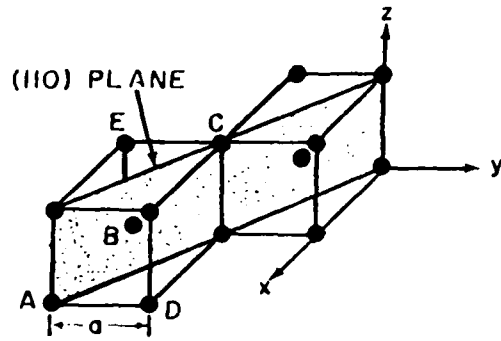
Consideration of experimental data on martensitic transformations has encouraged development of crystallographic explanations for any particular transformation of orientation relationships, habit planes, deformation shapes, and nature of the fine structure within the martensitic plates.

Bowden, et al.³¹ concluded that markings from recovered shocked alpha iron samples resulted from shear transformation to the epsilon phase, body-centered-cubic (bcc), to hexagonal-close-packed (hcp) and its reversal, which suggests that the transformation is martensitic. The shear mechanism, reviewed below, is essentially the same as proposed by Burgers⁴⁹ for the zirconium transformation.

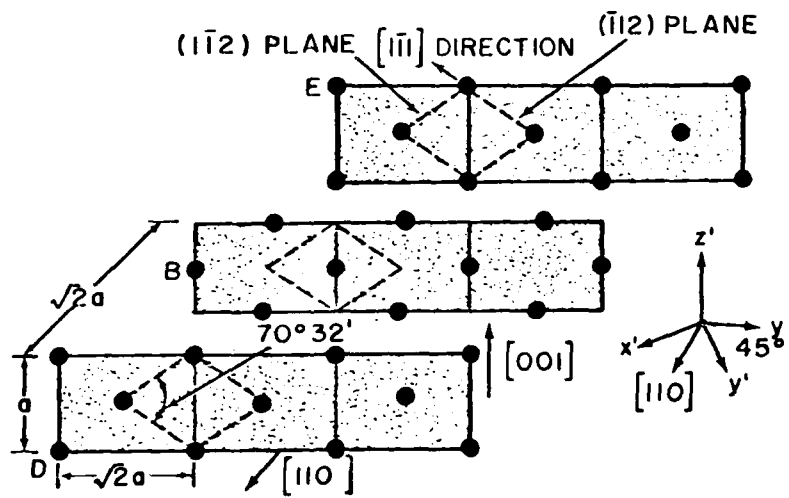
Some comments on notation are required. Lattice planes are defined by Miller indices with integer components (a', b', c') .⁵⁰ Directions in the lattice are given as vectors with integer components $[a, b, c]$. A bar above a component, such as (\bar{a}', b', c') , indicates a negative value. In cubic crystals, a direction $[a, b, c]$ is perpendicular to a plane (a, b, c) having the same indices.

A bcc cell has six different symmetric planes which are "most densely packed" (not close-packed): $(1\bar{1}0)$, (110) , (101) , (011) , $(0\bar{1}1)$, and $(\bar{1}01)$. Figure 5.2(a) shows a most densely packed (110) plane with rows of close-packed atoms such as A, B, and C along each cube diagonal. It is along these close-packed rows that slip, twinning, and some phase transformations take place due to applied shearing forces. These rows lie in either $(\bar{1}12)$ or $(1\bar{1}2)$ planes; e.g., the row ABC in Fig. 5.2(a) is in the $(1\bar{1}2)$ plane.

Changes in a particular triclinic cell illustrate how the bcc lattice can be transformed to hcp by shear deformation. In Fig. 5.2(b) three sequential (110) planes are represented in an isometric drawing; separations between planes are exaggerated for clarity. These planes are, for example, those containing atoms D, B, and E, respectively, as shown in Fig. 5.2(a). The triclinic cell of interest is outlined by dashed lines in Fig. 5.2(b) with four sides perpendicular to the (110) planes and lying in either the $(\bar{1}12)$ or $(1\bar{1}2)$ planes. It is along these sides that shearing action for the transformation will take place. The shear mechanism for transformation is



(a) TWO BODY CENTERED CELLS



(b) PARALLEL (110) PLANES IN A BODY CENTERED LATTICE

FIGURE 5.2 BODY CENTERED LATTICE.

easy to visualize if the triclinic cell is oriented as shown in Fig. 5.3(a). To obtain this orientation of the cell requires three rotations of the lattice with respect to the set of fixed coordinates in Fig. 5.2(a): (1) rotate the lattice around the z axis through an angle of $+45^{\circ}$, which gives the parallel (110) planes shown in Fig. 5.2(b); (2) rotate the lattice around the y axis by $+90^{\circ}$, which results in the (110) planes parallel to the xy plane; (3) rotate the lattice around the z axis through an angle of $-35^{\circ}15'$, which orients the triclinic cell as in Fig. 5.3(a).

The shear mechanism for bcc to hcp transformation is illustrated in Fig. 5.3(a) and (b) where a shear on the $(\bar{1}12)$ plane in the $[1\bar{1}1]$ direction changes the $70^{\circ}30'$ angle between the two sides in the basal plane to a 60° angle. The open circles in Fig. 5.3(b) represent atomic positions before shear. The resulting cell has hexagonal symmetry but is not close-packed because of the central atom. The central atom must be shifted, as indicated by the two open circles in the center plane of the cell of Fig. 5.3(b), to bring it into line with the interstitial position between the trio of atoms in the basal planes above and below. Further slight adjustments of cell dimensions are necessary for conformance with lattice parameters of the hcp phase.

The transition is initiated when a critical value of shear stress is exceeded for a row of close-packed atoms such as the $[1\bar{1}1]$ direction on the $(\bar{1}12)$ plane.

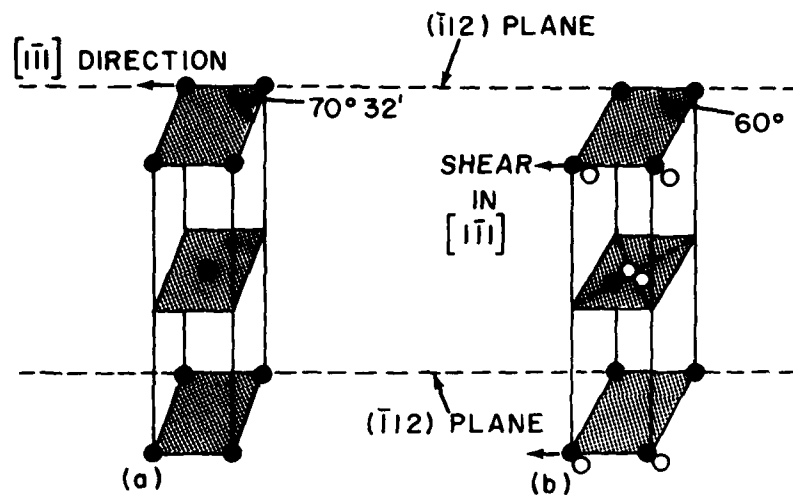


FIGURE 5.3 SHEAR MECHANISM FOR BODY-CENTERED-CUBIC TO HEXAGONAL-CLOSE-PACKED TRANSFORMATION.

5.2.2. Uniaxial Strain

It seems likely that uniaxial compression along certain crystallographic directions will activate the bcc to hcp transformation. The present search for possible uniaxial compression transformations is limited to compressions of the triclinic cell of Fig. 5.2(b).

This cell attains hexagonal symmetry by uniaxial compression in the $[001]$ direction; then the $70^{\circ}30'$ angle between sides in the basal plane becomes 60° . Due to the symmetry of cubic crystals six different planes exist which contain a triclinic cell like that of Fig. 5.2(b). However, there are only six directions of uniaxial compression which will produce hexagonal symmetry. Planes which contain triclinic cells and directions of uniaxial compression which transform the cell to hcp are:

<u>Plane</u>	<u>Direction</u>
($1\bar{1}0$)	$[001], [00\bar{1}]$
(110)	$[001], [00\bar{1}]$
(011)	$[100], [\bar{1}00]$
($0\bar{1}1$)	$[100], [\bar{1}00]$
(101)	$[010], [0\bar{1}0]$
($\bar{1}01$)	$[010], [0\bar{1}0]$

The relative displacement required to obtain the 60° angle is $a/a_0 = 0.816 =$ relative volume for uniaxial strain. To produce this compression in iron requires a shock stress near 400 kbar. The actual transformation occurs at 130 kbar, which

suggests that some other process is active at lower stresses or some local expansion occurs laterally.

5.2.3. Fraction Transformed

Theories of martensitic transformations have progressed to the point where the volume fraction transformed can be expressed as a function of time for constant temperature and pressure or as a time-independent function of temperature for constant pressure.⁴⁷ Transformations of the first kind are called "isothermal," the latter are called "athermal." Isothermal data show that reaction rate decreases rapidly during the course of transformation. This has been explained by Fisher⁴⁶ as a consequence of repeated subdivision of grains by succeeding generations of martensitic plates. Plates growing from any initiation site are stopped at grain boundaries or other plates so that, as a grain subdivides, the transformed volume growing from each nucleation site diminishes as in Fig. 5.4. If nucleation sites are activated at a constant rate, and if this rate is slow compared to individual growth rate, then it necessarily follows that volume transformation rate diminishes with time; the amount of material transforming depends on the amount of material available to transform. The "final" state reached in such experiments has been observed to contain a residue of phase 1.⁴⁷

In constant pressure athermal studies a sample is heated above the martensitic transition temperature, M_T , and rapidly cooled to a reference temperature below M_T . It is then examined

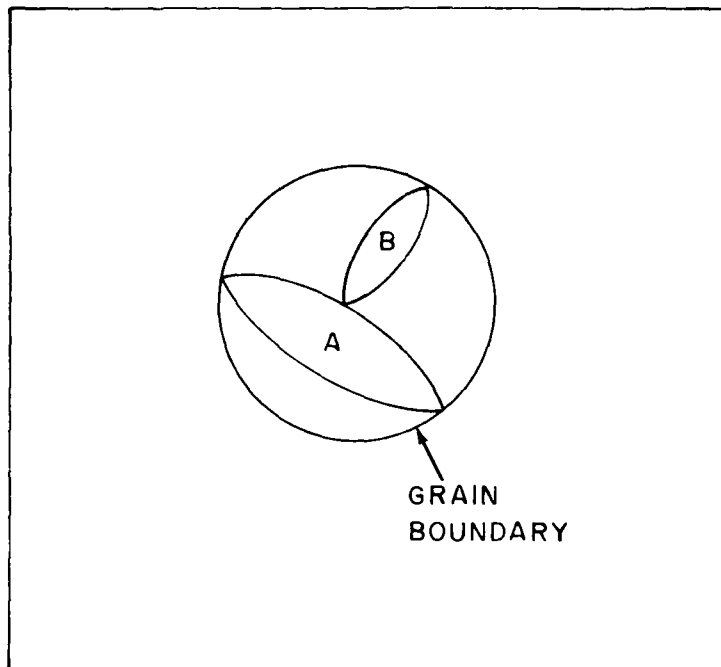


**FIGURE 5.4 SUBDIVISION OF A SINGLE GRAIN BY MARTENSITIC PLATES.
A AND B ARE FIRST AND SECOND GENERATION PLATES,
RESPECTIVELY.**

for the amount of martensite formed. The amount of martensite formed has been found proportional to the difference between transformation temperature and the lower reference temperature and independent of time, within the resolution of such experiments.

5.2.4. Fraction Transformed in Athermal Transformation

Athermal martensite appears to grow from a finite number of nucleation sites, which are eventually exhausted. Magee⁴⁷ has been successful in explaining athermal results by assuming the number of new plates in the untransformed volume to be proportional to increments in "driving force," $G_{21} = G_2 - G_1$, where G_2 and G_1 are the Gibbs energies for phases 1 and 2, respectively, at the existing pressure and temperature. He has proposed that the number of new sites per unit volume, dN , available to transform is

$$dN = -K(1-f') d(G_2 - G_1) \quad (5.1)$$

where K is a positive constant and f' is volume fraction of martensite.

This equation contains the implicit assumption that the final state is the state for which $f' = 1$, whereas observations show that $f' = 1$ is never quite reached.

If each cluster of plates contains nearly the same volume of martensite, then the volume fraction transformed is proportional to the number of new plates formed per unit volume:

$$df' = V_p dN \quad (5.2)$$

where V_p is the constant average plate volume of a cluster. This treatment of plate volume is different from Fisher's⁴⁶ and more in accord with athermal experiments.

An expression for $1 - f'$ is obtained by combining Eqs. (5.1) and (5.2) and integrating, which gives

$$1 - f' = \exp(KV_p(G_2 - G_1 - A)) \quad (5.3)$$

where A is the value of $G_2 - G_1$ at the onset of transformation. Magee demonstrated that Eq. (5.3) or some equivalent accurately fits almost all results from athermal martensitic rapid cooling studies.

The volume fraction f' is equal to ρ_0/ρ_2 times the mass fraction f . Since ρ_0/ρ_2 is nearly 1, Eq. (5.3) is expected to be valid for mass fraction data. In fact, by using similar assumptions, Eq. (5.3) can be derived with f' replaced by f .

The search for a physical model to reproduce Eq. (5.3) is certainly a major problem in the physics and metallurgy of martensitic transformations. The technological importance of these transformations in commercial materials enhances interest in understanding such phenomena.

5.3. Nucleation of a New Phase

Various types of nucleation sites are discussed. A new concept is described in which nucleation sites are "frozen-in" by a sudden step in pressure.

5.3.1. Nucleation Sites

Energy considerations have led to the widely-accepted belief that nucleation of the second phase occurs on defects such as: (1) impurities, (2) grain boundaries, and (3) dislocations. Calculations of energy to nucleate on various defects show that a dislocation is most important.⁵¹

If nucleation occurs on defects, it is reasonable to assume that not all the sites are activated by the same driving force. An increase in active nucleation sites with increasing driving force provides a plausible explanation of the observed mixture of phases for final states in athermal martensitic and certain shock experiments. A satisfactory theory of transformation would provide a physical mechanism or mechanisms for such an increase, but such has not yet appeared.

Twins have been suggested as nucleation sites, but no detailed energy calculations have been made. Since twins can be formed from interacting dislocations, one might assume that energy requirements for nucleation at a twin are of about the same magnitude as for dislocations; in that case, twin surfaces would be important.

In some materials, like iron and steel, twinning is the dominant mechanism for plastic yielding under rapid compression.⁵² In fact, the observed rapid increase in density of twins as the transformation stress in iron is approached has led German, et al.³⁰ to suggest twins as nucleation sites for the hcp phase.

Consideration of the bcc lattice shows that only a small change is required to obtain hcp structure along the

plane of the twin. A crystallographic model illustrating a twinned bcc lattice is shown in Fig. 5.5(a) with some irregular hexagons outlined. The lattice is viewed as stacked (110) planes. A small shear of the twin plane in the [111] direction results in a layer of symmetric hexagonal cells along the twin plane as shown in Fig. 5.5(b). A semicoherent interface exists between the two phases. The shear mechanism is similar to the one given in Fig. 5.3. It appears feasible that the nucleation of the hcp phase can occur on twins.

A possibility which has not been previously investigated is that equilibrium embryos of the second phase, which always exist as a result of statistical fluctuations, may be "frozen-in" by sudden application of sufficient pressure to bring the material into the stability field of the second phase. This type of nucleation would apply particularly in a shock wave. It is described in detail in the next section.

5.3.2. Nucleation Due to Rapid Application of Stress

Consider here only material in a lattice that is perfect except for thermal fluctuations. In an equilibrium state of the first phase there is a distribution of embryos of the second phase due to normal statistical fluctuations. Figure 5.6(a) shows the number of embryos in stable phase 1 as a function of the number of atoms, n , in each embryo. These embryos are created, grow, and shrink through fluctuations. For this case, where phase 1 is stable, energy to grow increases monotonically as shown by curve A in Fig. 5.6(b) where $G_{21} > 0$. If

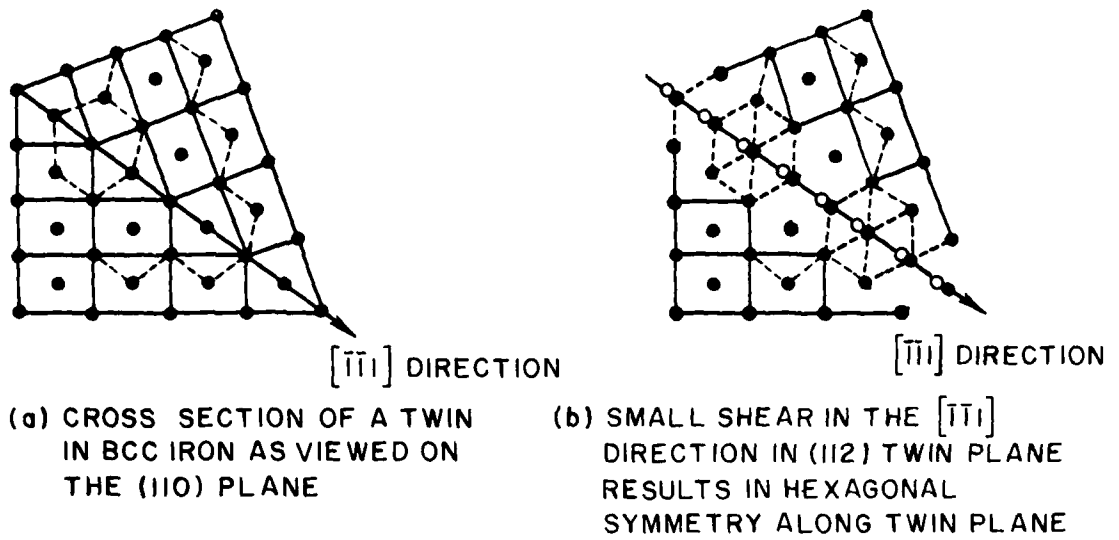


FIGURE 5.5 SHEAR MECHANISM IN BODY-CENTERED-CUBIC IRON TO OBTAIN HEXAGONAL SYMMETRY ALONG A TWIN PLANE.

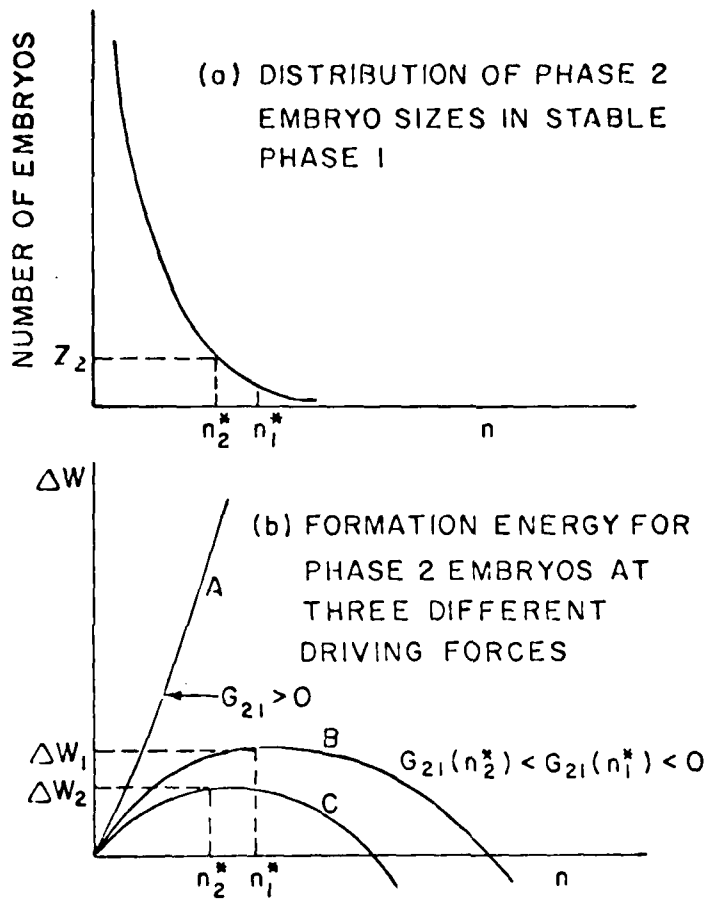


FIGURE 5.6 SPHERICAL EMBRYOS IN STABLE PHASE 1. CURVE A IS FOR THE STABLE PHASE 1 FIELD WITH $G_2 - G_1 = G_{21} > 0$. CURVE B IS FOR LOW PRESSURE SUFFICIENT TO MAKE THE PHASE 2 FIELD STABLE WITH $G_{21}(n_1^*) < 0$. CURVE C IS FOR HIGHER PRESSURE, P_2 , FOR WHICH $G_{21}(n_2^*) < G_{21}(n_1^*) < 0$.

sufficient stress, P_1 , is applied to make the field for phase 2 stable, G_{21} changes sign and curve B of Fig. 5.6(b) results. For this case, an embryo for which $n < n_1^*$ requires energy to grow; those with $n_1 > n_1^*$ will continue to grow because energy of the system is diminished by growth. Embryos of size $n > n^*$ are called nuclei.

Increasing stress to P_2 produces energy curve C in Fig. 5.6(b). In this case, the driving force $G_{21}(P_2)$ is more negative than $G_{21}(P_1)$, so energy required to form a stable nuclei of phase 2 is reduced from ΔW_1 to ΔW_2 . For curve C a stable nuclei of phase 2 contains n_2^* atoms: $n_2^* < n_1^*$.

If the distribution of embryo sizes given in Fig. 5.6(a) does not change when pressure is increased from zero to P_2 , then the number of embryos, N_2 , which become stable includes all nuclei for which $n > n_2^*$. This condition applies if the time required to apply the driving force is less than the time required to redistribute embryo sizes to conform to the new state. This should certainly be true for large embryos in a solid where reformation times are large when a shock wave passes.

A relationship between driving force and number of nucleation sites based on these concepts can be derived using nucleation theory. Assume the generally accepted conditions of nucleation, namely, that a number of small clusters of atoms, called embryos, exist; embryos are internally uniform and have the same structure and properties as the final phase in bulk form. These assumptions about embryos leave shape and size as the only variable parameters. A geometrical shape is adopted by

the embryo which minimizes the energy of the system for the formation of a nucleus. For simplicity, assume that n atoms in an embryo form a sphere. When the spherical embryo is formed, energy of the entire assembly increases by the amount ΔW defined by the expression⁵¹

$$\Delta W = n G_{21} + (36\pi V_2^2)^{1/3} \sigma n^{2/3} \quad (5.4)$$

where V_2 is volume per atom of the second phase and σ is surface energy per unit area of the interface between the two phases. The surface energy term in Eq. (5.4) makes it necessary for G_{21} to attain a certain negative value before transformation can begin.

Consider now the stability of embryos according to their size. Embryos containing n^* atoms maximize ΔW , where

$$n^* = \frac{-32\pi\sigma^3 V_2^2}{3G_{21}^3} \quad (5.5)$$

Having reached this size, they continue to grow.

In macroscopic assemblies, fluctuations will lead to local transitory phase transformations. These fluctuations are also responsible for establishing a distribution of embryos of different sizes within a stable phase which has the same atomic arrangement as the new phase. Frenkel⁵³ treated each embryo as a molecule of a particular kind, independent of the others, and randomly present as a dilute solution in phase 1. The thermodynamic Gibbs potential of such a solution is given by the expression

$$G = N_1 G_1 + \sum_n N_n \left(G_2 n + (36\pi V_2^2)^{1/3} \sigma n^{2/3} \right) + kT \left(N_1 \log \left(\frac{N_1}{N} \right) + \sum_n N_n \log \left(\frac{N_n}{N} \right) \right) \quad (5.6)$$

where N_n is the number of embryos containing n atoms and $N' = N_1 + \sum_n N_n$ denotes the total number of species, those of different size being treated as molecules of different kinds. Size distribution of clusters was determined by maximizing Eq. (5.6) to obtain the expression,

$$N_n = N \exp \left(-\frac{\Delta W(n)}{kT} \right), \quad (5.7)$$

where $N = \sum_n n N_n$ is total number of atoms per cm^3 , k is the gas constant, and T is temperature.

According to Frenkel,⁵³ the kinetics of transformation in solids does not differ, in principle, from kinetics of the condensation process considered above, except for certain special features connected with the shapes of crystals. Therefore, we assume that Eq. (5.7) is valid for solid systems.

If the distribution of embryos has insufficient time to change from its initial form when a large stress is rapidly applied, a certain number of embryos are suddenly found to exceed the critical or stable size for the new, thermodynamic state, becoming "trapped" on the side of the energy curve favoring growth. The number of embryos that begin to grow under these conditions can be calculated from the distribution function of stable embryos for old and new states. The number of embryos N_{12} in the interval (n_1, n_2) is given by the expression,

$$N_{12} = \sum_{n_1}^{n_2} N_n \Delta n \approx \int_{n_1}^{n_2} N_n dn, \quad (5.8)$$

where N_n is a large number and Δn is equal to 1.

Substitution of Eq. (5.7) into Eq. (5.8) and integration over the interval (n^*, n^∞) gives the number of clusters N^* that exceed the critical size for a sudden change in driving force:

$$N^* = N \int_{n^*}^{n^\infty} \exp \left[- \frac{\Delta W^O(n)}{kT_0} \right] dn, \quad (5.9)$$

where $\Delta W^O(n)$ is given by Eq. (5.4) for the initial stable state ahead of the shock front, and n^* is given by Eq. (5.5) for the state behind the shock front. We are not able to integrate Eq. (5.9) analytically. However, we can differentiate Eq. (5.9) with respect to G_{21} using Leibnitz's rule,⁵⁴ which results in the expression,

$$\begin{aligned} \frac{dN^*}{dG_{21}} &= N \exp \left[- \frac{\Delta W^O(n^\infty)}{kT_0} \right] \frac{dn^\infty}{dG_{21}} \\ &- N \exp \left[- \frac{\Delta W^O(n^*)}{kT_0} \right] \frac{dn^*}{dG_{21}} \\ &+ N \int_{n^*}^{n^\infty} \frac{\partial}{\partial G_{21}} \exp \left[- \frac{\Delta W^O(n)}{kT_0} \right] dn. \end{aligned} \quad (5.10)$$

Since the integrand and n^∞ are independent of G_{21} ,

$$\frac{dN^*}{dG_{21}} = -N \exp \left[- \frac{\Delta W^O(n^*)}{kT_0} \right] \frac{dn^*}{dG_{21}}. \quad (5.11)$$

Differentiating Eq. (5.5) with respect to G_{21} results in the expression,

$$\frac{dn^*}{dG_{21}} = -n^* \left[\frac{3}{G_{21}} - \frac{2}{V_2} \frac{dV_2}{dG_{21}} \right]. \quad (5.12)$$

Substituting Eq. (5.12) into Eq. (5.11) results in the expression,

$$\frac{dN^*}{dG_{21}} = Nn^* \left[\frac{3}{G_{21}} - \frac{2}{V_2} \frac{dV_2}{dG_{21}} \right] \exp \left[- \frac{\Delta W^0(n^*)}{kT} \right]. \quad (5.13)$$

Eliminating n^* and $\Delta W^0(n^*)$ by Eqs. (5.4) and (5.5) results in the final expression,

$$\frac{dN^*}{dG_{21}} = \frac{-32\pi\sigma^3 V_2^2 N}{3G_{21}^3} \left[\frac{3}{G_{21}} - \frac{2}{V_2} \frac{dV_2}{dG_{21}} \right] \times \exp \left[\frac{-16\pi\sigma^3 V_2^2}{G_{21}^2} \left[1 - \frac{2G_{21}(P=0, T=295^\circ K)}{3G_{21}} \right] \right], \quad (5.14)$$

which depends on σ , V_2 , N , dV_2/dG_{21} , and G_{21} . This equation is significant because it establishes a relation between number of nucleation sites and driving force, G_{21} , in the stable field of phase 2.

To calculate values of dN^*/dG_{21} , from Eq. (5.14) requires values for surface energy σ , volume V_2 , N , driving force G_{21} , and dV_2/dG_{21} . Values for σ found in the literature vary from 20 ergs/cm² for a coherent twin interface to 200 ergs/cm² for an incoherent interface.^{51,55} Examination of Eq. (5.14) reveals that the influence of the exponential function is overriding and if any nucleation is to occur, the argument of

the exponential must be less than about 100. This implies that the value for σ must not exceed about 20 ergs/cm². Values of the right hand side of Eq. (5.14) were therefore calculated for $\sigma = 20$ ergs/cm². Values for the driving force G_{21} , which are given in multiples of A, were obtained from the two-phase equation of state for iron given in Appendix A. The value for $A = -8.33 \times 10^{-15}$ ergs/atoms is G_{21} at $p^{TL} = 130$ kbar, $T = 338^\circ\text{K}$, which is the state for onset of transformation for the loading process. The value for $G_{21}(P=0, T=295^\circ\text{K}) = 6.85 \times 10^{-14}$ ergs/atoms, which defines the initial distribution function shown in Fig. 5.5(a), was obtained using the approximation $G_{21} \approx (V_2 - V_1)(P - P^T) - (S_2 - S_1)(T - 332^\circ\text{K})$. (See Appendix A.) A constant value $V_2 = 1.045 \times 10^{-23}$ cm³/atoms for iron at $p^{TL} = 130$ kbar, $T = 338^\circ\text{K}$ was used since V_2 varies only from 1.045×10^{-23} cm³/atoms to 1.021×10^{-23} cm³/atoms over the stress range 130 kbar to 200 kbar. The number of iron atoms, N, in 1 cc is 8.48×10^{22} . The value for $(2/V_2)(dV_2/dG_{21}) \approx 2K_T/(V_2 - V_1) \approx -150$ gm/Mbar cm³, where K_T is isothermal compressibility of phase 2 and the approximation $dG_{21} \approx \Delta V dP$ was used. (See Appendix A.) Since $3/A = 3.4 \times 10^4$ gm/Mbar cm³, $(2/V_2)(dV_2/dG_{21})$ can be ignored.

Inspection of values given in the last column of Table 5.2 reveals that as the magnitude of G_{21} increases so does the magnitude of dN^*/dG_{21} . Since dN^*/dG_{21} for $G_{21} = A$ is so small compared to values at higher driving force, nucleation is initiated for values at a driving force between A and 2A. A smaller value for σ would force the initiation of

nucleation nearer A, but the adjustment appears unwarranted considering uncertainties in σ . Values of n^* become unphysically small for driving forces exceeding $2A$. The value of this model and suggested ways to improve it are discussed in the next section.

If because of cold work, grain growth, or other energy concentrating processes, a number of permanent spherical embryos of phase 2 exist in the stable field of phase 1, then the energy required to reach critical size is less than for pure homogeneous nucleation. In fact, suppose that these pre-existing sites are of size n_0 and that normal statistical fluctuations created a distribution of sizes as in the homogeneous case; then Eqs. (5.4) and (5.5) are unchanged, except that $n + n_0$ is substituted for n . The important change comes in that N becomes the number of pre-existing sites N_0 of size n_0 . Substitution of N_0 for N in Eq. (5.14) results in an expression for dN^*/dG_{21} for the case of pre-existing sites.

5.4. The Quasistatic Hugoniot

Shock data described in Section 5.1 show that:

1. Initial transformation rate for close-in experiments exceeds $2 \times 10^7/\text{sec}$ for mass fraction of phase 2.
2. Any transformation taking place behind the plastic II shock is slow since there is no evidence of changes in stress behind the shock front.
3. Hugoniot P-V states for 130 to 200 kbar are vastly different from those predicted by equilibrium hydrostatic thermodynamics and measured values of dP/dT .

TABLE 5.2.--Values of $\frac{dN^*}{dG_{21}}$

G_{21} (ergs/ atom)	P (Mbar)	n^*	$\frac{\Delta W(n^*)}{kT_0}$ ^b	$\exp \left[-\frac{\Delta W(n^*)}{kT_0} \right]$	$\frac{dN^*}{dG_{21}}$ number atom ergs cm ³	$\frac{dN^*}{dG_{21}}$ number gm Mbar cm ⁶
A	0.13	51.1	99.8	4.5×10^{-44}	-8.3×10^{-5}	-7.7×10^{-15}
2A	0.144	6.4	14.4	5.6×10^{-7}	-1.3×10^{32}	-1.2×10^{22}
3A	0.158	1.9	4.84	7.9×10^{-3}	-5.4×10^{35}	-5.0×10^{25}
4A	0.172	0.8	2.28	1.0×10^{-1}	-2.9×10^{36}	-2.6×10^{26}

^a $A = G_{21}$ (P=.13 Mbar, T=338°K) = -8.33×10^{-15} ergs/atom = -7.06
x 10⁸ ergs/cm³

^b $\Delta W(n^*) = (6.85 \times 10^{-14}$ ergs/atom) $n^* + (4.62 \times 10^{-14}$ ergs/atom) $n^{*2/3}$

Discussion of points 1 and 2 is deferred to Chapter 6. Concern here is with point 3 and the quasistatic Hugoniot data in the mixed phase region shown in Fig. 4.7.

It can be seen from Fig. 4.7 that changes in V are nearly linearly related to changes in pressure for P between 130 and 200 kbar. If these measured points deviate from equilibrium because transformation stops before completion, then the mass fraction, $f(P,T)$, can be calculated for each point on the Hugoniot above the transition point according to the lever rule,

$$1 - f = \frac{V_2(P,T) - V(P,T)}{V_2(P,T) - V_1(P,T)}, \quad (5.15)$$

where f is the mass fraction of phase 2, $V(P,T)$ is specific volume of the mixture, and $V_1(P,T)$ and $V_2(P,T)$ are specific volumes of phases 1 and 2, respectively. As V approaches V_2 in value, small systematic uncertainties in $V_2 - V_1$, V_2 , and V lead to large uncertainties in $1 - f$:

$$\frac{\delta(1-f)}{1-f} = \frac{\delta V_2}{V_2 - V} - \frac{\delta V}{V_2 - V} - \frac{\delta(V_2 - V_1)}{V_2 - V_1}. \quad (5.16)$$

Values of f calculated from Eq. (5.15) and the measured Hugoniot points shown in Fig. 4.7 are represented in Fig. 5.7, where $\ln(0.93-f)$ is plotted versus $P - P^{TL}$. This odd ordinate was chosen because it was found that subtracting 0.07 from $1 - f$ produced a reasonable fit of the data to a straight line, as shown. This deviation of $1 - f$ from zero at the asymptote may be due to error in estimating the position of the

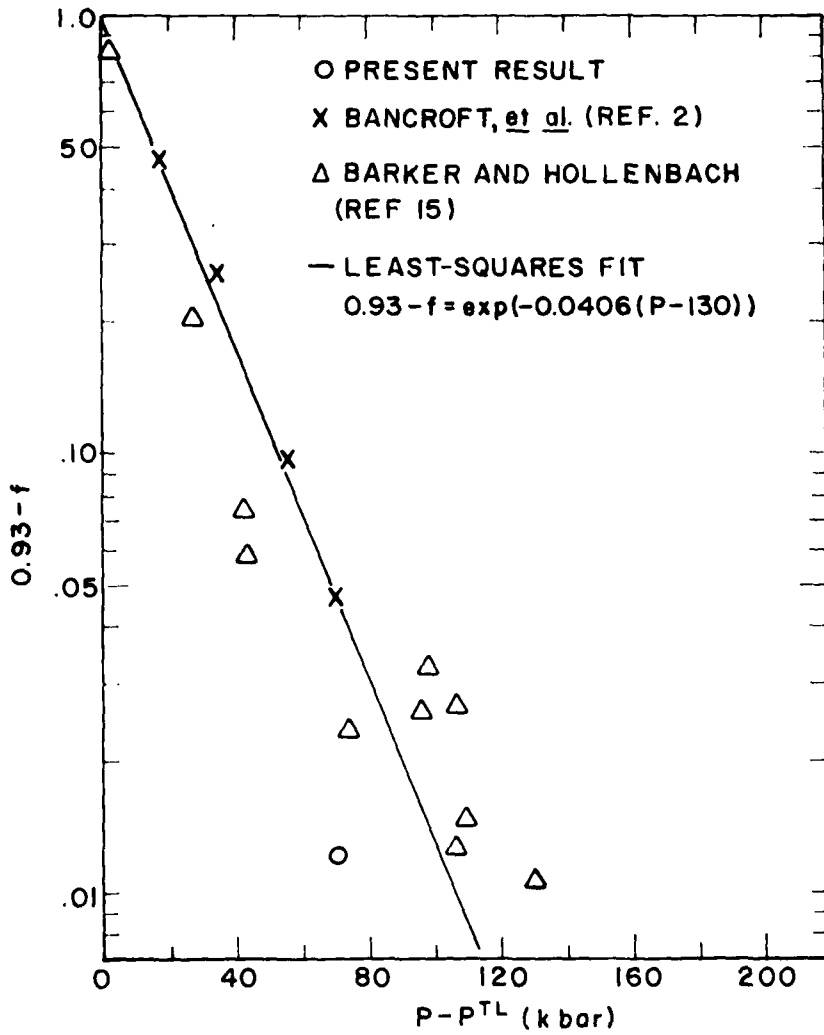


FIGURE 5.7 AMOUNT OF EPSILON PHASE AS A FUNCTION OF STRESS IN EXCESS OF 130 kbar.

phase 2 boundary or to incomplete transformation for large values of $P - P^{TL}$. The data shown are insufficient to distinguish between these two possibilities, each of which is represented in Eq. (5.16). The third term on the right hand side of that equation is negligible.

The second phase surface is calculated from a two-phase equation of state which is based on data of Mao, et al.³³ (See Appendix A.) They report an uncertainty in initial volume for the second phase, V_{02} , of $.0011 \text{ cm}^3/\text{gm}$. This uncertainty was reduced approximately 50 percent using a value of V_{02} consistent with x-ray measurements of $V_2 - V_1$ made at stresses near 130 kbar and reported by Mao, et al.³³ The difference, $V_2 - V$, obtained from this equation of state and measurements by Barker and Hollenbach¹⁵ goes from 0.00056 to $0.0004 \text{ cm}^3/\text{gm}$ for stresses from 204 to 304 kbar, which suggests that the second phase surface and the Barker and Hollenbach data agree within uncertainties of the experiments and accuracy of the equation of state for the second phase.

Since $P - P^{TL}$ is nearly proportional to G_{21} for iron (see Appendix A), an equally good fit is obtained by plotting $\ln(.93-f)$ versus G_{21} . The equation of the line so obtained is

$$0.93 - f = \exp[\theta(G_{21} - A)] \quad , \quad (5.17)$$

where $\theta = 6,444 \text{ gm/Mbar cm}^3$ is determined by least squares, and $A = 8.7 \times 10^{-5} \text{ Mbar cm}^3/\text{gm}$ is G_{21} at the transformation state (P^{TL}, T^{TL}) . The differential of Eq. (5.17) is

$$df = -\theta(.93-f) d(G_{21}), \quad (5.18)$$

which corresponds closely with the relation found by Magee⁴⁷ to describe athermal results for the gamma to alpha transformation, Eq. (5.3). Although there is no obvious connection, Magee found, for carbon alloys with less than 1.2 percent carbon, a value for θ which is 14 times larger than θ from Fig. 5.7.

Due to the large uncertainties in $1 - f$ for large values of P shown in Fig. 5.7, one might consider data only for stresses less than or equal to 204 kbar. These data are well fitted by a linear relation between $\ln(1-f)$ and G_{21} . They yield a value of θ equal to 4,048 gm/Mbar cm^3 , less than two-thirds the previous value.

Equation (5.17) can be interpreted in the following way: G_{21} is driving force which causes the transformation to proceed. It must exceed a threshold value, A , before the transformation is initiated. For unknown reasons the transformation proceeds only as G_{21} is increased. If, for example, nucleation sites exist which are activated at different stress levels, increases in P produce increases in G_{21} , more nucleation sites are activated, and the transformation proceeds incrementally. The calculation of nucleation sites described in Section 5.3 provides a detailed model of such a situation, Eq. (5.14). In that case, however, the proportionality parameter θ is not constant but varies over a wide range of values in the mixed phase region. If this transformation is martensitic and transformation occurs with constant average plate volume, V_p , of 10^{-8} cm^3 , then

values of θ are obtained by multiplying V_p by entries in the last column of Table 5.2. This gives $\theta \approx 7 \times 10^{-23}/\text{Mbar cm}^3$ for $G_{21} = A$ and $\theta = 1.2 \times 10^{14} \text{ gm/Mbar cm}^3$ for $G_{21} = 2A$. These values are far from observed values, which is not surprising considering the unreality of the basic assumption that nucleation is occurring in the homogeneous lattice.

Values for θ calculated from Eq. (5.14) come much closer to the measured value when the homogeneous model is modified by assuming spherical pre-existing embryos of phase 2. For this case, if martensitic plate volume $V_p = 10^{-8} \text{ cm}^3$ is 1 percent of the grain volume for 0.1-mm-diameter grains, N_0 can be calculated by dividing values of dN^*/dG_{21} in the last column of Table 5.2 into $-N/V_p \theta = 6.4 \times 10^{34}$. This gives $N_0 = 8.3 \times 10^{48}/\text{cm}^3$ for $G_{21} = A$, $N_0 = 5.3 \times 10^{12}/\text{cm}^3$ for $G_{21} = 2A$, and $N_0 = 1.28 \times 10^9/\text{cm}^3$ for $G_{21} = 3A$. These values for N_0 approach seemingly realistic values for pre-existing sites since the number of twins required to account for all the plastic strain in shocked iron at 130 kbar was inferred from Johnson and Rhode⁵⁶ to be about $10^7/\text{cm}^3$.

The above calculations show how a relation between dN and dG_{21} can be established, and although a detailed model to explain the form of Eq. (5.17) has not been produced, its similarity to the Magee equation strengthens the link between the alpha to epsilon, shock-induced transformation and the athermal, martensitic, gamma to alpha transformations in iron. The calculation also suggests a basis for understanding of both athermal gamma to alpha and shock-induced alpha to epsilon transformations.

The basic concept of freezing-in statistical fluctuations appears sound and avoids the theoretical problems of nucleation, wherein growth of embryos is too slow to enable the transformation to proceed as observed. Since the weight of observations on athermal martensite suggests that nucleation occurs at lattice imperfections, this calculation should be repeated for the much more difficult problems of embryos formed about such sites. The simple modification to homogeneous nucleation described above suggests that such calculations will be in the right direction to bring about agreement between measurements and theory. Considerations are also required on the effects on the transformation of (1) strain in the lattice to accommodate the nuclei, (2) use of the hydrostatic Gibbs function in problems dealing with solids, and (3) use of bulk values of surface energy on small surfaces with large curvature. If these modifications can be accomplished, it may well turn out that the too rapid variation of dN/dG_{21} with G_{21} , shown in Table 5.2, vanishes and that a reasonable theoretical basis for the observations is produced.

CHAPTER 6

KINETICS OF TRANSFORMATION

Horie and Duvall²⁰ treated wave propagation in a phase-transforming material by assuming that:

1. Phases do not separate mechanically; i.e., particle velocity is common to both phases.
2. Pressure and temperature are common to both phases.
3. Interfacial energy is a small fraction of the total energy.
4. Mass transfer is irreversible and df/dt is a known function of the state variables.

These assumptions can be incorporated in the flow equations to provide a theoretical basis for calculating evolution of a shock wave in the transforming material, including the effects of transformation kinetics. Their principal result can be expressed in the form:

$$\frac{d\bar{P}}{dt} = a_{11} \frac{d\rho}{dt} + a_{12} \frac{df}{dt} , \quad (6.1)$$

$$\frac{dT}{dt} = a_{21} \frac{d\rho}{dt} + a_{22} \frac{df}{dt} , \quad (6.2)$$

$$\frac{df}{dt} = \Psi(G_{21}, f) , \quad (6.3)$$

where a_{11} is frozen sound speed at mass fraction f ; the other a_{ij} are functions of V, T, P, f . They assumed for calculational purposes a simple relaxation function for $\Psi(G_{21}, f)$:

$$\Psi = (f^{\text{eq}} - f) / \tau_1, \quad (6.4)$$

where τ_1 is a relaxation time.

Andrews^{27,29} modified Ψ to a form more obviously related to the Gibbs function:

$$\frac{df}{dt} = \Psi = \frac{-JG_{21}}{|A|\tau_2}, \quad 0 \leq f^{\text{eq}} \leq 1, \quad (6.5)$$

where J is the Jacobian, $J = \partial(V, E) / \partial(P, T)_f = -C_{pf} V K_{Sf}$, and $|A|$ is the matrix of coefficients of differential equations describing the mixed phase region. (See Appendix D.)

Relaxation time, τ , is not uniquely defined and must be associated with a specific model for f^{eq} . Horie and Duvall²⁰ assumed f^{eq} to be defined by states on the equilibrium PVT surface in the mixed phase region at the same volume and temperature as the considered state. Figure 6.1 shows a cross section of the PVT surface at a constant T and two possible transient states of the transforming mixture, A and B. State A projects to a volume V_A on the isotherm, giving

$$-f^{\text{eq}} = \frac{V_1^T - V_A}{V_2^T - V_1^T} \quad (6.6)$$

which is a function of pressure and temperature. State B is a more completely transformed state at the same temperature. For this case $V_B < V_2^T$ and $f^{\text{eq}} = 1$.

Andrews assumed f^{eq} to be defined by states on the equilibrium PVE surface for the same volume and energy as the

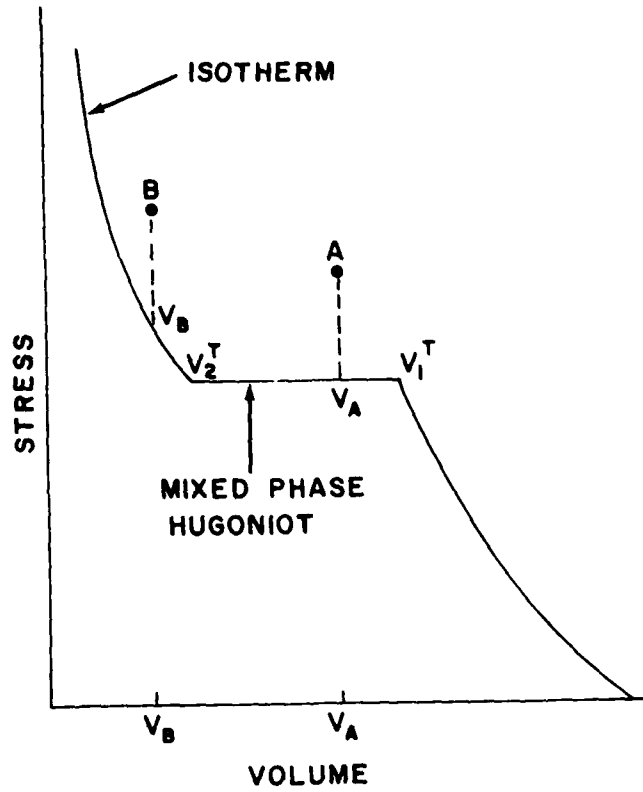


FIGURE 6.1 ISOTHERM USED TO DEFINE $f^{eq} = (V_A - V_1^T) / (V_1^T - V_2^T)$ FOR STATE A WHERE $0 \leq f^{eq} \leq 1$ AND $f^{eq} = 1$ FOR STATE B WHERE $V_B \leq V_2^T$

considered state. Under conditions of constant V and E , increments in f are proportional to increments in G_{21} and it follows that^{27,29}

$$f - f^{eq} = \frac{JG_{21}}{|A|}, \quad 0 \leq f^{eq} \leq 1. \quad (6.7)$$

6.1. Relaxation Times

There are three types of existing experimental data which measure different aspects of shock evolution in iron and allow evaluation of relaxation time: (1) amplitude of stress behind the plastic I shock as a function of sample thickness, (2) rise time of the plastic II shock, and (3) residual metallurgical effects when the plastic II shock is rapidly diminished by relief waves. Values of and bounds for τ for these different types of data are discussed separately in the next three subsections and are shown to agree within about 50 percent.

6.1.1. Decay of Stress Associated with the Plastic I Shock

The plastic I shock decays in amplitude as it propagates. If material strength is ignored, plastic I amplitude is expected to be near final driving amplitude at positions near the impact boundary. By making the essential assumption that phase 1 material is shocked to final driving stress, P^D , at the impact surface and that the plastic I shock velocity is constant, Eqs. (6.1) and (6.4) can be used to derive an approximate differential equation for rate of decay of the plastic I shock amplitude:

$$\frac{dP}{dt} \approx \frac{a_{11}^2 \Delta V}{2V_1^2} \frac{df}{dt}, \quad (6.8)$$

where $\Delta V = V_2 - V_1$.

Setting $f = 0$ in Eq. (6.4) and assuming constant temperature and linear P-V relations for phase 1 and phase 2 near the mixed phase boundaries, they obtained the relation,

$$P = P^{TL} + (P^D - P^{TL}) \exp\left[-\frac{x}{2U_2\tau_1}\right], \quad 0 \leq f^{eq} \leq 1, \quad (6.9)$$

where P^{TL} is transition stress, P^D is driving stress, x is sample thickness, and U_2 is constant plastic I shock velocity. Equation (6.9) was found compatible with data in Fig. 4.3, assuming $\tau_1 = 0.05 \mu\text{sec}$ to be constant for $0 \leq x \leq 1 \text{ mm}$ and a final driving stress of 201 kbar. This value represents an approximate upper bound for τ_1 since a 20 percent increase in its value is incompatible with the data, while effects of a decrease are undetectable.

Barker and Hollenbach¹⁵ found that $\tau_1 = 0.17 \mu\text{sec}$ was required in Eq. (6.9) to explain their data on plastic I stress decay for equal propagation distances but different final driving stresses.

Substituting Eq. (6.5) into Eq. (6.8) results in

$$P = P^{TL} + (P^D - P^{TL}) \exp\left[-\frac{a_{11}^2 \Delta V^2 J x}{2V_1^2 |A| U_2 \tau_2}\right], \quad 0 \leq f^{eq} \leq 1, \quad (6.10)$$

which describes plastic I decay according to Andrews' model.^{27,29} For iron, the term $-C_p \Delta V^2$ in $|A|$ (see Appendix D) exceeds the

others by an order of magnitude. This gives $J/|A| \approx V_1 K_S / (\Delta V)^2 = v_1^2 / (a_{11}^2 \Delta V^2)$ which makes Eq. (6.10) identical to Eq. (6.9). This shows that, under the assumptions used to obtain Eq. (6.9), $\tau_1 = \tau_2$ for iron. This identity is not a general result, and in transformations where terms other than $-C_p \Delta V^2$ dominate, the value of $|A|$ will produce different values for τ_1 and τ_2 .

Equations (6.9) and (6.10) are strongly dependent on the basic assumption that the shocked phase 1 material remains in phase 1 and, at the impact surface, reaches the driving stress at a point on the metastable or extended phase 1 surface. This assumption may be invalidated by the inability to prepare smooth microscopic surfaces. Even the best finely-lapped and polished surfaces contain microvoids which require closing before stress at the impact surface can be sustained. If the effective driving stress were to be thus reduced, τ_2 in the above equation could be increased without violating the data.

Data of Fig. 4.3 show plastic I first decreasing as x increases, then increasing, then decreasing again. This behavior might arise from inaccuracies in measurements which have not been fully accounted for, or from other effects such as shear strength associated with precursor decay or relaxation in the plastic I wave and behind it.

6.1.2. Rise Time of Plastic II Shocks

Rise times of 0.2-0.3 μsec for plastic II shocks have been reported elsewhere;²³ these are consistent with the present

measurements, which gives a value of 0.18 ± 0.02 μsec for the rise time. These rise times are used here to evaluate relaxation times from calculated steady shock wave profiles.

Swan, et al.⁵⁷ have shown that transient effects in shock fronts ultimately decay, leaving a steady shock profile. If it is assumed that measured profiles of the plastic II shock front are steady, and that the locus of states within these shocks lies along the appropriate Rayleigh line, it follows that an estimate of relaxation time can be obtained by comparing measured profiles with calculated steady profiles, assuming that transformation kinetics dominates the shock transition process. Techniques for calculating profiles are described elsewhere.^{57,58} The technique used here is described in Appendix D. Values of relaxation time inferred in this way should be greater than true values because effects of viscosity act to increase rise time.

Figure 6.2 shows calculated temperature-independent profiles for $\tau_1 = 0.05$ μsec and $\tau_1 = 0.1$ μsec . The relaxation time, $\tau_1 = 0.05$ μsec , in the rate equation of Eq. (6.4) was required to obtain a wave profile with rise time near 0.2 μsec . Width of the shock wave as used here is defined as rise time times laboratory velocity, $U_2 - u_1 = 3.36$ $\text{mm}/\mu\text{sec}$. A practical definition of 5 percent to 95 percent of maximum stress amplitude was used for rise time and shock width determinations.

6.1.3. Metallurgical Data

Residual hardness for iron which has been shocked into the epsilon phase by successive plastic I and plastic II waves

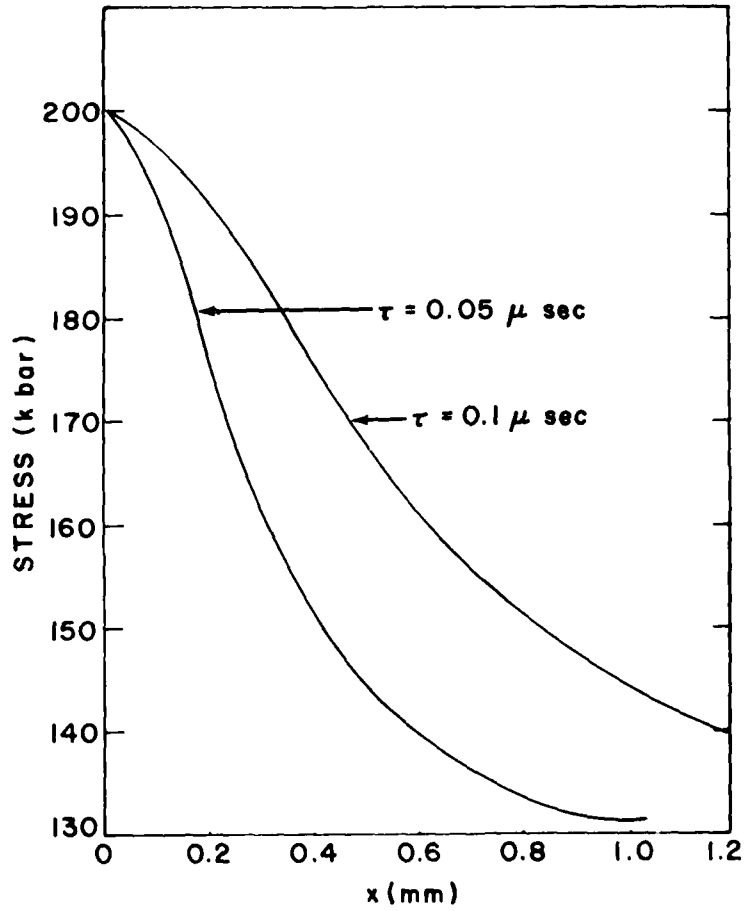


FIGURE 6.2 TEMPERATURE-INDEPENDENT STEADY PLASTIC II SHOCK FRONTS USING EQ. (6.4) AND $U_2 - u_1 = 3.36 \text{ mm}/\mu \text{ sec}$.

is several times greater than for that which has not been transformed. Thickness of the plastic II shock front has been estimated by some workers from post shock hardness measurements in which the plastic II wave is quenched by reflection of elastic precursor and plastic I wave from a free surface.^{24,25}

Shock width can be related to the hardness transition zone thickness measured in such experiments in the following way: Assume the interaction between the oncoming plastic II wave and reflected plastic I wave to be as shown in Fig. 6.3.

Then

$$\frac{h_2-h_3}{U_2'} = (h_1-h_2)(1/R_2' - 1/R_1') + (h_2-h_5)(1/U_2' + 1/R_2') , \quad (6.11)$$

where velocities are Lagrangian, h_2-h_3 is shock width, h_1-h_2 is distance from the free surface, h_2-h_5 is width of the transition band, U_2' is plastic II wave velocity, R_2' is velocity associated with the relief wave that brings the stress behind the plastic II shock to 130 kbar, and R_1' is the leading elastic relief wave velocity. In deriving this expression the following assumptions were made: (1) wave velocities are constant through the region of wave interactions; (2) the plastic II shock is steady and can be represented as two parallel lines in the $h-t$ diagram; and (3) the first term on the right hand side of Eq. (6.11) is smaller than the second term. Slopes of the various lines are indicated in the $h-t$ diagram as the reciprocal of their wave speeds.

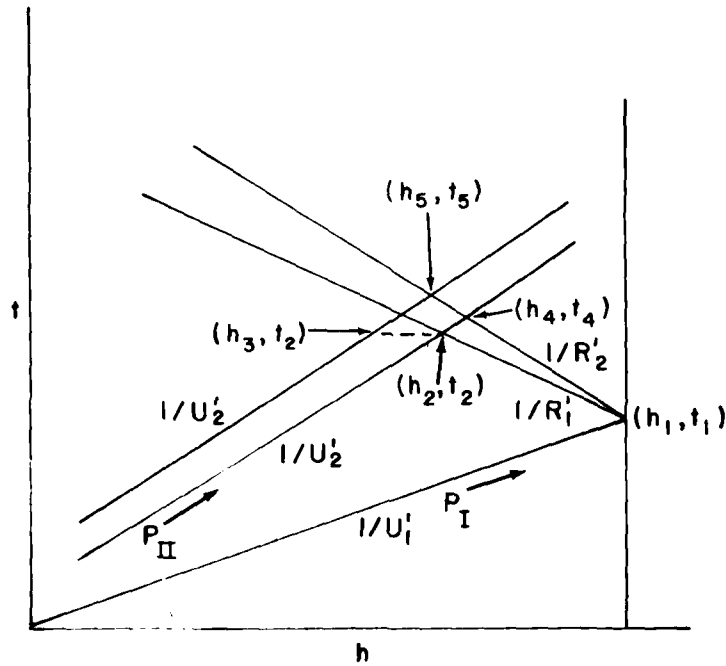


FIGURE 6.3 REFLECTED PLASTIC I WAVE REDUCES THE STRESS IN AND BEHIND THE PLASTIC II SHOCK FRONT TO A VALUE BELOW THE TRANSFORMATION STRESS. THIS PROCESS LEAVES A ZONE, h_5-h_3 , IN IRON OF VARYING HARDNESS.

Average values of $h_1-h_2 = 2.53$ mm and $h_2-h_5 = 0.47$ mm were found for a 190-kbar shock in 12-mm-thick samples of iron.²⁵ If $U_2' = 3.578$ mm/ μ sec, $R_2' = 5.69$ mm/ μ sec, and $R_1' = 6.58$ mm/ μ sec, then $h_2-h_3 = .98$ mm which is equivalent to a rise time of 0.27 μ sec for the plastic II wave front. This value is within the range of observed values of rise time described in the preceding section, but near the high side.

6.2. Slow Decay of the Stress Behind the Plastic I Shock

It was noted in Chapter 4 that p^{TL} diminishes slowly with propagation distance; but that if stress jump across the plastic I front is considered, this slow decay disappears. Therefore, one can reasonably infer that the slow decay of p^{TL} is due to precursor decay. The situation can be complicated by wave interactions so the inference is not conclusive.

The situation can be clarified by describing possible bounds of stress-particle velocity states at the impact boundary when an iron sample is impacted by an aluminum projectile. Figure 6.4 illustrates the pressure-particle velocity plane; dashed lines represent metastable extensions of lower pressure states and the solid lines represent equilibrium Hugoniot. The aluminum cross curve represents possible states at the impact boundary. Point A represents the maximum attainable stress at the instant of impact, and C represents the equilibrium stress obtained when all time effects have disappeared. The problem of kinetics at the impact surface is to describe how fast the stress gets from A to C. The time required for stress to decay from

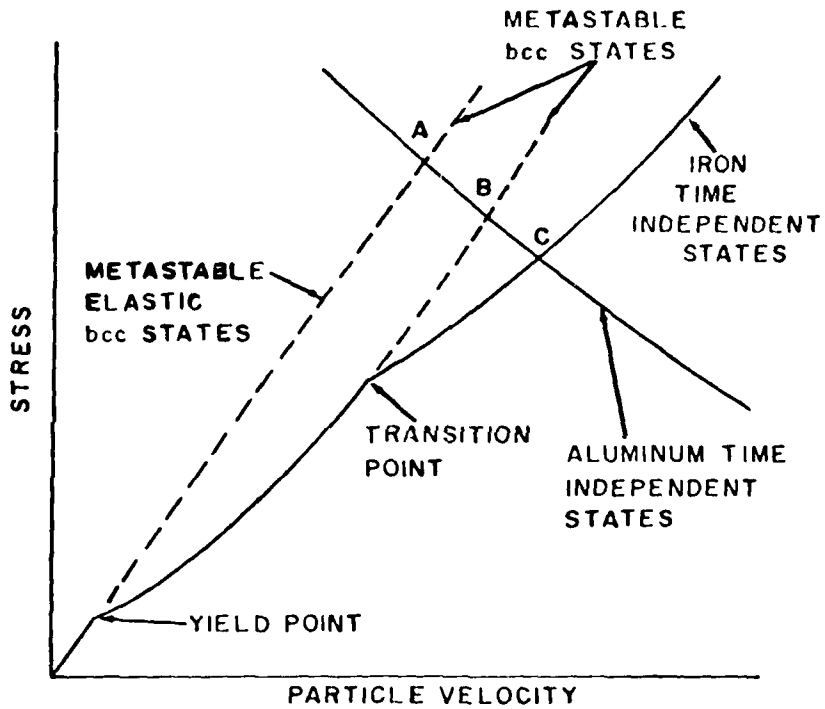


FIGURE 6.4 STRESS-PARTICLE VELOCITY STATES AT THE IMPACT BOUNDARY WHEN AN IRON SAMPLE IS IMPACTED BY AN ALUMINUM PLATE.

A to B depends on the elastic-plastic transformation rate, while the time for stress to decay from B to C depends on the polymorphic transformation rate. To understand the rate of decay from A to C requires an understanding of both transformation processes. However, if the yielding rate is much faster than the polymorphic transformation rate, the polymorphic transformation rate is the limiting and important one. In that case, details of the yielding process are not necessary to solve most problems of interest.

Both precursor and plastic I decay data show that both transformations occur very rapidly. However, the data of Chapter 4 are not sufficient to resolve effects of the kinetics of yielding on the evolution of shocks in iron. Further, experimental and theoretical work in this area are required.

6.3. Discussion

There are some disparities in relaxation times inferred from various types of data which suggest that relaxation time is not constant. However, the relaxation times are all of the order of 0.1 μ sec. A lower bound of initial transformation rate in iron shocked to 200 kbar of 10^7 /sec can be inferred from this value of τ and Eq. (6.4).

The theoretical treatment appears adequate for data being obtained. Future work may require closer examination of its basic assumptions.

CHAPTER 7

SUMMARY AND CONCLUSIONS

Little is known about atomic mechanisms which cause ultrafast phase transitions. This void in knowledge is partly due to lack of experimental data. Need for data and understanding of the transformation process is the reason for this study. Iron was chosen as the material to study primarily because of the wealth of existing thermodynamic and equation of state data.

Experimental intent of this study was to measure evolution of the plastic I shock in polycrystalline Armco iron when final driving stress is near 200 kbar. The most significant experimental result is that little or no variation of plastic I wave amplitude occurs for propagation distances between 0.9 and 6.35 mm. This implies a relaxation time of about 0.05 μsec or less for initial stages of the alpha to epsilon transformation. When the single measurement at 25.4-mm propagation distance is included with close-in data, one infers a slow variation of transformation stress with distance superimposed on the rapid decay for propagation distance of less than 1 mm. Inference of initial decay rate depends on the assumption that initial compression at the impact surface is entirely in the alpha phase.

Further results, which are essentially corroborative, are that:

1. Elastic precursor amplitude increases as sample thickness is decreased.
2. Transformation stress measured in a 25.4-mm-thick sample is 131.4 ± 3.3 kbar.
3. Relative volume behind the plastic II wave is $V_3/V_0 = 0.871 \pm .008$ for a stress of 201 ± 8.4 kbar.
4. Rise time in the plastic II shock front is $0.18 \pm .02$ μ sec.

These results are in essential agreement with those of earlier experiments reported in References 36, 2, 2, and 23, respectively.

In addition to this study other data exist which relate to kinetics of transformation. They are:

1. Rise times of 0.2-0.3 μ sec for the plastic II shock measured by Novikov, et al.²³ and more recently by Barker¹⁵ and this author.
2. Metallurgical measurements of a hardness transformation zone thickness in shocked iron by Smith²⁴ and more recently by Smith and Fowler.²⁵
3. Slow decay of the plastic I shock in iron first observed by Minshall²² and confirmed by this work.

Considering all but the slow decay of plastic I stress, the inferred relaxation time from the data was approximately equal to $0.1 \pm .05$ μ sec. This gives a lower bound for the initial transformation rate of 10^7 /sec for the second phase.

The slow decay in the plastic I shock amplitude may be due to decay in the elastic precursor amplitude for iron samples thicker than 1 mm. This is suggested by the apparently constant stress jump in the plastic I shock. Because of effects of wave interactions, this conclusion is not firm; experiments with samples treated to modify precursor structure may improve understanding of this phenomenon.

Based on the assumption that Hugoniot data between 130 and 250 kbar are for partially transformed material, the lever rule was used to calculate the mass fraction, f , of phase 2 which is experimentally related to excess stress above the transformation stress. These data show that f varies exponentially with G_{21} , the difference between Gibbs energies of the bulk phases, giving the expression

$$1 - f = \exp(\theta(G_{21} - A)) \quad ,$$

where θ is constant and A is the value of G_{21} at onset of transformation.

Previous workers have shown that such a relationship describes athermal martensitic transformations; this similarity strengthens the link between martensitic transformation and the shock-induced alpha to epsilon transformation. A possibility which has not been previously investigated is that equilibrium embryos of the second phase, which always exist as a result of statistical fluctuations, may be "frozen-in" by sudden application of sufficient pressure to bring the material into the stability field of the second phase. A relation between number of "frozen-in" nucleation sites and driving force can be established; this fact suggests a basis for understanding both athermal transformations and the shock-induced alpha to epsilon transformation.

Better theoretical calculations on "frozen-in" nucleation sites are needed which include strain effects and surface energy of small clusters of atoms; errors which result from use of the hydrostatic Gibbs energy for solids need to be evaluated.

Experiments to date have not revealed the operating mechanism for the ultrafast transformation in shocked solids. If the alpha to epsilon transformation is martensitic as suggested, then experiments with different grain sizes should give different kinetic results at close-in distances. Single crystal studies would be useful since it may be a shear-induced transformation with preferred directions and planes. If the transformation is nucleated on twins, cold rolling to eliminate twin formation prior to shock loading might change the kinetics of transformation. Double shock experiments in which first shock amplitude is varied in order to vary the shock-induced twin density should be interesting.

Surface roughness may prevent stress on the metastable or extended phase 1 surface from reaching the driving stress which would violate a basic assumption in Horie and Duvall's theory of plastic I decay and estimates of relaxation time inferred from close-in measurements. A possible experiment to eliminate surface effects would be to deposit within a few nanoseconds, at some depth, enough high energy electrons to create a shock exceeding the transformation pressure. This would not be a simple experiment, but it would avoid the surface problem since the shock would be formed internally.

REFERENCES

1. P. W. Bridgman, Collected Experimental Papers (Harvard University Press, Cambridge, Mass., 1964).
2. D. Bancroft, E. L. Peterson, and F. S. Minshall, J. Appl. Phys. 27, 291 (1956).
3. F. P. Bundy, J. Appl. Phys. 36, 616 (1965).
4. R. W. Lynch and H. G. Drickamer, J. Chem. Phys. 44, 181 (1966).
5. P. S. De Carli and J. C. Jamieson, Science 133, 1821 (1961).
6. R. J. Zeto and H. B. Vanfleet, J. Appl. Phys. 42, 1001 (1971).
7. R. E. Duff and S. Minshall, Phys. Rev. 108, 1207 (1957).
8. R. H. Wentorf, Jr. and J. S. Kasper, Science 139, 338 (1963).
9. W. H. Gust and E. B. Royce, J. Appl. Phys. 42, 1897 (1971).
10. W. P. Bundy and R. H. Wentorf, Jr., J. Chem. Phys. 38, 1144 (1963).
11. N. L. Coleburn and J. W. Forbes, J. Chem. Phys. 48, 555 (1967).
12. F. Dachele and R. Roy, Nature 4718, 34 (1960).
13. L. Leiserowitz, G. M. Schmidt, and A. Shamgar, J. Phys. and Chem. Solids 27, 1453 (1966).
14. R. H. Frushour and R. Roy, J. Appl. Phys. 44, 4417 (1973).
15. L. M. Barker and R. E. Hollenbach, J. Appl. Phys. 45, 4872 (1974).
16. D. B. Hayes, "Experimental Determination of Phase Transformation Rates in Shocked Potassium Chloride," Ph.D. Thesis, Washington State University, Pullman (1973).
17. D. B. Hayes, J. Appl. Phys. 45, 1208 (1974).

18. R. H. Warnes, *J. Appl. Phys.* 38, 4629 (1967).
19. D. E. Grady, W. J. Murri, and G. R. Fowles, *J. Geophys. Res.* 79, 332 (1974).
20. Y. Horie and G. E. Duvall, "Shock Waves and Kinetics of Solid-Solid Transition," in Proceedings of the Army Symposium on Solid Mechanics, Applied Materials and Mechanics Research Center, Watertown, Mass., September, 1968.
21. J. M. Walsh, *Bull. Am. Phys. Soc.* 29, 28 (1954).
22. F. S. Minshall, "The Dynamic Response of Iron and Iron Alloys to Shock Waves," in Response of Metals to High Velocity Deformation (Interscience, 1961), pp. 249-274. P. G. Shewmon and V. F. Zackay, eds.
23. S. A. Novikov, I. I. Divnov, and A. G. Ivanov, *Sov. Phys. JETP.* 20, 545 (1965).
24. C. S. Smith, *Trans. AIME* 214, 574 (1958).
25. C. S. Smith and C. M. Fowler, "Further Metallographic Studies on Metals after Explosive Shock," in Response of Metals to High Velocity Deformation (Interscience, 1961), pp. 309-342. P. G. Shewmon and V. F. Zackay, eds.
26. G. E. Duvall and Y. Horie, "Shock Induced Phase Transitions," in Fourth Symposium on Detonation (U.S. Government Printing Office, October, 1965), pp. 248-257.
27. D. J. Andrews, "Equation of State of the Alpha to epsilon Phases of Iron," Ph.D. Thesis, Washington State University, Pullman (1970).
28. D. J. Andrews, *J. Phys. Chem. Solids* 34, 825 (1973).
29. D. J. Andrews, *J. Comp. Phys.* 7, 310 (1971).
30. V. N. German, M. P. Speranskaya, L. V. Al'Tshuler, and L. A. Tarasova, English Translation of *Fiz. metal, metalloved.* 30, 1018 (1970).
31. H. G. Bowden and P. M. Kelly, *ACTA Metallurgica* 15, 1489 (1967).
32. P. M. Giles, M. H. Longenbach, and A. R. Marder, *J. Appl. Phys.* 42, 4290 (1971).
33. H. Mao, W. A. Bassett, and T. Takahashi, *J. Appl. Phys.* 38, 272 (1967).

34. D. M. Pipkorn, C. K. Edge, P. DeBrunner, G. DePasquali, H. G. Drickamer, and H. Frauenfelder, Phys. Rev. 135, No. 6A, A1604 (1964).
35. R. L. Clendenen and H. G. Drickamer, J. Phys. Chem. Solids 25, 865 (1964).
36. J. W. Taylor and M. H. Rice, J. Appl. Phys. 34, 364 (1963).
37. J. M. Walsh, M. H. Rice, R. G. McQueen, and F. L. Yarger, Phys. Rev. 108, 196 (1957).
38. C. M. Fowler, F. S. Minshall, and E. G. Zukas, "A Metallurgical Method for Simplifying the Determination of Hugoniot Curves for Iron Alloys in the Two-Wave Region," in Response of Metals to High Velocity Deformation (Interscience, 1961), pp. 275-308. P. G. Shewmon and V. F. Zackay, eds.
39. T. J. Ahrens, J. T. Rosenberg, M. H. Ruderman, "Dynamic Properties of Rocks," Stanford Research Institute Report No. DASA 1868 (1966).
40. G. R. Fowles, G. E. Duvall, J. Asay, P. Bellamy, F. Feistman, D. Grady, T. Michaels, and R. Mitchell, Rev. Sci. Instr. 41, 984 (1970).
41. J. R. Asay, "Effects of Point Defects on Elastic Precursor Decay in Lithium Fluoride," Ph.D. Thesis, Washington State University, Pullman (1972).
42. D. R. Curran, J. Appl. Phys. 34, 2677 (1963).
43. J. O. Erkman and G. E. Duvall, "Elastoplasticity and the Attenuation of Shock Waves," in Proceedings of Midwestern Mechanics Conference (University of Wisconsin, Madison, August 1965).
44. T. R. Loree, C. M. Fowler, E. G. Zukas, and F. S. Minshall, J. Appl. Phys. 37, 1918 (1966).
45. P. C. Johnson, B. A. Stein, and R. S. Davis, J. Appl. Phys. 33, 557 (1962).
46. J. C. Fisher, Acta Met. 1, 32 (1953).
47. C. L. Magee, "The Nucleation of Martensite," in Phase Transformations (American Society for Metals, 1970), Ch. 3, pp. 115-156.
48. L. Kaufman and M. Cohen, "Thermodynamics and Kinetics of Martensitic Transformations," in Progress in Metal Physics (Pergamon Press, 1958), Vol. 7, Ch. 3, pp. 165-246.

49. W. G. Burgers, *Physica* 1, 561 (1934).
50. C. Kittel, Introduction to Solid State Physics (John Wiley & Sons, Inc., 1956).
51. J. W. Christian, The Theory of Transformation in Metals and Alloys (Pergamon Press, 1965).
52. D. McLean, Mechanical Properties of Metals (John Wiley & Sons, Inc., 1962).
53. J. Frenkel, Kinetic Theory of Liquids (Dover Publications, 1955).
54. W. Kaplan, Advanced Calculus (Addison-Wesley Publishing Co., Inc., 1959).
55. J. Burke, The Kinetics of Phase Transformations in Metals (Pergamon Press, 1965).
56. J. N. Johnson and R. W. Rhode, *J. Appl. Phys.* 42, 4171 (1971).
57. G. W. Swan, G. E. Duvall, and C. K. Thornhill, *J. Mech. Phys. Solids* 21, 215 (1973).
58. W. Band, *Am. J. Phys.* 29, 780 (1961).
59. J. N. Johnson, "Consideration for Calculation of Shock-Induced Phase Transformations, : Sandia Laboratories Report (September 1972), SC-RR-72 0626.
60. J. N. Johnson, D. B. Hayes, and J. R. Asay, *J. Phys. Chem. Solids* 35, 501 (1974).
61. K. C. Seddon, "The Barr and Stroud-CP6 Rotating Mirror Streak Camera Determination of Writing Speed," in Proceedings of the 8th International Congress on High-Speed Photography, Stockholm (1968), pp. 108-111. N. R. Nilsson and L. Hogberg, eds.
62. J. K. Landre, *Rev. sci. Instr.* 35, 796 (1964).
63. Y. Beers, Introduction to the Theory of Errors (Addison-Wesley Co., Inc., 1962), 2nd ed.
64. A. S. Dubovik, "Photographic Recording of High Speed Process," NASA Technical translation No. NASA TTF-377 (1965).

APPENDIX A

THERMODYNAMICALLY CONSISTENT EQUATION OF STATE

The present interest in an equation of state is restricted to describing isotherms and Hugoniot of alpha and epsilon iron. These thermodynamic paths involve very small portions of the equilibrium surface of each phase. In fact, when iron is shocked to a stress of 200 kbar, the total temperature rise is less than 100°K . This temperature rise will displace the Hugoniot stress by less than 3 percent from the isothermal stress at the same volume.

By assuming that the specific heat is constant, simple analytical expressions result which describe the equilibrium alpha and epsilon surfaces. Accurate isothermal compression data have been reported for alpha and epsilon iron in terms of the Murnaghan equation.³³ The equation of state developed below reduces exactly to the Murnaghan equation for isotherms. The accuracy of the calculated Hugoniot, which varies only slightly from the isotherm, is limited principally by the experimental error of ± 2 percent in stress for the measured isotherms.³³

The choice of the present equation of state rather than that of Andrews^{27,28} was made for its simplicity. Andrews' equation of state exists as a deck of computer cards, and analytical expressions describing the equilibrium surfaces are not

readily available. However, Andrews' equation of state does define all of the equilibrium surfaces of alpha and epsilon iron and is more useful than the present equation of state for a variety of problems. Except for the assumptions of constant C_V and constant ratio of Gruenisen parameter to volume for the epsilon phase, the present equation of state and Andrews' equation of state are similar in principle. In practice, the two approaches differ considerably. For example, the present equation of state relies on one set of isothermal compression data to define the equilibrium surfaces while Andrews fitted all the available thermodynamic data to the appropriate derivatives of a Helmholtz potential function to define the surfaces. The two equations of state give values on the Hugoniot for volume and temperature at 130-kbar stress which differ by less than 0.3 percent. The excellent agreement between the equations of state was expected.

A.1. Equilibrium Surfaces

The specific heat at constant volume is assumed constant following the approach suggested by Johnson.^{59,60} This approach is sufficient for making accurate predictions along a Hugoniot. These assumptions, along with the isothermal compression data of alpha and epsilon iron, define the equilibrium surfaces for the two phases.

The primary assumption is that the specific heat at constant volume is independent of temperature and volume:

$$C_V = \left(\frac{\partial E}{\partial T} \right)_V = \text{constant} \quad . \quad (\text{A.1})$$

This assumption restricts E to the form,

$$E = C_V T + f(V) , \quad (A.2)$$

where $f(V)$ is an arbitrary function of specific volume V .

Since C_V is constant, Maxwell's equations require

$$\left[\frac{\partial C_V}{\partial V} \right]_T = T \left[\frac{\partial^2 P}{\partial T^2} \right]_V = 0 , \quad (A.3)$$

which gives

$$P = r(V)T + y(V) = \frac{\Gamma C_V}{V} T - f'(V) . \quad (A.4)$$

The assumption is made that

$$\left[\frac{\partial P}{\partial T} \right]_V = C_V \left[\frac{\partial P}{\partial E} \right]_V = \frac{\Gamma}{V} C_V = \text{constant} , \quad (A.5)$$

where Γ is the Grüneisen parameter. Then, from Eqs. (A.4) and (A.5), we find that

$$r(V) = C_V \frac{\Gamma}{V} = b C_V = \text{constant} . \quad (A.6)$$

Now any path on the thermodynamic equilibrium surface can be used to determine $y(V)$ in Eq. (A.4). Therefore, choosing the compression path along an isotherm is a logical choice because isothermal data are known in the form of the Murnaghan equation.

Each phase is represented by

$$P(V_i) = B_{0i} \left[\left[\frac{V_i}{V_0} \right]^{-n_i} - 1 \right] , \quad (A.7)$$

where the temperature T_0 is held constant, the subscript i indicates the particular phase, and the parameters B_{0i} and n_i are fitted constants. Combining Eqs. (A.4), (A.6), and (A.7) results in

$$P(V_i, T) = b C_{V_i} (T - T_0) + B_{0i} \left[\left[\frac{V_i}{V_0} \right]^{-n_i} - 1 \right], \quad (\text{A.8})$$

which defines any P, V, T path on the equilibrium surfaces.

To complete the definition of the surfaces, the function $f(V)$ of Eq. (A.2) has to be evaluated. This can be done in a consistent way with the use of the following identity:

$$G = E - T S + P V . \quad (\text{A.9})$$

The use of subscript i is dropped for convenience. To complete Eq. (A.9) an expression for S is required. Since

$$\left[\frac{\partial S}{\partial V} \right]_T = b C_V \quad (\text{A.10})$$

and

$$\left[\frac{\partial S}{\partial T} \right]_V = C_V / T . \quad (\text{A.11})$$

Then

$$S = S_0 - b C_V (V_0 - V) + C_V \ln(T/T_0) . \quad (\text{A.12})$$

Using the identity,

$$V = \left[\frac{\partial G}{\partial P} \right]_T, \quad (\text{A.13})$$

and combining Eqs. (A.2), (A.8), (A.9), (A.12), and (A.13) results in

$$\left[\frac{\partial f(V)}{\partial V} \right]_T = -T_0 b C_V + B_0 V_0 \left[\left[\frac{V}{V_0} \right]^{-1} - 1 \right]. \quad (\text{A.14})$$

Integrating eq. (A.14) for $f(V)$ and substituting in Eq. (A.2) results in the expression,

$$E = E_0 + C_V(T-T_0) - T_0 b C_V(V_0-V) + V_0 B_0 \left[\frac{\left[\frac{V}{V_0} \right]^{1-n} - 1}{n-1} - \frac{V_0-V}{V_0} \right]. \quad (\text{A.15})$$

Equations (A.8), (A.12), and (A.15) define the phase 1 and phase 2 equilibrium surfaces within initial values V_{01} , V_{02} , E_{01} , E_{02} , S_{01} , and S_{02} . The value for V_{01} for iron is easily measured while V_{02} has been inferred from x-ray measurements of coexisting phases.³³ The value for S_{01} can be arbitrarily chosen while S_{02} is fixed by the difference in entropy between phases which can be inferred from the measured slope of the phase line or obtained from a thermodynamically consistent empirical equation of state which is fitted to all types of experimental data.^{27,28} The magnitude of E_{01} can be arbitrarily chosen while E_{02} must be specified by some additional relationship. A relationship which makes the connection between the equilibrium surfaces is:

$$G_{21}(P^*, T^*) = 0, \quad (\text{A.16})$$

where G_{21} is the difference between Gibbs energies of the phases, (P^*, T^*) is the equilibrium transformation point. This equilibrium condition with Eq. (A.9) determines the value of E_{02} . Use of Eq. (A.16) to determine the equilibrium surface provides no assurance that the state point in any real process will actually lie on such a surface (cf Chapter 5).

The values for E_{01} , S_{01} , and S_{02} at 1 atmosphere pressure and a temperature of 295°K were chosen to be the same as those used by Andrews.^{27,28} The value for E_{02} was determined from the relation $G_{21}(116 \text{ kbar}, 332^\circ\text{K}) = 0$. The initial value of C_{V2} is the classical value of $3R$ where R is the gas constant. The initial values used to define the equilibrium surfaces are listed in Table A.1.

TABLE A.1.--Initial values
($T=295^\circ\text{K}, P=0$)

Variable	Alpha phase	Epsilon phase
V_0	0.1272	$0.1208 \text{ cm}^3/\text{gm}$
E_0	7.932×10^{-4}	$1.667 \times 10^{-3} \text{ Mbar cm}^3/\text{gm}$
S_0	4.863×10^{-6}	$5.323 \times 10^{-6} \text{ Mbar cm}^3/\text{gm deg}$
n	5.917	5.102
B_0	0.275	0.325 Mbar
Γ	1.735	2.0
C_V	4.447×10^{-6}	$4.466 \times 10^{-6} \text{ Mbar cm}^3/\text{gm deg}$

A.2. Approximations of Potential Functions

It is often found convenient to use simple approximations for the differences between the internal energies of the two phases and also the difference between the Gibbs energies. To demonstrate their accuracy, the approximations are compared to the more accurate equation of state results. It is important to keep in mind that these differences are between values that lie on the equilibrium surfaces. The first useful approximation is for $G_2 - G_1$. Since

$$d(G_2 - G_1) = (V_2 - V_1)dP - (S_2 - S_1)dT ; \quad (A.17)$$

if $V_2 - V_1$ and $S_2 - S_1$ are constant, then

$$G_2 - G_1 = (V_2 - V_1)(P - P^*) - (S_2 - S_1)(T - T^*) , \quad (A.18)$$

the difference between internal energy of the two phases, is

$$E_2 - E_1 = T^*(S_2 - S_1) - P^*(V_2 - V_1) . \quad (A.19)$$

For the approximate calculations, the following values are used: $V_2 - V_1 = -0.00604 \text{ cm}^3/\text{gm}$, $S_2 - S_1 = 3.67 \times 10^{-7} \text{ Mbar cm}^3/\text{gm}$, and $P^* = 0.116 \text{ Mbar}$, $T^* = 332^\circ\text{K}$. Figure A.1 shows the result from the approximate relation for the Gibbs energy differences and those from the more exact equation of state for the mixed phase Hugoniot of iron. The agreement between Eq. (A.18) and the equation of state results is excellent. The approximate

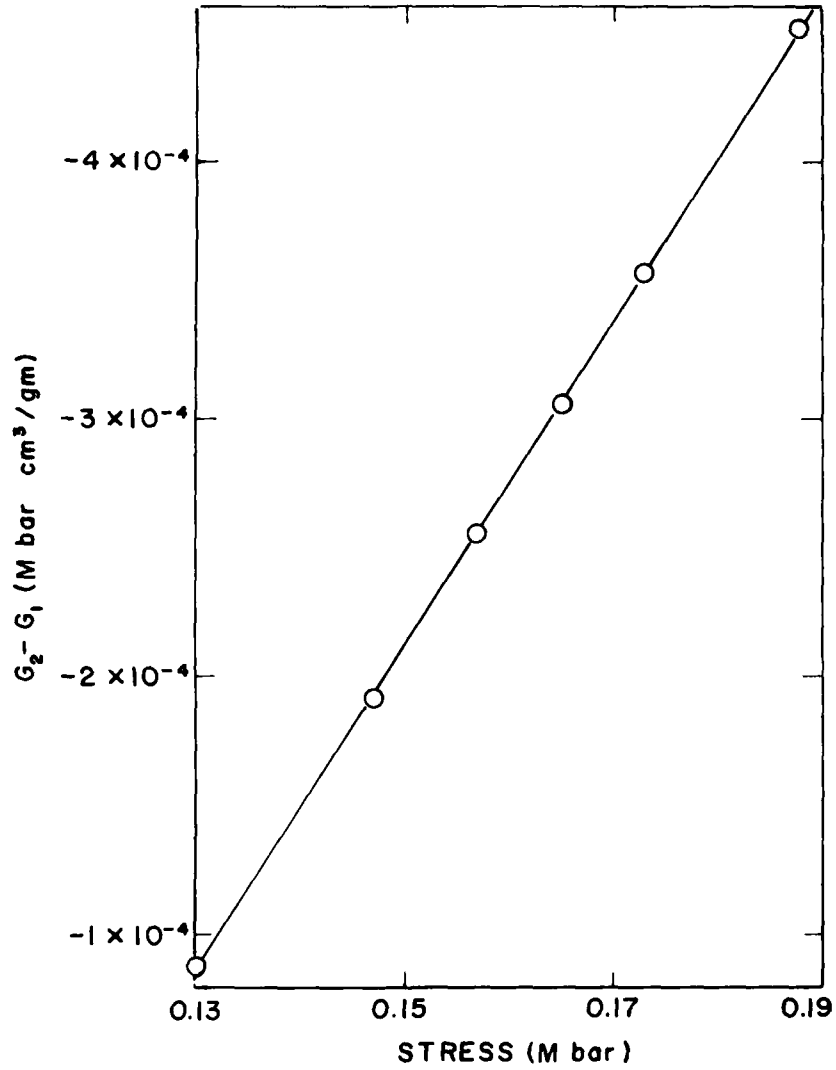


FIGURE A.1 DIFFERENCE BETWEEN GIBBS ENERGIES OF ALPHA AND EPSILON IRON ALONG THE MIXED PHASE HUGONIOT.

value, $E_2 - E_1 = 8.22 \times 10^{-4}$ Mbar cm^3/gm , agrees within 2 percent of the equation of state results over the stress range of 130 to 200 kbar.

APPENDIX B

STREAK CAMERA CALIBRATION

The Cordin 132 streak camera writing speed was calibrated by recording the output of a crystal-controlled oscillator displayed on the face of an oscilloscope.⁶¹ The dynamic spatial resolution for the camera was measured by recording the image of a Ronchi ruling for different camera writing speeds. The details of the calibration experiments are given below.

B.1. Writing Speed

A schematic of the calibration setup is given in Fig. B.1. The equipment used for the calibration experiments consisted of the streak camera, the synchronizer circuit, a Hewlett-Packard 5512A electronic counter, a resistance-capacitor (RC) pulse power supply, a Tektronix 535 oscilloscope, and a General Radio 1213A oscillator. The oscillator was stable to within +4 hz out of 10^7 hz for 24 hours. The frequency scale of the oscillator was accurate to +3.4 hz out of 10^6 hz. The electronic counter was accurate to one count.

The electronic equipment was connected as shown in Fig. B.1 and the camera was focused on the face of the oscilloscope's cathode ray tube. The camera's mirror was rotated at a constant speed and then a switch on the camera controls was closed which opened the camera shutter and sent a pulse to the

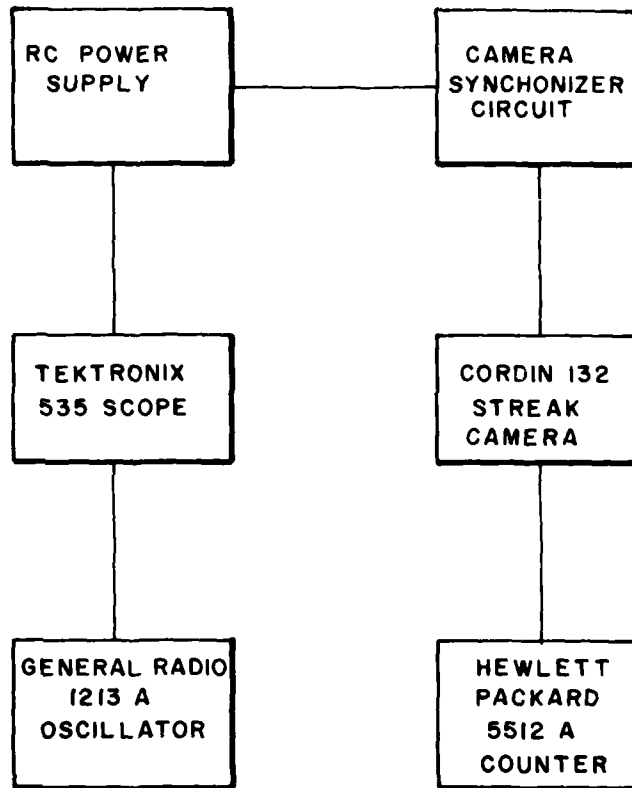


FIGURE B.1 SCHEMATIC OF CALIBRATION TECHNIQUE FOR THE STREAK CAMERA.

synchronizer circuit. The synchronizer circuit assures that the rotating mirror is in proper position to record on the film and supplies a pulse to trigger the RC power supply. The power supply applied -80V pulse to the cathode ray tube which brightens the scope trace for a few milliseconds. A 100 KHz signal from the oscillator was continuously applied to the vertical input of the oscilloscope without sweeping the scope in time. A vertical oscillating line image of the oscillator's signal was displayed on the scope face and then recorded dynamically by the streak camera. A sinusoidal wave results on the streak camera film with accurately known peak-to-peak time intervals.

The camera writing speed is given by

$$W = F \cdot R \quad (B.1)$$

where W is the writing speed, F is the calibration parameter, and R is the rotation speed of the camera's mirror. The results of the calibrations are given in Table B.1.

TABLE B.1.--Calibration experimental results

Experiment Number	R (rev/sec)	W (mm/ μ sec)	F 10^{-3} (mm)
Cal-1	250	1.0075 \pm .0025	4.030 \pm .001
Cal-2	250	1.0075 \pm .0025	4.030 \pm .001
Cal-3	1000	4.04 \pm .02	4.040 \pm .02

The record for experiment Cal-3 was faint and could not be read precisely as the given error indicates, but the results are in good agreement with Cal-1 and Cal-2. The calibration parameter F should be constant for revolution speeds up to 5000 hz since beryllium mirrors⁶² do not physically distort for these rotation speeds.

B.2. Dynamic Spatial Resolution

The practical definition of the spatial resolution was taken as the number of lines/mm distinguishable on the film in a simulated experimental setup. The dynamic spatial resolution of the camera was measured by dynamically recording the image of a Ronchi ruling. The glass ruling plate was located in the test chamber so the camera would view it in an experimental situation. The camera was focused on the ruling with the projection of the slit plane perpendicular to the rulings. The light for the camera was provided by an exploding wire light source located just behind the ruling. The camera was run at speeds up to 15 mm/ μ sec. The dynamic spatial resolution for this range of writing speeds was > 30 lines/mm.

APPENDIX C
ERROR ANALYSIS

This appendix outlines the error analysis used for this work. The general treatment of errors is given in Section C.1, and a specific example of the error in the measurements of free surface velocity is treated in Section C.2.

C.1. General Treatment of Errors

The error in a quantity is the uncertainty in its measurement. The value of a quantity may depend on two or more other parameters. Each of these parameters is uncertain to some degree. To estimate the total uncertainty in the quantity requires a prescription for calculating the error which includes the propagation of errors. The present error analysis gives such a prescription which depends on obtaining analytical expressions of the error in terms of known parameters. The analysis is based on a book by Yardley Beers.⁶³

The errors are reported in the shorthand form " $f \pm e$ " where e is the average deviation of f . The total magnitude of the error is just $2e$.

Errors may be random, as in the case when a measurement is repeated several times. The results will be distributed around a "most probable" value which is assumed here to be the average value. For random errors there is a possibility of

compensation among the various contributions. It is expected that the total error will be algebraically less than the sum of the separate contributions. A logical way of adding the separate contributions is to take the square root of the sum of their squares (hereinafter called SRSS) which does have the compensating property. The rule for combining random errors is

$$\epsilon_f = \left[\left[\frac{\partial f}{\partial x} \right]^2 \epsilon_x^2 + \left[\frac{\partial f}{\partial y} \right]^2 \epsilon_y^2 \right]^{1/2} \quad (C.1)$$

where $f = F(x,y)$ and x,y are the independent measured parameters. The function f can depend on any number of parameters. The choice of two parameters for Eq. (C.1) was made only for illustrative purposes.

Errors may be systematic where all the individual values are in error by the same amount. These errors cannot be estimated by repeated measurements. The systematic error often comes from the uncertainty in the calibration of the instrument used to measure the parameter. These errors combine algebraically because compensation among the various contributions is not likely. Therefore,

$$\epsilon_f = \frac{\partial f}{\partial x} \epsilon_x + \frac{\partial f}{\partial y} \epsilon_y \quad (C.2)$$

When both kinds of errors are encountered they are combined by taking the SRSS of both separate contributions to give a total estimate of error for that particular parameter.

From a set of measurements of a parameter the best value available is the average value. The error associated with this average value is not the average of the deviations from this average value but rather the average of these deviations divided by the square root of the number of measurements. In other words, the precision improves in proportion to the square root of the reciprocal of the number of measurements in the sample set.

C.2. Error in Free Surface Velocity Measurements

The experimental technique used to measure the free surface motion was to photographically record with a streak camera the changes in the intensity of reflected light from the tilted mirrors which were placed on the surfaces of the test samples. For this experimental technique the free surface velocity is a function of five different parameters. (See Chapter 2.) Each parameter is unknown by a certain amount. Each individual uncertainty in the five parameters contributes to the overall uncertainty in the free surface velocity. Determination of the total uncertainty is the goal of this appendix.

The free surface velocity due to the plastic I shock is given by

$$u_{fs} = \frac{u_c}{M_f} \frac{\tan \alpha}{\tan \gamma - \tan \omega} \quad (C.3)$$

where u_{fs} is the free surface velocity due to the plastic I shock, u_c is the camera speed, α is the tilted mirror angle,

M_f is the magnification (image/object), γ is the angle of the trace, and ω is the wave tilt angle on the film. The total error in u_{fs} is given by

$$\frac{\epsilon}{u_{fs}} = \left[\left[\frac{\epsilon_{u_c}}{u_c} \right]^2 + \left[\frac{\epsilon_{M_f}}{M_f} \right]^2 + \left[\frac{2\epsilon_\alpha}{\sin 2\alpha} \right]^2 + \left[\frac{\epsilon_\gamma}{\cos^2 \gamma (\tan \gamma - \tan \omega)} \right]^2 + \left[\frac{\epsilon_\omega}{\cos^2 \omega \tan \gamma - \tan \omega} \right]^2 \right]^{1/2} \quad (C.4)$$

The individual errors for camera speed, magnification, mirror angle, trace angle, and wave tilt angle contain both random and systematic errors. The random errors were estimated by taking the deviations from the average of a number of measurements of each parameter. The systematic error was usually taken as equal to one-half of the smallest division of the instrument used to measure the parameter. The total error for each parameter was then found by taking the SRSS of the systematic and random errors.

C.2.1. Sources of Various Errors

The performance of accurate experiments requires knowledge of the source and magnitude of the various errors. The purpose of this subsection is to identify the sources of error in the free surface velocity measurement and to determine which are the important errors.

The error in the camera writing speed was determined from the error associated with the calibration constant (see

Appendix B) and the uncertainty of ± 1 count in the counter reading which determined the camera's rotor speed.

The total error in the magnification was determined by the length of the precision grid used and the uncertainty of ± 0.05 mm in measuring the image of the grid with a precision eyepiece.

The total error in the mirror angle α was determined by the scatter in the readings and the uncertainty of ± 1 min of arc in measuring the angle with a Shadowgraph instrument.

The error in determining the trace angle γ and the tilt angle ω is more difficult to ascertain. They require an understanding of the camera operation, experimental design, and record reading technique. A detailed treatment of this error is given in Section C.2.2.

Table C.1 summarizes the total contributions to the error in u_{fs} for a typical experiment. The largest and most important error is in the trace angle γ .

TABLE C.1.--Various contributions to the error in u_{fs}

$\frac{\epsilon_{u_c}}{u_c}$	$\frac{\epsilon_{M_f}}{M_f}$	$\frac{2\epsilon_\alpha}{\sin 2\alpha}$	$\frac{\epsilon_\gamma}{\cos^2 \gamma (\tan \gamma - \tan \omega)}$	$\frac{\epsilon_\omega}{\cos^2 \omega (\tan \gamma - \tan \omega)}$
0.006	0.005	0.008	0.028	0.003

C.2.2. Errors in Determining the trace Angle and the Wave Tilt Angle

It was shown above that the error in determining the trace angle on the film is the largest contributor to the total error in u_{fs} . Therefore, a detailed discussion on the systematic part of this error is given here. The estimates of the systematic errors in determining the trace angles on the camera records are similar to those of Dubovik.⁶⁴ There are four separate contributions to this error: (1) the film alignment in the reader instrument, (2) the fuzziness of the trace, (3) the reader instrument accuracy, and (4) the spatial resolution. Each is treated as independent of the other, which is not strictly true. It is a reasonable assumption to make since the sole purpose is to obtain a reasonable estimate of the error.

The first contribution to the systematic error in γ is due to the alignment of the film parallel to the time axis for reading. This error is ≤ 0.001 rad based on a graphic accuracy of ± 0.1 mm per 100 mm which can be realized in practice.

The second and largest contribution to the error in γ is due to the fading and fuzziness of the trace, which depends on the camera slit width and response of the film to different exposure times. The recording of the motion of an opaque half-plane moving at a constant speed parallel to the slit plane (along the length of the slit) results in a cut-off of the light to the camera. The cut-off is not recorded as a sharp loss of light because of the finite width of the slit. Rather, it is a

line of some width made up of many thin lines each at different optical densities and at an angle γ to the space axis of the film. The optical density of the broad line varies from high to low density in the direction of the camera sweep (e.i., increasing time). The geometry of the envelope of lines is shown in Fig. C.1.

An analytical expression for the error can easily be derived from the geometry, resulting in

$$\epsilon = AB \sin \gamma / (S - AB \cos \gamma) \quad (C.5)$$

where AB is the camera slit width, γ is the angle of the trace, and S is the trace length. The typical systematic error is 0.018 rad for AB = 0.05 mm, $\gamma = 0.786$ rad, and S = 2 mm.

The third contribution to the error is that due to the accuracy of the Vanguard analyzer in determining γ . By assuming the error can be assigned to one reader variable, then Eq. (C.5) is applicable. The slit width AB in Eq. (C.5) is replaced by the smallest distance measurable by the Vanguard analyzer (0.005 mm). A typical error is 0.002 rad for $\gamma = 0.786$ rad and S = 2 mm.

The fourth contribution to the error is due to the spatial resolution. The smallest distinguishable spatial distance on the film was about 0.03 mm for the camera in a simulated experimental setup. (See Appendix B.) Treating this uncertainty as independent of the others, an expression for this error becomes

$$\epsilon_{SR} = \frac{0.03 \text{ mm}}{S} \cdot \cos \gamma \quad (C.6)$$

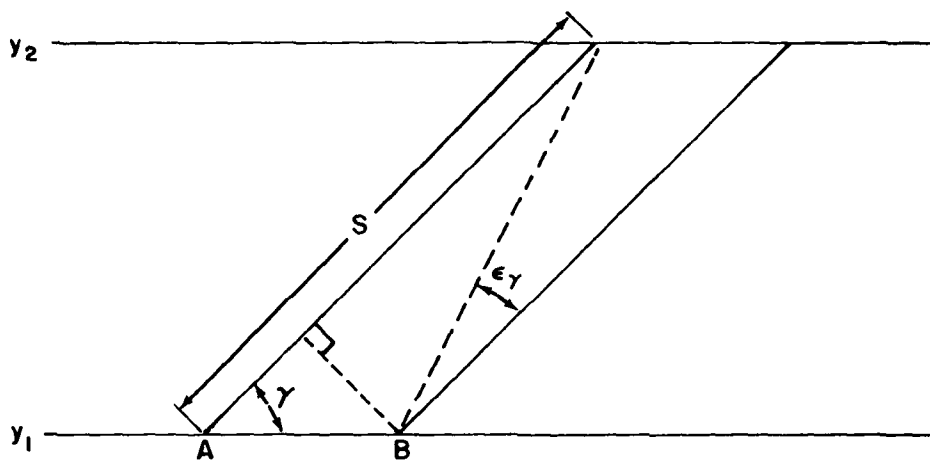


FIGURE C.1 ENVELOPE OF PARALLEL LINES BETWEEN A AND B MAKE UP THE STREAK CAMERA TRACE.

The typical contribution for this error is 0.011 rad when $S = 2$ mm and $\gamma = 0.786$ rad.

The typical errors were given above for each separate case to illustrate which was the largest and dominating error. It is obvious by comparing the typical contributions given for each factor above that the largest errors are due to the fuzziness of the trace and to the spatial resolution of the camera.

It should be emphasized that the above analysis for the error in γ is a pessimistic one. The analysis was limited to the error between two data points while the actual measurement of the angle typically resulted in 15 data points which were least-squares fitted to a straight line. The least-squares fitting of the data reduces the measuring error. In addition, placing the Vanguard analyzer's hairlines on film coordinates of about the same optical density reduces the trace width to less than the slit width. To compensate for these factors, personal judgment must be used. A reduction of one-half of the error due to the slit width error in Eq. (C.5) was used.

The same methods used in estimating errors in the trace angle apply and were used for the errors in the wave tilt angle ω .

APPENDIX D

PERMANENT REGIME WAVE SOLUTION

A nonsteady shock will approach a steady shock in time.⁵⁷
 A solution for the steady shock is given here based on the constitutive relation of the Horie-Duvall model.²⁰

D.1. General Solution

The differential flow equations in Eulerian coordinates are:

$$\frac{\partial \rho}{\partial t} + \frac{\partial \rho u}{\partial x} = 0 , \quad (D.1)$$

$$\rho \frac{du}{dt} = - \frac{\partial P}{\partial x} , \quad (D.2)$$

$$\frac{dE}{dt} = -P \frac{dV}{dt} , \quad (D.3)$$

$$\rho \equiv \frac{1}{V} .$$

The total time derivative is $(d/dt) = (\partial/\partial t) + u(\partial/\partial x)$. The steady state condition is that $\partial/\partial t = 0$ which, applied to the flow equations, results in

$$\rho u = m = \text{constant} , \quad (D.4)$$

$$P + mu = \text{constant} , \quad (D.5)$$

$$E - \frac{1}{2} \left[\frac{P}{m} \right]^2 = \text{constant} \quad (\text{D.6})$$

where P represents uniaxial stress. Combining Eqs. (D.4) and (D.5) results in a useful equation which defines the compression path as a straight line in the P - V plane connecting the initial and final P - V states. The equation is

$$P - P^* = -m^2(V - V^*) \quad (\text{D.7})$$

Another useful relation is obtained from Eqs. (D.1) and (D.2):

$$\frac{dV}{dx} = -\frac{1}{m^2} \frac{dP}{dx} \quad (\text{D.8})$$

In the mixed phase region the extensive parameters V and E are defined as functions of P , T , and f such that:

$$V(P, T, f) = V_1(P, T) + f[V_2(P, T) - V_1(P, T)] \quad (\text{D.9})$$

$$E(P, T, f) = E_1(P, T) + f[E_2(P, T) - E_1(P, T)] \quad (\text{D.10})$$

Since P , T , and f are implicit functions of x , Eq. (D.9) and (D.10) result in

$$\frac{dV}{dx} = \left[\frac{\partial V}{\partial P} \right]_{T, f} \frac{dP}{dx} + \left[\frac{\partial V}{\partial T} \right]_{P, f} \frac{dT}{dx} + \left[\frac{\partial V}{\partial f} \right]_{T, P} \frac{df}{dx} \quad (\text{D.11})$$

$$\frac{dE}{dx} = \left[\frac{\partial E}{\partial P} \right]_{T, f} \frac{dP}{dx} + \left[\frac{\partial E}{\partial T} \right]_{P, f} \frac{dT}{dx} + \left[\frac{\partial E}{\partial f} \right]_{T, P} \frac{df}{dx} \quad (\text{D.12})$$

Using Eqs. (D.8), (D.9), and (D.10) and the thermodynamic identities for specific heat C_p , compressibility K_T , and thermal expansion β , then Eqs. (D.11) and (D.12) become:

$$\frac{dP}{dx} = \frac{V\beta_f \frac{dT}{dx} + (V_2 - V_1) \frac{df}{dx}}{VK_{T,f} - \frac{1}{m^2}}, \quad (D.13)$$

$$\frac{dT}{dx} = \frac{\frac{dP}{dx} \left[\frac{P}{m^2} - PVK_{T,f} + TV\beta_f \right] - (E_2 - E_1) \frac{df}{dx}}{C_{P,f} - PV\beta_f}. \quad (D.14)$$

Equations (D.13) and (D.14) require only an equation of state and a relation for df/dx to solve for the stress and temperature distribution in a steady wave.

For iron the second term on the right hand side of Eq. (D.13) is about 60 times greater than the first term. Steady profile calculations with this first term neglected (for example see Fig. (6.2)) are called temperature independent.

D.2. Rate Equation

Horie and Duvall²⁰ assumed a relation for df/dt (see Chapter 6) that for steady waves can be written as

$$U \frac{df}{dx} = \frac{f^{eq} - f}{\tau_1}. \quad (D.15)$$

Andrew^{27,29} later showed that by defining τ as the constant energy and constant volume equilibration time, the rate equation can be directly related to the difference in Gibbs energies. For steady waves this rate equation becomes:

$$U \frac{df}{dx} = - \frac{J G_{21}}{|A| \tau_2}. \quad (D.16)$$

For small variations from equilibrium the determinant of A is

$$|A| = \begin{vmatrix} -VK_{T,f} & B_f V & \Delta V \\ PVK_{T,f} - TV\beta_f & C_{P,f} - PV\beta_f & \Delta E \\ \Delta V & -\Delta S & 0 \end{vmatrix}$$

$$= \Delta E (BV\Delta V - VK_{T,f}\Delta S) + \Delta V \Delta S (TV\beta_f - PVK_{T,f}) + (\Delta V)^2 (PV\beta_f - C_{P,f})$$

(D.17)

where $\Delta S = S_2 - S_1$ and $\Delta V = V_2 - V_1$.

The transformation Jacobian J was previously evaluated by Hayes¹⁶ as

$$J = J \begin{bmatrix} VEf \\ PTf \end{bmatrix} = -C_{P,f} VK_{S,f} \cdot$$

(D.18)

Equation (D.16) provides the necessary relation defining df/dx . Equations (D.13), (D.14), (D.17), and (D.18), and an equation of state give the stress and temperature distribution in the steady shock.

DISTRIBUTION LIST

Copies

Chief of Naval Material
Attn: MAT-03T
 MAT-08T2
Washington, D.C. 20360

Commander
Naval Air Systems Command
Attn: AIR-350
Department of the Navy
Washington, D.C. 20361

Commander
Naval Sea Systems Command
Attn: SEA-0332
 SEA-0333A
Department of the Navy
Washington, D.C. 20362

Commander
Naval Weapons Center
Attn: Technical Library
 H. D. Mallory
 G. Green
 E. Royce
China Lake, California 93555

Director
Naval Research Laboratory
Attn: Technical Information Section
Washington, D.C. 20375

Director
Office of the Secretary of Defense
Advanced Research Projects, Agency
Washington, D.C. 20301

Commanding Officer
Naval Weapons Evaluation Facility
Attn: Code AT-7
Kirtland Air Force Base
Albuquerque, New Mexico 87117

NSWC/WOL TR 77-137

DISTRIBUTION LIST (Cont.)

Copies

Superintendent Naval Academy
Attn: Library
Annapolis, Maryland 21402

Commanding Officer
Picatinny Arsenal
Attn: SARPA-TS-S #59
J. Hershkowitz
Dover, New Jersey 07801

Commanding General
Aberdeen Proving Ground
Attn: BRL
G. Hauver
Maryland 21005

Commanding Officer
Harry Diamond Laboratory
Attn: Library
2800 Powder Mill Road
Adelphi, Maryland 20783

Armament Development and Test Center
DIOSL/Technical Library
Eglin Air Force Base
Florida 32542

Energy Research and Development Administration
Attn: DMA
Washington, D.C. 20545

Director
Defense Nuclear Agency
Washington, D.C. 20305

Shock Hydrodynamics, Inc.
Attn: Dr. L. Zernow
15010 Ventura Boulevard
Sherman Oaks, California 91403

Chief
Office of Naval Research
Attn: Code 473, R. Miller
Code 473, J. H. Satkowski
800 North Quincy Street
Arlington, Virginia 22217

DISTRIBUTION LIST (Cont.)

Copies

Defense Documentation Center
Cameron Station
Alexandria, Virginia 22314

12

California Institute of Technology
Attn: T. J. Ahrens (252-21)
Pasadena, California 91125

Lawrence Livermore Laboratory
Attn: D. L. Banner (L-31)
J. Shaner
A. Mitchell
W. Gust (L-450)
R. Grover (L-450)
Q. Johnson (L-401)
W. Nellis
M. L. Wilkins (H Division)
P. O. Box 908
Livermore, California 94550

Los Alamos Scientific Laboratory
Attn: W. J. Carter
J. N. Johnson (T-14)
J. Wackerle (WX-7)
J. N. Fritz (M-6)
T. R. Neal (M-2)
R. McQueen
P. O. Box 1663
Los Alamos, New Mexico 87545

SRI International
Attn: D. Curran
P. DeCarli
Y. Gupta
W. Murri
Y. Horie
333 Ravenswood Ave.
Menlo Park, California 94025

Sandia Laboratories
Attn: J. R. Asay (Div.-5167)
B. M. Butcher (Div.-5167)
D. B. Hayes (Div.-2513)
D. Grady (Div.-5163)
R. A. Graham (Div.-5131)
J. E. Kennedy (Div.-2513)
G. A. Samara (Dept. 5130)
Albuquerque, New Mexico 87115

NSWC/WOL TR 77-137

DISTRIBUTION LIST (Cont.)

Copies

Systems, Science & Software
Attn: R. Duff
P. O. Box 7620
La Jolla, California 92038

Washington State University
Attn: G. E. Duvall
G. R. Fowles
M. H. Miles
Department Physics
Pullman, Washington 99163

Effects Technology, Inc.
Attn: W. Isbell
M. Graham
5383 Hollister Ave.
Santa Barbara, California 93111

U.S. Geological Survey
Attn: D. J. Andrews
345 Middlefield Road
Menlow Park, California 94025

Bethlehem Steel Corp
Homer Research Laboratories
Attn: P. M. Giles
Bethlehem, Pennsylvania 18016

TO AID IN UPDATING THE DISTRIBUTION LIST
FOR NAVAL SURFACE WEAPONS CENTER, WHITE
OAK LABORATORY TECHNICAL REPORTS PLEASE
COMPLETE THE FORM BELOW:

TO ALL HOLDERS OF NSWC/WOL TR 77-137
by J. W. Forbes, Code R-13
DO NOT RETURN THIS FORM IF ALL INFORMATION IS CURRENT

A. FACILITY NAME AND ADDRESS (OLD) (Show Zip Code)

NEW ADDRESS (Show Zip Code)

B. ATTENTION LINE ADDRESSES:

C.

REMOVE THIS FACILITY FROM THE DISTRIBUTION LIST FOR TECHNICAL REPORTS ON THIS SUBJECT.

D. NUMBER OF COPIES DESIRED _____

ATTENTION: CODE R-13

COMMANDER
NAVAL SURFACE WEAPONS CENTER
WHITE OAK, SILVER SPRING, MARYLAND 20910

OFFICIAL BUSINESS
PENALTY FOR PRIVATE USE, \$300

DEPARTMENT OF THE NAVY
NAVAL SURFACE WEAPONS CENTER
WHITE OAK, SILVER SPRING, MD. 20910

POSTAGE AND FEES PAID
DEPARTMENT OF THE NAVY
DOD 316

